Thermomechanical study of the gigacycle fatigue behavior of pure iron and carbon-manganese steels : influence of chemical composition and microstructure on damage and crack initiation mechanism

Xiaoxue Pu

Université Paris Nanterre
200 av. de la République
92001 Nanterre Cedex
www.parisnanterre.fr

Membre de l'université Paris Lumières

École doctorale 139 : Connaissance, langage, modélisation

Laboratoire d'Energetique

Mecanique et Electromagnetisme

Xiaoxue PU

Thermomechanical study of the gigacycle fatigue behavior of pure iron and carbon-manganese steels

Influence of chemical composition and microstructure on damage and crack initiation mechanism

Thèse présentée et soutenue publiquement le 30/01/2019

en vue de l'obtention du doctorat de Energétique, génie des procédés de l'Université Paris Nanterre

sous la direction de Mme. Danièle WAGNER (Université Paris Nanterre)
de M. Johann PETIT (Université Paris Nanterre)
et de Mme. Isabelle RANC (Université Paris Nanterre)

Jury:

Président	M. Bruno SERIO	Prof., Université Paris Nanterre, France
Rapporteur	M. Zhiyong HUANG	Prof. Sichuan University, China
Rapporteur	M. Nicolas RANC	Prof. Arts et Métiers Paris Tech, France
Eximinateur	M. Bastien WEBER	Arcelor Mittal Co., France
Eximinateur	M. Pierre JOLY	Framatome Co., France
Directeur	Mme. Danièle WAGNER	Prof., Université Paris Nanterre, France
Co-encadrant	M. Johann PETIT	Ass. Prof., Université Paris Nanterre, France
Co-encadrant	Mme. Isabelle RANC	Ass. Prof., Université Paris Nanterre, France

Abstract

This work attempts to a better understanding of the fatigue damage in ferrite-pearlite dual-phase steels in the Very High Cycle Fatigue (VHCF) domain. The influences of two parameters, namely pearlite phase percentage and free interstitial atoms content in solid solution, are investigated to deeply understand the dissipative mechanisms under 20 kHz high frequency fatigue loading. In-situ infrared thermography is carried out to record the temperature changes, while fractography studies and microscope observations are conducted to investigate the dissipative mechanism on the surface of specimens.

Classically, during a fatigue test, the specimen surface temperature at the beginning increases rapidly and then stabilizes. When the fracture occurs, after the crack initiation, the temperature increases very quickly. For the body centered cubic (BCC) materials, under high stress amplitudes, a sudden increase of the temperature occurs without a crack initiation and fracture.

The inevitable temperature increase up to hundreds of degrees at high stress amplitudes, is caused mainly by the screw dislocations mobility, which is one of the keys to explaining the observed fatigue behavior and thermal response of BCC structure under high frequency loading. Therefore, PSBs on surface and micro-voids in matrix emerge massively, accompanying with this abrupt temperature increase. These phenomena are considered as a transition of deformation mechanism from thermal regime to athermal regime. At low amplitudes, few PSBs or surface roughness are still observed on the specimen surface. By gathering the experimental data about cycles of PSB appearance on α-iron, it's found that PSBs are inclined to appear before 1×10^7 cycles, and PSB threshold lies below the conventional fatigue limit. The increase of pearlite phase content weakens the temperature elevation, and strengthens the fatigue properties.

The presence of free interstitial atoms in steels results in appearence of a secondary temperature increase in the stabilized temperature part (100-200 °C). This behavior seems to be related to the interaction of the edge dislocations with free interstitial atoms. Moreover, the remarkable hardening-softening-hardening phenomenon after the sudden temperature elevation to above 300 °C is thought as the interaction of multiplicated screw dislocations and free interstitial atoms.

***Keywords*:** Very high cycle fatigue, Ultrasonic fatigue, α-iron, Carbon steel, Thermography, Dynamic strain aging

Résumé

Ce travail tente de mieux comprendre les dommages par fatigue dans les aciers à deux phases ferrite-perlite dans le domaine de la fatigue à tres grand nombre de cycles (VHCF). Les influences de deux paramètres, à savoir le pourcentage de phase perlite et le contenu d'atomes interstitiels libres dans une solution solide, sont étudiées pour comprendre profondément les mécanismes de dissipation en 20 kHz en fatigue à haute fréquence. Une thermographie infrarouge in situ est réalisée pour enregistrer les changements de température, tandis que des études de fractographie et des observations au microscope sont menées pour étudier le mécanisme de dissipation à la surface des échantillons.

Classiquement, lors d'un essai de fatigue, la température de surface de l'échantillon au début augmente rapidement puis se stabilise. Lorsque la fracture se produit, après le début de la fissure, la température augmente très rapidement. Pour les matériaux cubiques centrés (BCC), sous fortes amplitudes de contrainte, une augmentation soudaine de la température se produit sans initiation de fissure ni fracture.

L'augmentation inévitable de la température jusqu'à des centaines de degrés aux fortes amplitudes de contrainte est principalement due à la mobilité des dislocations vis, qui est l'une des clés permettant d'expliquer le comportement en fatigue et la réponse thermique observée de la structure du BCC sous un chargement haute fréquence. Par conséquent, les PSB en surface et les micro-vides dans la matrice émergent en masse, accompagnant cette élévation abrupte de la température. Ces phénomènes sont considérés comme une transition du mécanisme de déformation du régime thermique au régime athermique. À faible amplitude, peu de PSB ou de rugosité de surface sont encore observés à la surface de l'échantillon. En rassemblant les données expérimentales sur les cycles d'apparition de PSB sur le fer armco, il a été constaté que les PSB étaient susceptibles d'apparaître avant 1×10^7 cycles et que le seuil de PSB était inférieur à la limite de fatigue conventionnelle. L'augmentation de la teneur en phase perlitique affaiblit l'élévation de la température et renforce les propriétés de fatigue.

La présence d'atomes interstitiels libres dans les aciers entraîne l'apparition d'une augmentation secondaire de la température dans la domain de la température stabilisée à 100 ℃ ~ 200 ℃. Ce comportement semble être lié à l'interaction des dislocations coins avec des atomes interstitiels libres. De plus, on pense que le phénomène remarquable de durcissement-adoucissement-durcissement après l'élévation soudaine de la température jusqu'à plus de 300 ℃ est l'interaction de dislocations à vis multipliées et d'atomes interstitiels libres.

***Motscl és*:** Fatigue à tr ès grand nombre de cycles, Fatigue ultrasonique, Fer armco, Acier au carbone, Thermographie, Vieillissement dynamique

Notation

PSBs	Persistent Slip Bands
IR	Infrared
N_f	Number of fatigue cycles
FGA	Fine Granular Area
YS	Yield stress
UTS	Ultimate Tensile Stress
E	Young's modulus
$\boldsymbol{b}$	Burgers vector
σ_a	Applied stress amplitude
R	Fatigue stress ratio
T	Temperature
T_{ini}	The ambient temperature
ΔT	Temperature elevation
T_0	The critical transition temperature
f	Frequency
C_p	Heat capacity at constant pressure
ρ	Density
k	Heat conductivity coefficient
h	Heat exchange coefficient
d_1	Intrinsic dissipation
$\tilde{d}_1$	Mean intrinsic dissipation in one cycle
S_{the}	Thermoelastic coupling
R	External volume heat source
$\dot{\varepsilon}$	Strain rate
σ_G	Athermal component of the flow stress
σ^*	Thermal component of the flow stress
τ	Time constant
Δ	Laplace operator
div	Divergence operator
$grad$	Gradient operator
EDS	Energy dispersive spectrometer

SEM	Scanning Electron Microscope
TEM	Transmission Electron Microscope
SP	Snoek Peak
SKKP	Snoek-Kê-Köster Peak
DSA	Dynamic Strain aging

Content Table

Introduction

Several decades ago, accidents caused by the unpredicted failure of metallic components (railways, vehicles, bridges, aircrafts and so on) often happened. Most of these accidents occurred by fatigue, that is to say, by the repeatability of the loading between a maximum stress and a minimum stress around a mean stress. In the year 1842, the event "Meudon railway disaster" (Bathias and Pineau, 2013) which killed at least 55 passengers was the first railway accident in France and one of the first in the world. This accident was due to the failure of a locomotive axle and the mechanism of crack was attributed to a repeated loading. Therein, the various ruptures due to repeated loadings in Germany urged August Wöhler to undertake a systematic study of this type of damage from 1852. The famous Wöhler curve or Stress amplitude-Number of cycles (S-N) curve was established (Wöhler, 1870; Mughrabi, 2006), including three domains: Low Cycle Fatigue domain (LCF) (below 10^4 cycles), High Cycle Fatigue domain (HCF) (10^4-10^7 cycles) and Very High Cycle domain (VHCF) (above 10^7 cycles). Historically, the VHCF domain corresponded to the domain of infinite endurance, and the stress amplitude for 10^6 to 10^7 cycles was related to the fatigue limit.

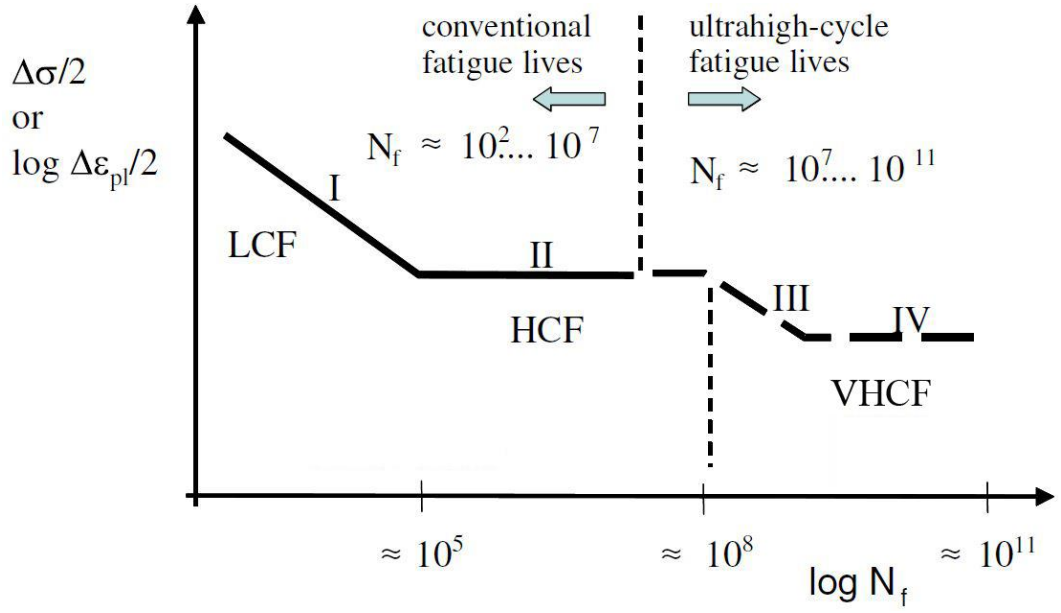

Figure 1 Schematic figure of S-N curve.(Mughrabi, 2006)

The requirement on materials fatigue performance is no longer limited below 10^7 cycles, but needs characteristics in very high cycle fatigue domain (10^7-10^{11} cycles). Low-frequency fatigue tests, as conducted in the past to establish the Wöhler curves, requires several weeks or months to complete the characterizing the fatigue properties up to 10^8-10^9 cycles. To

evaluate the fatigue life in an effective way is a challenging task to be solved by researchers all over the world. Under the pressure of time and economy, high-frequency fatigue tests become necessary, which makes it possible to obtain the materials properties in a reasonable time. To explore the domain beyond 10^7 cycles, a new generation of machines has been constructed. One of the pioneers was Claude Bathias (Bathias and Paris, 2005) who used the vibration of a piezoelectric ceramic devices which transforms an electrical signal into an ultrasonic mechanical wave allowing a loading frequency of 20 or 30 kHz. Until now, scholars have fruitfully published on the fatigue fracture mechanisms at high frequency cyclic loading. The observed fatigue fracture above 10^{10}-10^{11} cycles is contradictory to traditionally-defined fatigue limit in HCF, indicating that the VHCF domain has been neglected in a long period of time and needs to be paid more attention to. The relation between characteristics in fatigue initiation stage and fatigue strength still remains unclear.

In another aspect, low carbon steels always act as the most common engineering materials in fields of industry. Considering the strain rate- and temperature-dependent deformation behavior in body centered cubic structure in ferrous steels, the tests without cooling condition lead to an inevitable thermal phenomenon under high frequency fatigue loading, which is different from the traditional fatigue tests in low cycle or high cycle fatigue regime. Moreover, an abnormal and abrupt temperature increase appears above one certain stress amplitude. Some similar results about this abnormal thermal phenomenon have been published in ferrite-pearlite and ferrite-martensite steels (Huang, 2010; Ranc et al., 2015; Torabian et al., 2016; Ouarabi, 2018), but the underlying mechanisms are still not very clear. It requires more works to testify and clarify.

It is well-known that during mechanical loading in the plastic domain of metallic materials, a great part of the mechanical energy is transformed into heat. Even below the macroscopic yield stress, microplasticity occurs, accompanying with the specimen temperature increase. So, the temperature field recording on the specimen surface is an interesting technique to improve the understanding of the fatigue crack mechanisms.

So, in recent years, thermography method becomes very popular to rapidly and economically evaluate the fatigue properties, especially in LCF and HCF. As a non-destructive and non-contact technique, thermography could offer the useful temperature maps about crack initiation sites and crack propagation process. People are devoted to improving the data analysis method, with the aim that thermography can precisely predict fatigue properties such

as the fatigue limit after a given number of cycles through traditional fatigue tests. In HCF, temperature variation of self-heating tests present linear behaviors between applied stress and stabilized temperature. Does it still present linearly in VHCF? If not, there will be a puzzle to be solved about the fatigue limit and the underlying dissipative mechanisms.

Objectives of the thesis

With the challenges of this study, our objectives concern the VHCF domain and are summarized below:

- Better understanding of the fatigue behavior in dual-phase ferrite-pearlite steels by measuring the thermal response during tests.
- Investigating the influence of two microstructural parameters, namely the pearlite fraction and interstitial atoms percentage in solid solution, on the thermal response and fatigue behavior.
- Investigating the fatigue behavior of pure iron and dual-phase ferrite-pearlite steels by means of microscopic observations of the surface damage during fatigue tests as well as fractographic observations after tests.
- Determining the first signs of damage in fatigue crack initiation stage on pure iron through thermographic and microscopic observations of the specimen surface during self-heating tests.

This thesis involves four chapters whose subjects are briefly listed as following:

Chapter 1 introduces the general presentation of the body cubic centered ferrite-pearlite steels, the associated aging phenomena, the mechanisms of damage and initiation in fatigue (high, low and very low stress amplitudes) and self-heating methods in fatigue.

Chapter 2 displays the experimental devices used in this work. More particularly, the process of specimens design and the intrinsic dissipated energy calculation are exposed.

Chapter 3 talks about the influence of pearlite ratio on fatigue behavior under 20 kHz cyclic loading via thermography method, by means of in-situ microscope observations and fractographic observations. Moreover, the surface damages on α-iron under different stress amplitudes (high, low, very low) in fatigue crack initiation stage are displayed and discussed.

Chapter 4 discusses about the influence of interstitial atoms in solid solution on thermal response and fatigue behavior of steels. It shows the characteristics thermal response caused by the presence of dynamic strain aging phenomenon.

This thesis ends with the main conclusions of this research and the perspectives.

Chapter 1 Presentation and recent advances on fatigue and thermography of C-Mn steels

This chapter briefly introduces three aspects involved in my work.

Firstly, we begin to talk from the basic knowledge about crystal structure, thermal treatment of steels and hardening in steels. Therein, strain aging is introduced in details, especially dynamic strain aging. The effects of temperature and strain rate on BCC metals deformation mechanisms are very important to explain some experimental phenomena in following chapters.

Secondly, fatigue damage mechanisms are summarized, plastic deformation in crack initiation and formation of Persistent Slips Bands (PSB) are useful to understand the microstructure evolutions in chapter 3.

Thirdly, thermographic self-heating test is one of the most important topics in my work. The research status about fatigue relevant self-heating tests is summarized.

1.1 Alloys of iron-carbon

1.1.1 Defects and properties

The properties of materials are directly related to the crystal structure. Iron-based alloys are classic body-centered cubic (BCC) crystal structure as presented in Figure 1.1, which has a cubic unite cell with atoms located at all eight corners and a single atom at the cube center. The atomic packing factor (APF) of BCC structure is 0.68.

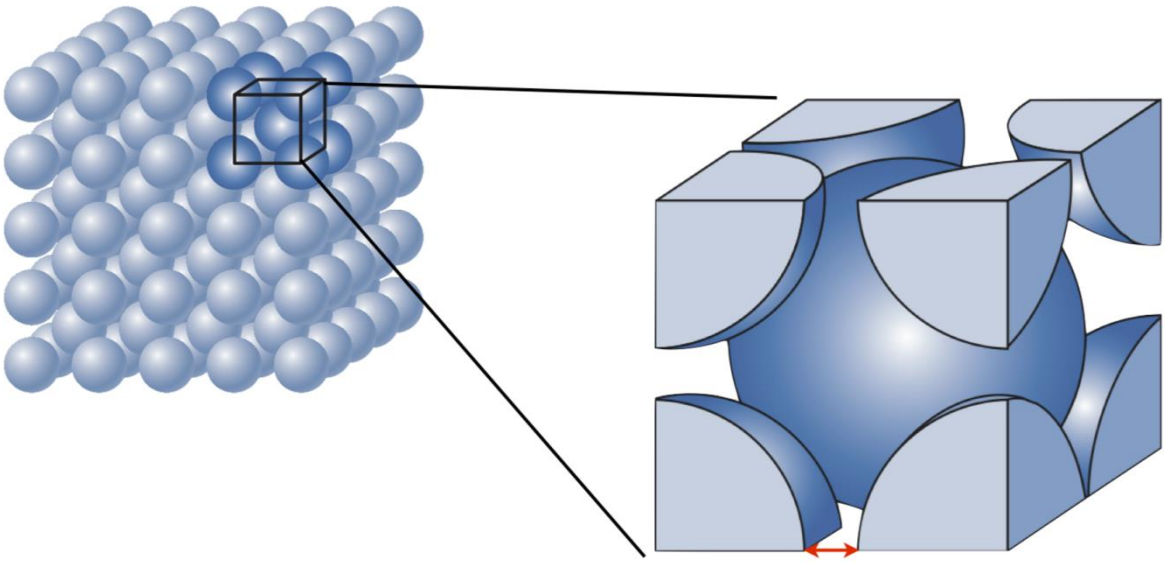

Figure 1.1 Schematic diagram of the body-centered cubic crystal structure. (Callister, 2007)

In the dense-arranged crystal structure, large numbers of various defects or imperfections always exist throughout the material at the atomic scale. The properties of materials are profoundly influenced by the presence of imperfections. It's important to summarize the imperfections that exist in steels. Classification of crystalline imperfections is frequently made according to geometry or dimensionality of the defect. It includes point defects (those associated with one or two atomic positions), linear defects (or dislocations), as well as interfacial defects, or boundaries, and volumic defects (precipitates, inclusions).

The most common of the point defects is a vacancy, site normally occupied by an atom which is missing. For most metals, the fraction of vacancy is on the order of 10^{-4} at the melting point and 10^{-15} at room temperature (Callister, 2015). The necessity of the existence of vacancies is explained using principles of thermodynamics: in essence, the presence of vacancies increases

the entropy of the crystal, and the relationship between the equilibrium number of vacancies and temperature agrees with the Arrhenius equation.

A dislocation is a linear or one-dimensional defect around which some of the atoms are misaligned. Edge dislocation (Figure 1.2a) is a linear defect centered around a line that is defined as the end of an extra half-plane of atoms. Within the region around the dislocation line there is some localized lattice distortion. The magnitude of this distortion decreases with the distance away from the dislocation line; at positions far removed, the crystal lattice is virtually perfect. Screw dislocation also exists, which may be thought of as being formed by a shear stress that is applied to produce the distortion shown in Figure 1.2b. The upper front region of the crystal is shifted by one atomic distance to the right relative to the bottom portion.

Most dislocations found in crystalline materials are probably neither pure edge nor pure screw, but exhibit components of both types; these are termed mixed dislocations. Virtually all crystalline materials contain some dislocations that were introduced during solidification, by plastic deformation, or as a consequence of thermal stresses that result from rapid cooling.

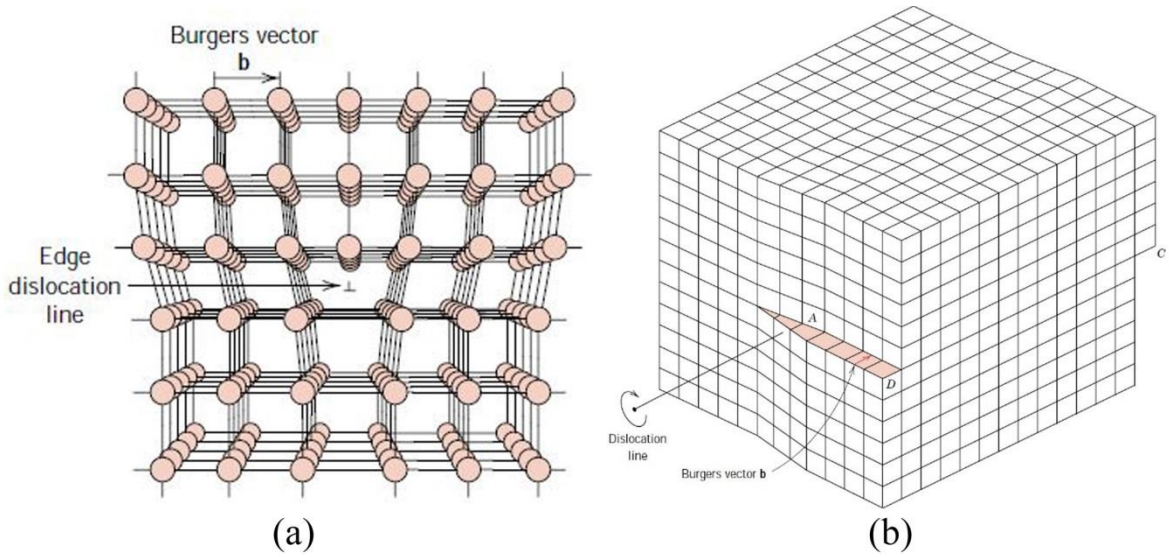

Figure 1.2 Schematic diagrams of (a) an edge dislocation and (b) a screw dislocation within a crystal. (Guy, 1976; Callister, 2015)

The nature of a dislocation (i.e., edge, screw, or mixed) is defined by the relative orientations of dislocation line and Burgers vector. For an edge, they are perpendicular, whereas for a screw, they are parallel; they are neither perpendicular nor parallel for a mixed dislocation.

Dislocations can be observed in crystalline materials using electron-microscopic techniques. Under the view of transmission electron micrograph, the dark lines are the dislocations, as shown in Figure 1.3.

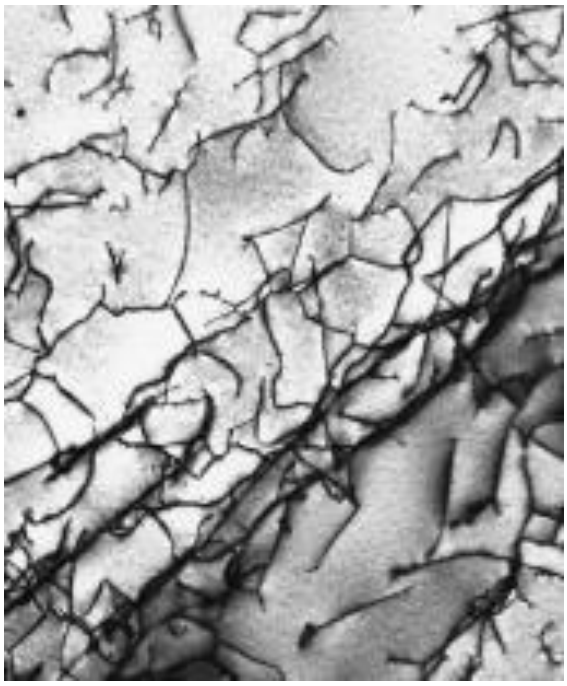

Figure 1.3 A transmission electron micrograph of a titanium alloy in which the dark lines are dislocations. 51,450×. (Callister, 2015)

Interfacial defects in BCC structure concern imperfections, such as external surfaces, grain boundaries, twin boundaries, stacking faults, and phase boundaries.

Even with relatively sophisticated techniques, it is difficult to refine metals to the absolute purity. Most familiar metals are not highly pure; rather, they are alloys. People add additional atoms intentionally to achieve some specific mechanical characteristics. The addition of foreign atoms to a metal will result in the formation of a solid solution and/or a new second phase, depending on the kinds of additional atoms, their concentration and the temperature.

1.1.2 Heat treatment of steels

A portion of the iron-carbon phase diagram is shown in Figure 1.4. Iron-alloys below 2% carbon content are called steels, but practically the carbon content is lower than 1% in weight.

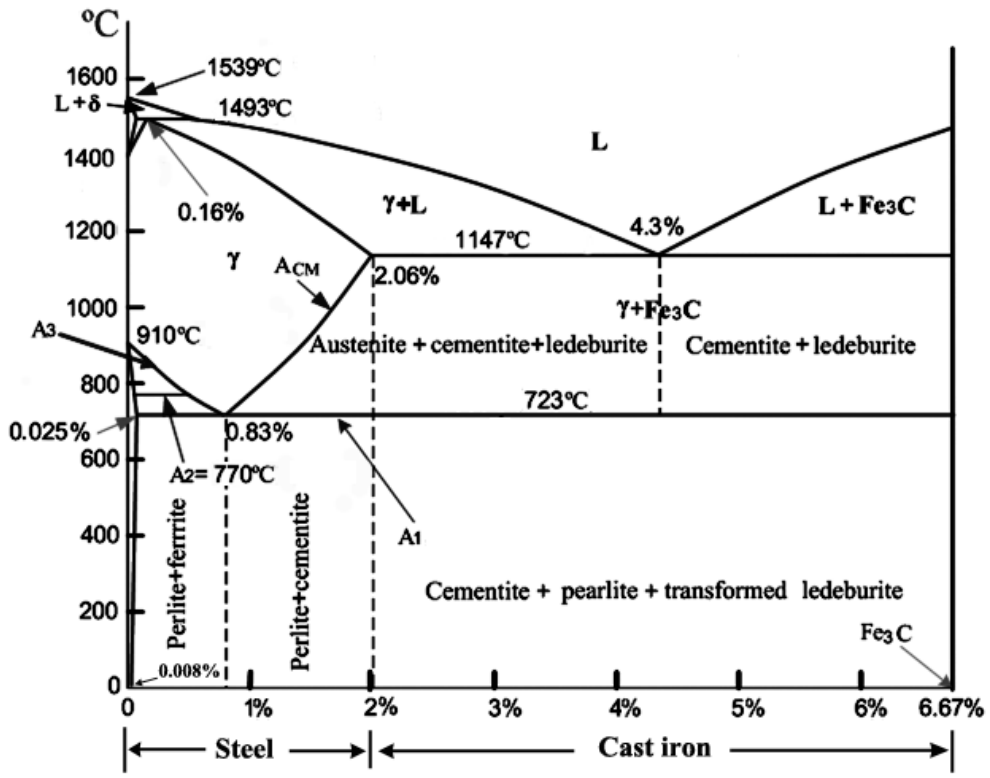

Figure 1.4 Phase diagram for carbon steels.(Thomas and Samuel, 1960)

According to the temperature and the process, heat treatment can be classified into four methods: normalizing, quenching, tempering, annealing. The Figure 1.5 gives the applied temperature in each case.

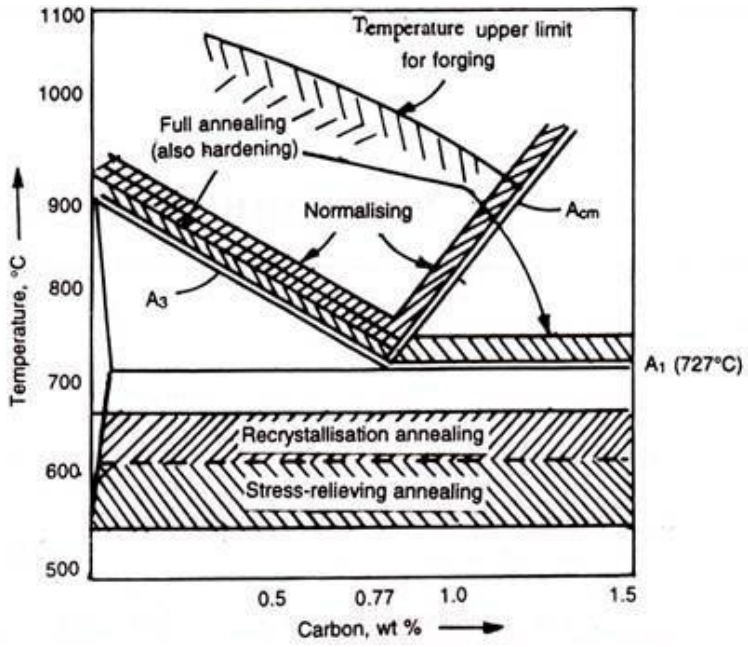

Figure 1.5 Temperature ranges of the heat treatments on Fe-Fe_3C diagram. (Thomas and Samuel, 1960)

- Normalizing is a process in which a steel is heated to a temperature above the A_3 and then cooled in still air. The purpose of the treatment is to obliterate the effects of any previous heat treatment or cold-work and to insure a homogeneous austenite on reheating. The resultant structures depending upon the composition of the steel are:

  - ferrite for pure α-iron or ferrite with secondary cementite for alloys with few ppm of carbon
  - proeutectoid ferrite and pearlite for hypoeutectoid steels ($0.0022\% < C < 0.77\%$)
  - pearlite for the eutectoid steel (0.77% of carbon)
  - proeutectoid cementite and pearlite for hypereutoid steels ($0.77\% < C < 1\%$)

  The pearlite is composed by eutectoid ferrite and lamellar cementite Fe_3C (alternate lamella of ferrite and cementite). The morphology of pearlite depends on the cooling rate.

- Quenching is a process to produce hardening by a rapid cooling, in order to prevent undesired phase transformation at low temperature. Quenching mediums commonly used are oil, water, salt bath and so on, according to their ability to cool steels. Quenching improves the strength and hardness of steels, by introducing martensite or bainite phase.

- Annealing is a process involving heating and cooling, usually applied to produce softening. The temperature and the rate of cooling depend on the compositions of materials being annealed and the purpose of the treatment. Usually, annealing includes full annealing, process annealing and spheroidizing. Full annealing is a softening process in which a steel is heated to a temperature below the transformation range (A_1). Recrystallization annealing is applied to cold-worked low carbon steels (< 0.25% carbon). If the steel is not to be further cold-worked, but relief of internal stresses is desired, a lower range of temperature will suffice (about 540 ℃). Rate of cooling is immaterial. This type of annealing will cause recrystallization and softening of the cold-worked ferrite grains, but usually will not affect pearlite. Spheroidizing annealing is a process of heating and cooling to produce a rounded or globular form of carbide cementite Fe_3C in a matrix of ferrite (globular pearlite). It is usually accomplished by prolonged heating at temperature just below the A_1 (Thomas and Samuel, 1960). This treatment is usually applied to the high carbon steels (≥ 0.60% of carbon).

- Tempering is a process of reheating quenching-hardened steels to some temperature below the lower critical temperature A_1. The rate of cooling is basically immaterial except for some special alloys. Tempering temperature is a very important parameter, which depends upon the desired properties and the purposes for which the steel is to be used.

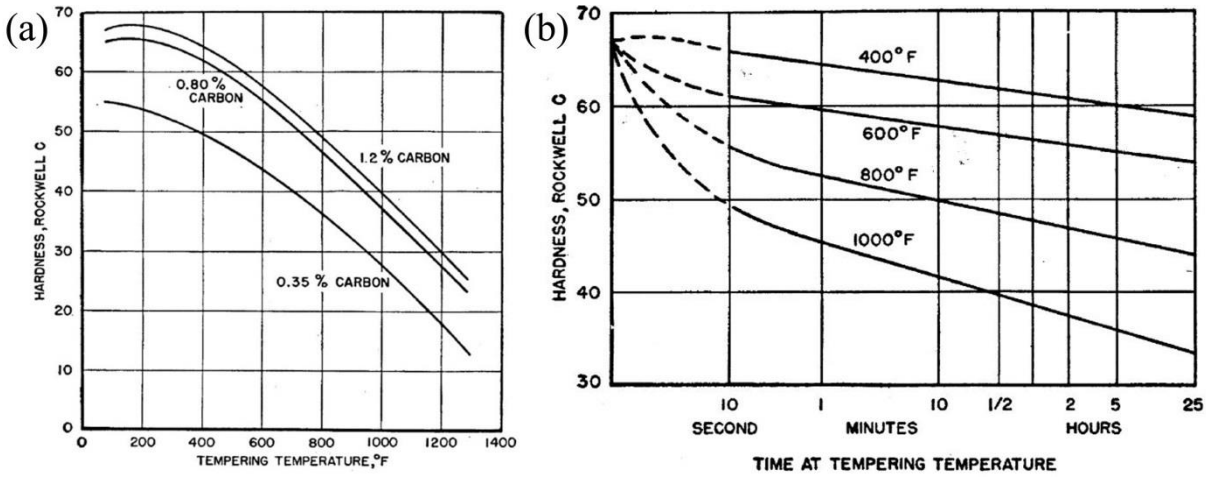

Figure 1.6 (a) Effect of tempering temperature on the hardness of carbon steels of different carbon content when tempering time is 1 hour, (b) Effect of time at tempering temperature on the hardness of 0.8% carbon steel when tempering time is 1 hour. (Bain, 1939)

Tempering will not produce phase transformation, but it affects microstructure transformation. Microstructure transformation closely depends on tempering temperature, involving carbides and nitrides precipitation, aggregation, recovery, α-phase recrystallization and cementite morphology. As the tempering temperature is increased, the martensite of hardened steel passes through stages of tempered martensite and is gradually changed into a structure consisting of spheroids of cementite in a matrix of ferrite, formerly termed sorbite. Proper tempering requires a certain amount of time. The tempering temperature and duration greatly influence the hardness, as explained in Figure 1.6. (Bain, 1939)

1.1.3 Plastic deformations and strengthening mechanisms

All metals initially contain an appreciable number of dislocations from the growth of the crystals, dislocation number can be reduced through thermal treatment, but even well-annealed crystals usually contain a network of dislocations. The most common plastic strain mechanism is due to the dislocation gliding on the close packed planes. During the loading, the hardening comes from the intersection of the dislocations with obstacles:

- pre-existed dislocations forest from the strain hardening
- solute atoms in solid solution
- precipitates and grain boundaries

Only the phenomena due to the intersection of the dislocations (strain hardening) or due to the solute atoms are presented in this section.

Strain Hardening

The phenomenon whereby a ductile metal becomes harder and stronger as it is plastically deformed is called strain hardening or work hardening. It is sometimes convenient to express the degree of plastic deformation as percent cold work rather than as strain. Percent of cold work (%CW) is defined as (1.1) (Callister, 2015):

$$\%CW = \left(\frac{A_0 - A_d}{A_d}\right) \times 100\% \qquad (1.1)$$

where A_0 is the original area of the cross section that experiences deformation, and A_d is the area after deformation.

Most metals can get a higher yield stress and tensile strength with increasing cold work percent. The influence of cold work on the stress-strain curve of a low carbon steel is vividly portrayed in Figure 1.7 (Bardes, 1978; Callister, 2015). The strain hardening phenomenon is explained by the dislocation-dislocation intersections. The dislocation density in a metal increases with deformation, due to dislocation multiplication or the formation of new dislocations. Consequently, the average distance of separation between dislocations decreases, that is, the dislocations are positioned closer together. On the average, dislocation–dislocation interactions are repulsive, because two attractive dislocations can counteract the lattice strains by dislocations annihilation. The net result is that the motion of a dislocation is hindered by the presence of other dislocations. As the dislocation density increases, this resistance to dislocation motion by other dislocations becomes more pronounced. Thus, the imposed stress necessary to deform a metal would increase with increasing cold work.

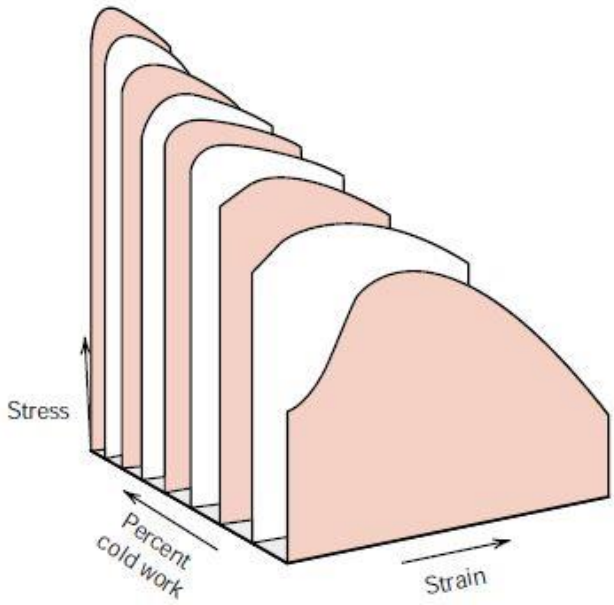

Figure 1.7 Schamatic illustration about influence of cold work on the stress–strain behavior for a low carbon steel. (Bardes, 1978)

Strain hardening is often utilized commercially to enhance the mechanical properties of metals during fabrication procedures. The effects of strain hardening may be removed by an annealing heat treatment.

Solid solution strengthening

Except the hardening from plastic deformation, the common technique to strengthen metals is alloying with foreign atoms that go into either substitutional or interstitial solid solution. Substitutional atoms are larger than host atoms, for which it exerts compressive strains on the surrounding lattice, as in Figure 1.8a. Conversely, the smaller substitutional atoms impose tensile strains in their vicinity, as illustrated in Figure 1.8b. Both the larger and smaller interstitial atoms than solute atoms, the interstitial atoms will impose the compressive strains on the surrounding atmosphere, because they are always larger than the available free space in the lattice. Owing to the presence of solute atoms, alloys are stronger than pure metals, because the lattice strain field interactions between foreign atoms and dislocations will restrict dislocations movement.

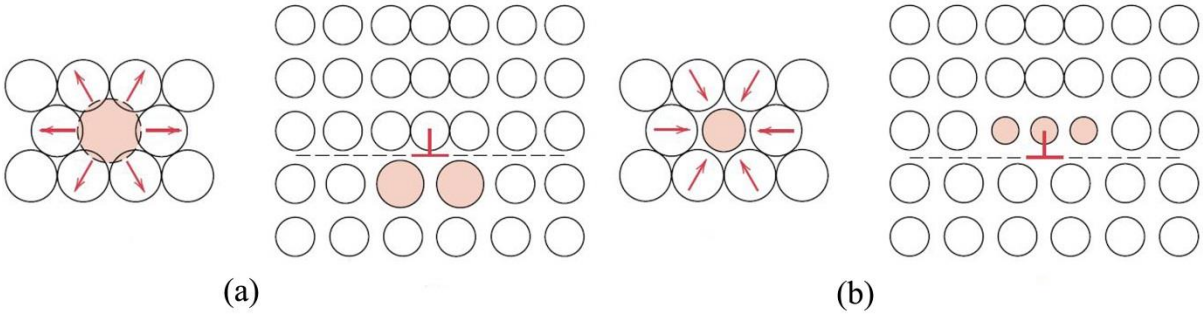

Figure 1.8 Representation of strains imposed on host atoms by (a) a larger substitutional atoms and the corresponding possible locations of foreign atoms beside an edge dislocation such that there is partial cancellation of lattice strains; (b) the case of a smaller substitutional atom. (Callister, 2015)

Two well-known phenomena related to solid-solution strengthening are the Portevin-Le Chatelier effect (PLC) and Lüders bands. The Lüders bands is described more precisely in next section which presents the all aging phenomena due to the interaction dislocation-solute atoms susceptible to operate in dual phase steels.

1.1.4 Aging of carbon manganese steels

Lüders bands

For the ferrite/pearlite and ferrite martensite steels, the tension curve (Figure 1.9) presents a plateau (Lüders strain) with an upper and lower yield stress (Baird, 1971; Johnson, 2012). With the help of straining, the interstitial solute atoms diffuse easily in the matrix and locate preferentially near the dislocations. The dislocations are anchored and cannot move. As the plateau is not completed, the strain along the specimen length is not homogeneous and the strain propagates by bands.

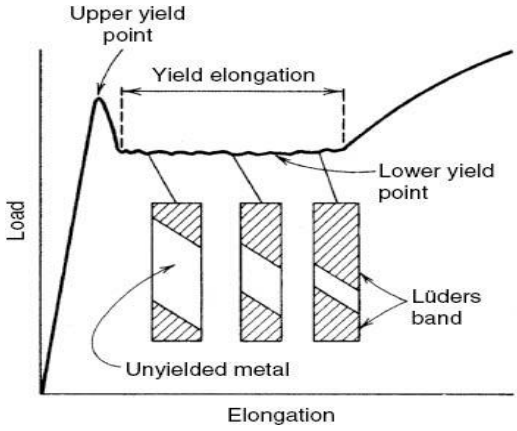

Figure 1.9 Schematic diagram of Lüders bands.

Static Strain Aging (SSA)

Static Strain Aging (SSA) is a phenonmenon in process of reloading, after unloading during homogeneous plastic deformation (after Lüders bands), ageing at a 200 °C for some time, and then reloading. This results in the return of the Lüders strain phenomenon. (Baird, 1971)

Dynamic Strain Aging (DSA)

In the Dynamic Strain Aging (DSA) phenomenon, the aging is sufficiently rapid to occur during straining. In this case, for the materials rather sensitive to the DSA, the localization of the strain is characterized in a tensile test by the formation and the propagation of plastic strain bands called Portevin-Le Chatelier bands (PLC bands). During a tensile test at imposed strain rate, DSA phenomenon is associated with serrations on the stress-strain curve (Ranc and Wagner, 2007; Ranc et al., 2016), as in Figure 1.10. Each stress drop on the tensile curve corresponds to the formation of a band. At a microscopic strain, this phenomenon is explained by the interaction of mobile dislocations with the interstitial solute atoms. The dislocation gliding is not continuous, but discontinuous (McCormigk, 1972; Mühlhaus et al., 1995).

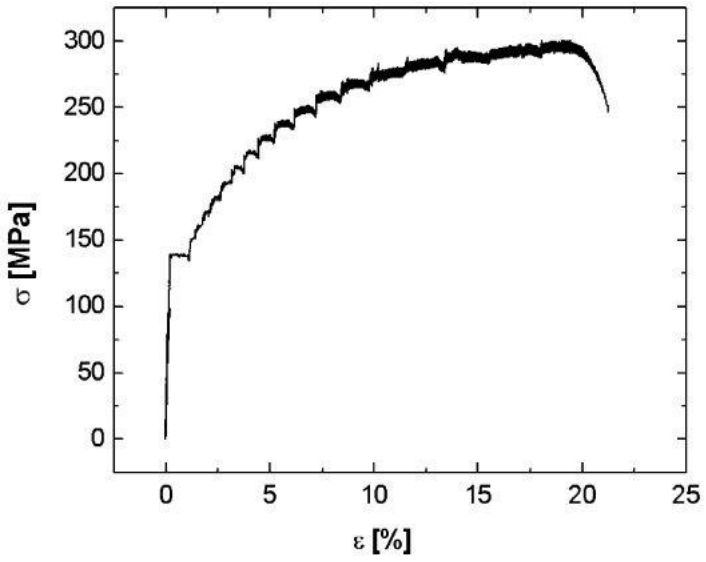

Figure 1.10 Schematic diagram of Portevin-Le Chaterlier effect. (Chmelík et al., 2007)

DSA in solid solution is described as the diffusion of solute atoms towards the mobile dislocations, which are temporarily arrested at obstacles. A dislocation segment has to wait for a certain time t_w until the obstacles are overcome. After that, it moves to the next obstacles. During the waiting time, solute atoms (such as carbon, nitrogen for C-Mn steels) diffuse

around the dislocations further strengthening the obstacles. Then dislocations move with sufficient stress and will stops at new obstacles. The process can repeat. (Beukel, 1975)

At a constant strain rate, the stress dislocations required to move will increase, due to DSA. The solute atoms diffusion is dependent on temperature and the dislocation speed on strain rate. So, the waiting time t_w is directly related to temperature and strain rate. Therefore, DSA is sensitive to strain rate and temperature. The phenomenon is active in a certain domain of strain rate (which imposes the dislocations speed) and temperature (which imposes the diffusion of solute atoms). In C-Mn steels, the DSA phenomenon occurs for common strain rate in a temperature range of 100-300 ℃.

DSA effect can occur in many metal alloys, C-Mn steels (Wagner et al., 2006; Huang et al., 2015), forging steels (Lee and Kim, 1995), austenitic stainless steels (Sarkar et al., 2018), and so on. In C-Mn steels, it is well established that the atoms which interact with dislocations are carbon and nitrogen. According to its greater solubility limit, nitrogen seems to exert a more pronounced influence on aging than carbon does (Baird, 1971; Marschall et al., 1990).

Previously, this DSA phenomenon has been extensively studied on two ferrite/pearlite steels (Moreno, 1998) with different sensitivity to DSA: one A48 steel (French standard) sensitive to DSA and one A42 steel nearly insensitive to DSA. This DSA phenomenon induces an increase in flow stress, ultimate tensile strength (UTS) and work hardening coefficient (Wagner et al., 2006), as well as a decrease in ductility (elongation, reduction of area and fracture toughness) (Wagner et al., 2002). The Figure 1.11 gives the UTS evolution with temperature of these two steels. It is clearly displayed that the DSA effect operates from 100 ℃. On the conventional tensile curves, the DSA effect is exhibited at both 100 ℃ and 200 ℃ for the A48 steel, whereas for the A42 steel, no serrations resulting from DSA effect are visible (Moreno, 1998).

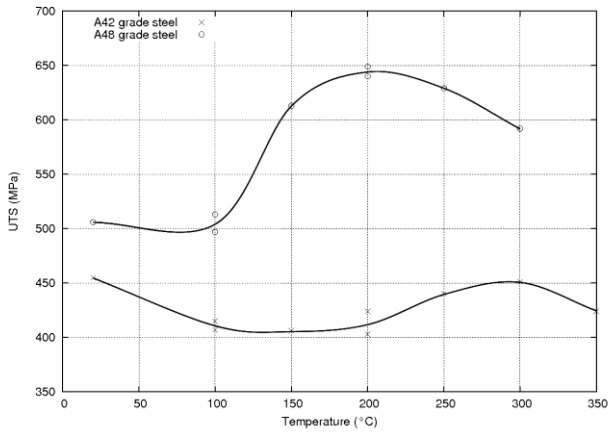

Figure 1.11 Ultimate tensile strength versus temperature for A48 and A42 steels.(Wagner et al., 2002)

On the other hand, the upper shelf level Charpy V-notch results remain unchanged and are not affected by the DSA phenomenon (Wagner et al., 2002). This is due to the high strain rate of Charpy V-notch tests, for which the C and N atoms diffusion is too slow compared to the dislocations speed. In the Low Cycle Fatigue tests (LCF) (Huang et al., 2015), at room temperature, the hysteresis loop (stress amplitude-strain amplitude) does not show serrations, whereas from 100 ℃ whatever the material (A48 or A42), it appears serrations in the plastic domain (Figure 1.12).

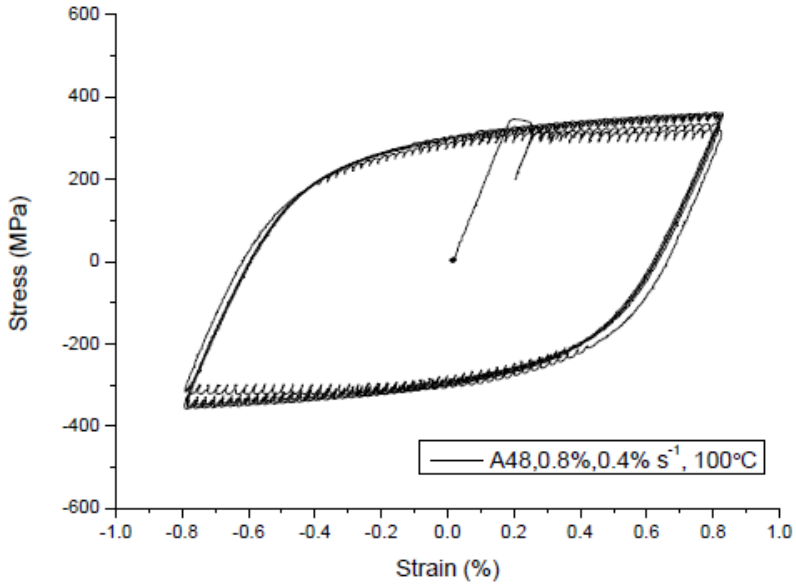

Figure 1.12 Hysteresis loop for A48 steel at 100 ℃ (0.8% strain amplitude, 0.4% s^{-1} strain rate). (Huang et al., 2015)

The evolution of the maximum stress amplitude with the number of cycles (Figure 1.13) presents a first hardening followed by a stabilization and a second hardening. The first hardening is due to the cyclic strain hardening whereas the second hardening is attributed to DSA.

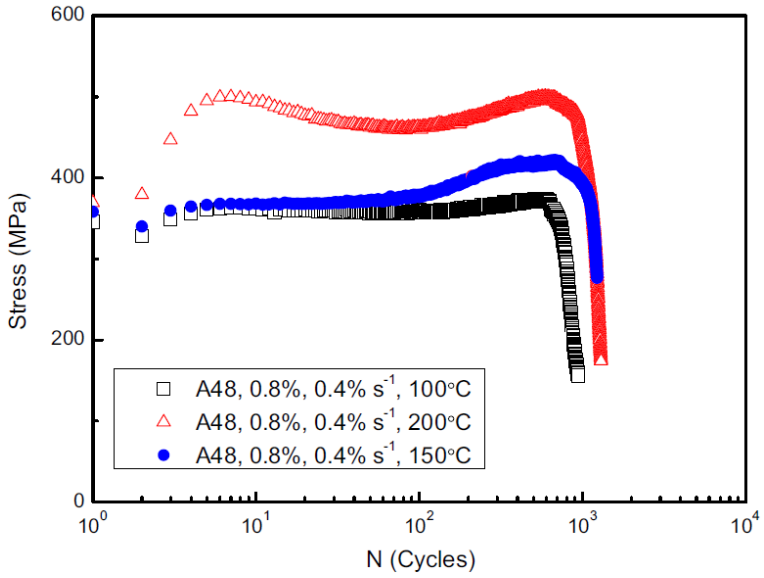

Figure 1.13 Stress evolutions during the test for the A48 steel at 100 ℃, 150 ℃, 200 ℃ (0.4% s^{-1} strain rate). (Huang et al., 2015)

In the literature (Huang et al., 2015), a strong effect of the strain rate is reported for the LCF tests. For the C-Mn steels, it seems that the DSA enhances the fatigue life. Lee and Kim (1995) found the dynamic strain aging was easy to initiate the crack, while crack propagation was retarded by crack branching. Hence, the dynamic strain aging caused the improvement of fatigue resistance (Torabian et al., 2017).

1.1.5 BCC temperature-dependent mechanism

BCC metals have a different behavior as FCC metals. They are more susceptible to strain rate and temperature. Flow stress is defined as the instantaneous value of stress required to continue plastically deforming the material (Mikell P. Groover, 2007). The flow stress $\sigma(\mathrm{T}, \dot{\varepsilon})$ of BCC metals depends on strain rate $\dot{\varepsilon}$ and temperature T, and it can be written as the sum of an athermal stress σ_G and a thermal stress $\sigma^*(\mathrm{T}, \dot{\varepsilon})$:

$$\sigma(\mathrm{T}, \dot{\varepsilon}) = \sigma_G + \sigma^*(\mathrm{T}, \dot{\varepsilon}) \qquad (1.2)$$

At the same temperature, flow stress would increase non-linearly with increasing strain rate. At the same strain rate, flow stress would decrease with increasing temperature, i.e. $\sigma \propto \dot{\varepsilon}$, and $\sigma \propto 1/\mathrm{T}$. Figure 1.14 is the stress-strain curves for carbon steels (0.125% Carbon) at various temperatures for the quasi-static and dynamic strain rate. As with other BCC metals, flow stress is controlled by the combination of strain rate and temperature, and more dependent on the temperature than strain rate.

Mughrabi (2009) described the temperature-dependent deformation of BCC metals by a schematic diagram as shown in Figure 1.15. For a given strain rate, flow stress decreases as the temperature rises and levels off to athermal stress σ_G. The critical temperature from thermal stress to athermal stress is the transition temperature T_0. The deformation mechanisms are classified by the transition temperature T_0. Below the transition temperature T_0, it's named as "thermally activated regime" or "thermal regime", and above T_0, it's called "athermal regime". Below T_0, at low temperature, the screw dislocations are nearly immobile and the dislocation glide mainly occurs by the to-and-fro glide of edge dislocations. Above T_0, the mobilities of edge and screw dislocations become comparable and screw dislocations can cross slips easily.

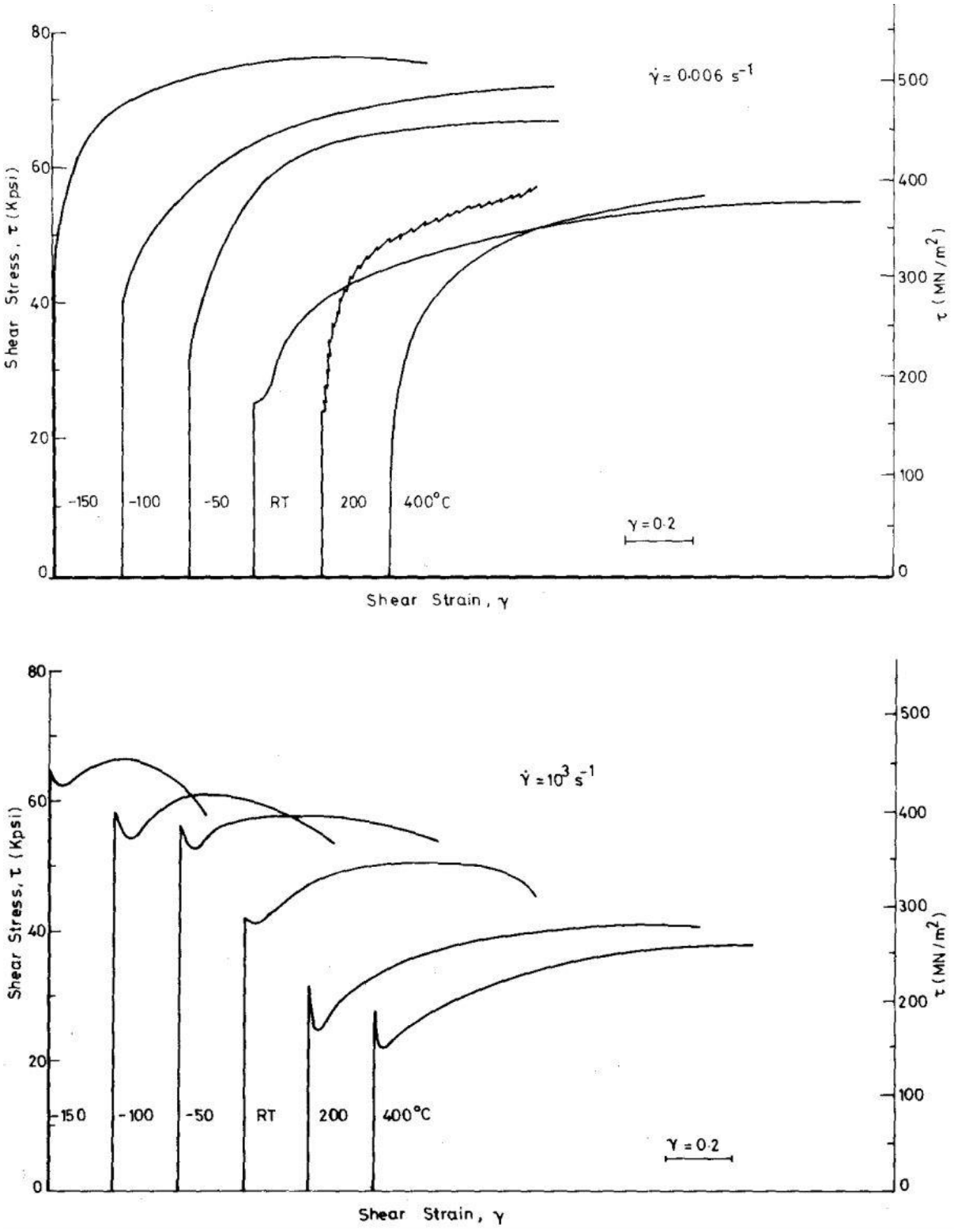

Figure 1.14 The stress-strain curves of a mild steel (containing 0.125% carbon) under different strain rate and temperature. (Abdel-Salam M. Eleiche, 1981)

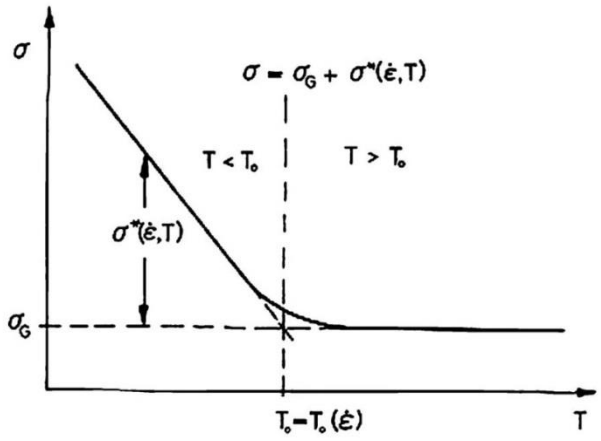

Figure 1.15 Schematic diagram of flow stress of BCC metals versus temperature (Mughrabi, 2009).

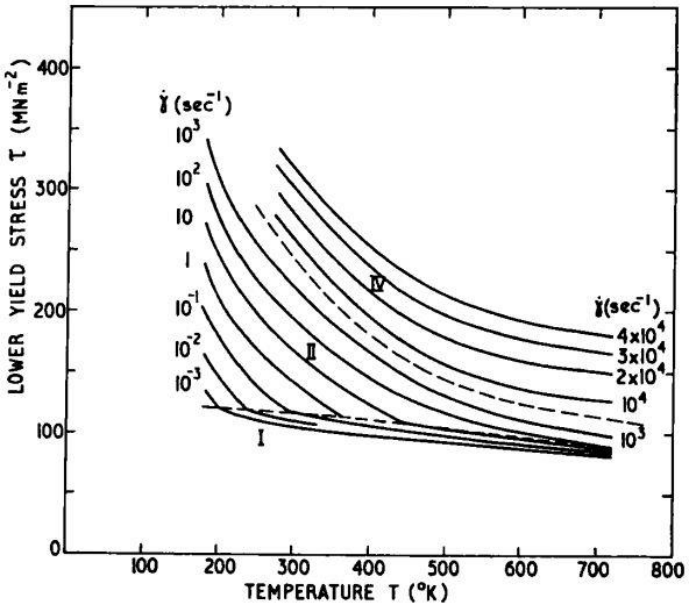

Figure 1.16 The variation of flow stress (shear stress) with temperature under a series of strain rate, for mild steel (0.12% carbon), measured by Hopkinson-bar apparatus.(Campbell and Ferguson, 1970)

Figure 1.16 is the flow behavior diagram of 0.12 wt% carbon steel given by Campbell and Ferguson (1970). Under each strain rate, flow stress presents the similar curve as Figure 1.15. T_0 increases from 25 ℃ to 100 ℃ (or about 300 K to 370 K) with strain rate from 0.01 s^{-1} to 1 s^{-1} and continue increasing above 200 ℃ when the strain rate reaches 100 s^{-1}. For a steel, the transition temperature T_0 is affected by strain rate.

1.2 Fatigue crack mechanism

On the Wöhler curve we can see four stages, as shown in Figure 1.17. The upper region (above the red curve) corresponds to the conditions in which the specimens are broken. The lower region below the red curve corresponds to the cases of unbroken specimens. Within the area directly below the red curve, we can see three new regions: region I is related to cyclic hardening or softening in strain localization processes, region II corresponds to the initiation of a crack, and region III is associated with the propagation of this crack. The number of corresponding cycles in region II and region III being N_i and N_p, respectively. The ratio between both varies according to the number of cycle to failure. The proportion of initiation in whole fatigue life is not same in LCF, HCF and VHCF. In general, N_i represents the majority part of the lifetime when the applied stress amplitude becomes lower and the number of cycle to failure is higher. The detailed discussion is in the following section: the region I corresponds to the dislocation structure evolution with the Persistent Slips Bands (PSB) appearance, the region II corresponds to the crack iniation part, and the region III to the crack propagation.

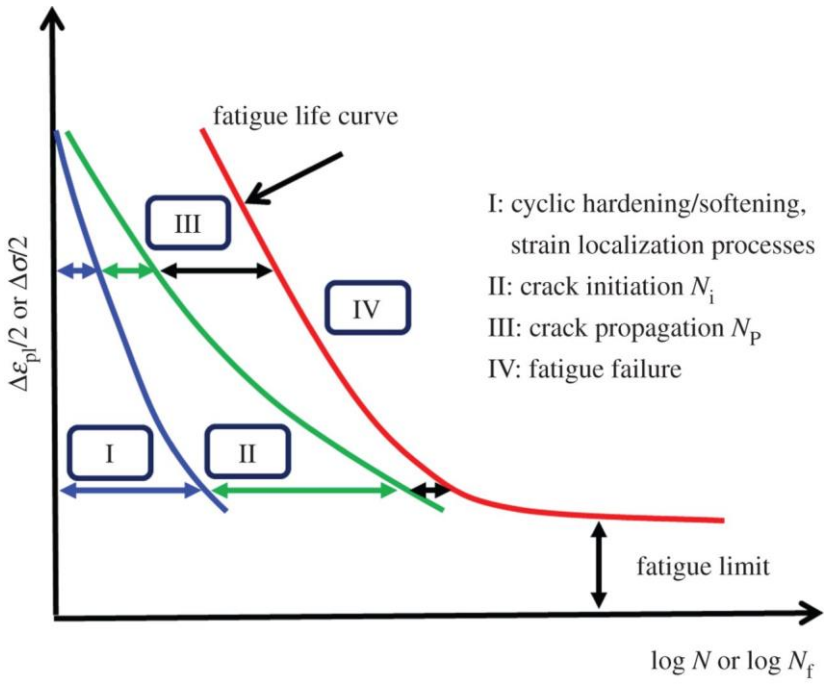

Figure 1.17 Schematic illustration of the four stages of fatigue ductile metals until failure.(Mughrabi, 2015)

1.2.1 Fatigue damage mechanism: Dislocation configurations and Persistent Slips Bands (PSB)

<u>High stress amplitudes (LCF-HCF)</u>

- FCC metals

The evolution of the dislocation structure, is closely related to the cyclic deformation mechanism, and is responsible for the fatigue damage. For the FCC single crystal copper, a Cyclic Stress-Strain (CSS) curve was established at different strains, as shown in Figure 1.18 (Winter, 1974; Mughrabi et al., 1979), where τ_s is the shear stress on the slips plane and γ_{pl} the resolved shear strain. This curve shows 3 domains.

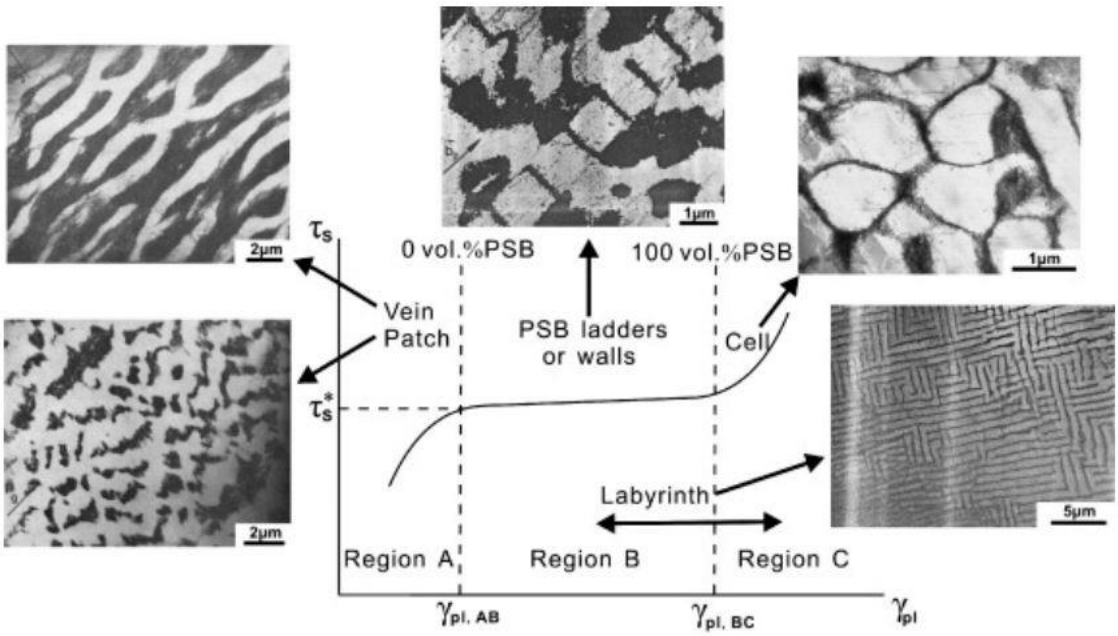

Figure 1.18 Cyclic stress-strain curve and dislocation patterns (TEM photos) in copper single crystal. (Winter, 1974; Mughrabi et al., 1979)

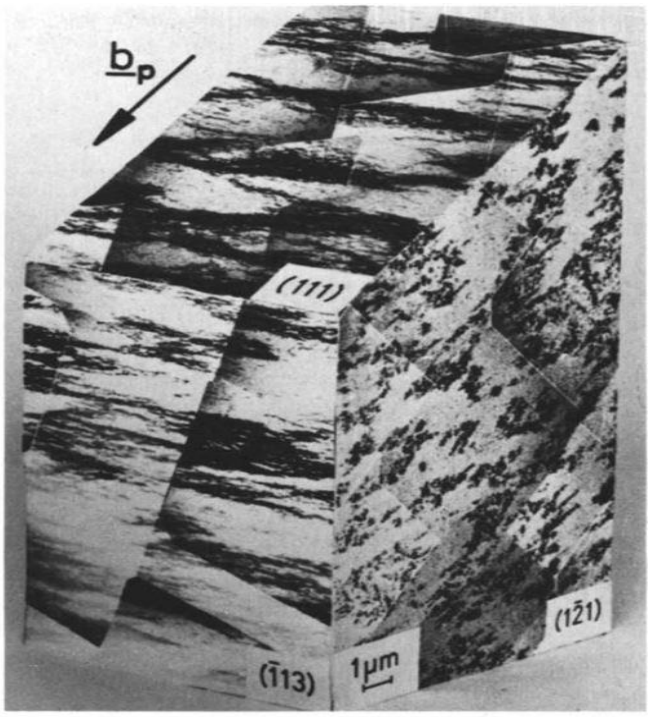

Figure 1.19 Three-dimensional views of loop patches corresponding to region A of the cyclic stress-strain curve. (Laird et al., 1986)

In region A, at low stresses and strains, hardening occurs for this material. This is due to the formation of bundles of dislocation dipoles dominated by primary dislocations. These are termed “loop patches”. Their three dimensional TEM morphology can be found in Figure 1.19. Observed from different slip plans, the TEM morphology looks like “veins” or “patches”. With increasing the strain amplitude, the loop patches become denser, and higher saturation stresses are required to accommodate the plastic strain.

In region B, the occurrence of plateau accompanied by the formation of the Persistent Slips Bands (PSB) provides good evidence that, in this case, the matrix structure breaks down and is converted into the "wall" or "ladder" structure of the PSBs which are softer, and in which the strain concentrates subsequently. From $\gamma_{pl,AB}$ to $\gamma_{pl,BC}$ (6×10^{-5} to 7.5×10^{-3}), the specimen is filled progressively with PSBs. At $\gamma_{pl,BC}$, the volume fraction of PSBs in the single crystal is nearly 100% (Suresh, 1998). Materials under cyclic loading would produce slip bands due to strain localization, therein, persistent slips bands in region B have been most intensively studied, which owns a characteristic structure, some extrusions above the surface and some intrusions below the surface. As to the source of its naming, it is established that locations of

the bands remain visible after electro-polishing (Thompson and Wadsworth, 1958), suggesting that they are structurally different from surrounding material. If the fatigue test is continued after polishing, the slip activity re-occurs at the same locations. That is why these bands were termed Persistent Slip Bands.

In region C the transformation observed prior to saturation is attributed to dislocation rearrangement affected by the to-and-fro glide of dislocations after the quick initial build-up of stress. These rearrangements are not confined to localized bands as in region B, and lead to the formation of structures similar to kink bands, as indicated by the surface pattern, TEM, and X-ray tomography. (Laird et al., 1986; Li et al., 2009). In region C, when $\gamma_{pl} > \gamma_{pl,BC}$, secondary slips originate at the PSBs martrix interface and leads to a cell structure which fills the PSBs.

In region A and C, only single-phase dislocation structures appear. A two-phase dislocation structure consisting of PSBs embedded in a vein matrix is characteristic for plateau region B. PSBs are zones of highly activity. The cyclic plastic strain amplitude within the PSBs is higher than that in the matrix.

The plateau region B of the cyclic stress-strain curve in single crystals, reflects the behavior of the PSBs as a matrix phenomenon. Similar features are absent in the case of polycrystals where PSBs remain confined to the surface grains. Typically, the cyclic stress-strain curve of FCC polycrystals exhibits a continuous increase of the saturation stress with increasing plastic strain amplitude (Bhat and Laird, 1978; Zhang and Wang, 2008). The formation of PSBs in individual surface grains of favourable orientation still is presumably very similar to that in single crystals orientated for single slip. For the FCC polycrystals alloys, precipitates, inclusions, grain boundaries and different solid solution for commercial alloys, as well as initial condition (annealed or cold-worked) modify the dislocation structure evolution during cycling loading (Suresh, 1998). But above all, the types of dislocations substructures depend very strongly on the strain amplitude, the stacking fault Energy (SFE) and to a small extent, on the temperature (Lukáš and Klesnil, 1973). Indeed, when the SFE is high, the cross-slip screw dislocations are favored and the gliding is wavy. When the SFE decreases, the slips offsets becomes straight and the gliding is planar (Suresh, 1998).

◆ BCC metals

As reported in Section 1.1.5, the dislocation behaviors of BCC metals differ from the FCC metals as follows (Suresh, 1998; Mughrabi, 2009):

- At low temperature ($T < T_0$) and low plastic strain amplitudes, thermally-activated glide of screw dislocations as well as screw dislocations multiplication are suppressed.

- The flow stress is strongly strain-rate dependent. So, the CSS curve must be obtained at the same strain rate for all the curve data.

- The glide of screw dislocations occur on different glide planes in tension and in compression at low temperature leading to the "slip plan asymmetry".

The dislocation structures of BCC metals are reasonably similar to those of FCC metals only under conditions which allow the mobilities of screw and edge dislocations to be similar. For BCC metals, the cyclic stress-strain curves do not have similar relation to the dislocation structures as FCC metals. Figure 1.20 is the cyclic stress-strain curve of polycrystalline iron with mean grain size of 80 μm. The shape of its cyclic stress-strain curve for BCC metals is similar to that for FCC metals. For BCC polycrystalline iron, it's verified that almost no dislocation arrangement is found in region A (Figure 1.20), despite some gliding primary screw dislocations, debris loops and a few secondary dislocations. In region B, the loop-patch structure prevails, whose structure should be identical to FCC metals. If the strain amplitude is kept at the upper limit of region B, a few dislocation walls and dislocation cells larger than 2 μm can also be found, but these structures have no significant effect on the fatigue failure. In region C, the dislocation cells smaller than 2 μm rapidly developed.

Apparently, for FCC metals, the plateau of the curves is relevant to the PSBs structure. Although this cyclic stress-strain curve (Figure 1.20) could reflect the dislocation structure, the appearance of PSBs has no relation to CSS curves for BCC metals.

For pure α-iron, no PSBs similar to those of fatigued FCC metals have been identified. In less pure BCC metals, the situation differs. Moderate increase of temperature, low cyclic strain rates and substitutional and interstitials atoms (C and N in α-iron) make the dislocation modes of BCC metals more similar to those of FCC metals. Then, PSBs may be observed, usually not with the classical wall/ladder structure in narrow bands containing, for example, a dislocation cell structure, while the matrix structure becomes quite similar to the "vein"

structure in FCC metals (Mughrabi, 2009). In only one study (Pohl et al., 1980), PSBs with the ladder structure have been found in a fatigued low-carbon steel.

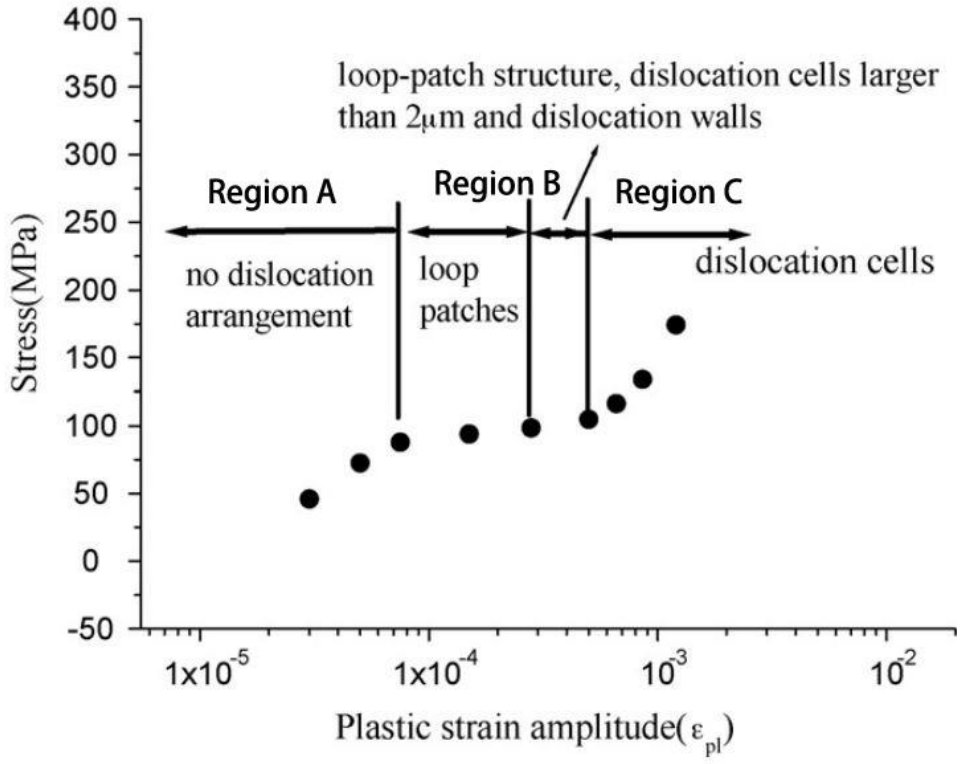

Figure 1.20 Relationship between dislocation structures and the cyclic stress-strain curve for polycrystalline iron. (Shih et al., 2009)

Also, in addition, in the presence of DSA, the motion of the edge dislocations is retarded preferentially by the carbon and/or nitrogen atoms, so that the dislocation velocities become more comparable as in FCC metals (Mughrabi, 2009).

The dislocation structures are less studied for BCC than for FCC metals, because the difficulties in Transmission Electron Microscope (TEM) studies dues to the ferromagnetism of BCC metals. Hempel (1957; Cazaud et al., 1968) showed the occurrence of slip markings (SMs) in Armco iron on the surface of flat specimens fatigued in bending. The higher the stress amplitude, the greater the number of SMs. As expected, the lower the stress amplitude, the later the occurrence. For $N_f = 5.6\times10^5$, SMs occured as early as 2.4×10^3 cycles (that is to say at 0.4% of the total life), and for $N_f = 2.2\times10^6$ at 1.12×10^4 cycles (0.51% of the total life). Klesnil and Lukáš (1965) have studied the dislocation structure just beneath the surface in the bulk of Armco iron specimens fatigued in tension/compression at 83 Hz at two stress amplitudes (22 kp/mm^2, $N_f = 10^6$ cycles; 24.5 kp/mm^2, $N_f = 5\times10^4$ cycles). Their results

confirm the early occurrence of SMs. The SM width is 1 to 2 µm. After removing a thin layer (2 µm by electrolytic polishing, and etching), these SM remained visible with small stains, and the authors referred to this as a "bamboo structure". After removing a layer of 6-7 µm, the SMs are no longer visible.

More recently, Munier et al. (2017) have studied the self-heating of High Strength Low Alloyed steels (HSLA) in tensile-compression with a frequency of 30 Hz in HCF until 10^6 cycles. In HCF domain, they observed PSBs similarly to those on polycrystalline copper by Lukáš and Klesnil (1973). These PSBs are homogeneously located on the surface, with different crystallographic orientations. For a given stress amplitude, when the number of cycles increases, there is no occurrence of new PSBs, as in Figure 1.21. The higher stress amplitude is, the denser PSBs on the specimen surface are.

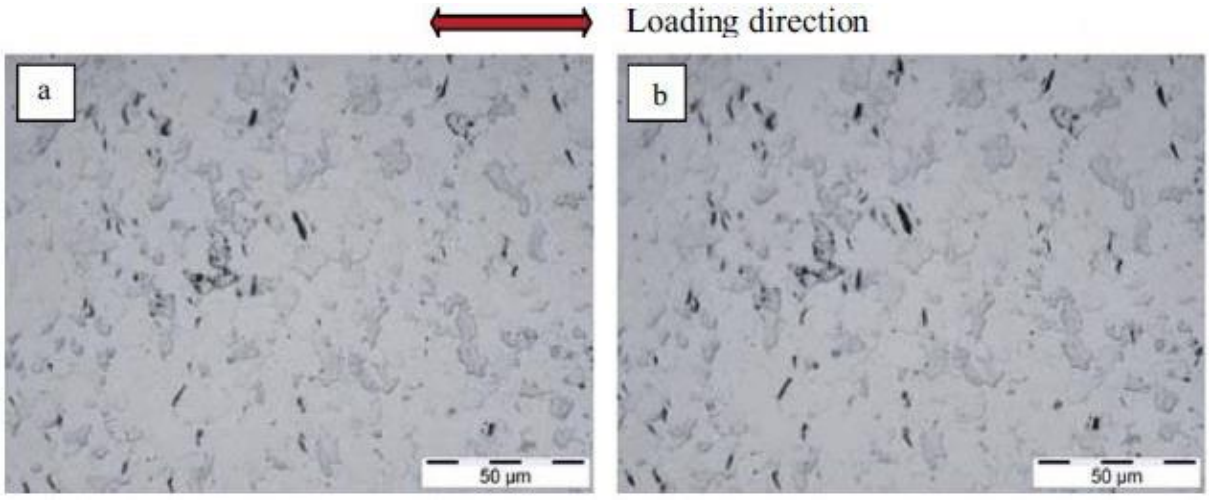

Figure 1.21 Appearance of PSBs in the interest zone of the specimen at different numbers of cycles for a stress amplitude of 250 MPa. At (a) 5×10^5 cycles; (b) 1×10^6 cycles.(Munier et al., 2017)

Moreover, Munier et al. (2017) also observed three different morphologies of PSBs observed on the surface of the specimens loaded at a stress amplitude of 250 MPa during 2 million cycles in this HLSA steel, as shown in Figure 1.22a-c. The first corresponds to straight PSBs (Figure 1.22a). This type of PSBs initiates at a grain boundary, propagates through the grain and joins a second grain boundary. The width and the length of the PSBs measure 1 and 10 µm respectively. Moreover, the surrounding grains do not present any signs of microplasticity. The second type of PSBs has a more peculiar and more complex morphology (Figure 1.22b). Indeed, this second type of PSBs presents a "comma shape". To the knowledge of the authors, such observations were reported only very rarely in the literature and concern mono or

polycrystals of fcc metals (Stanzl-Tschegg et al., 2007). The third type is the presence of a few grains covered with PSBs (Figure 1.22c).

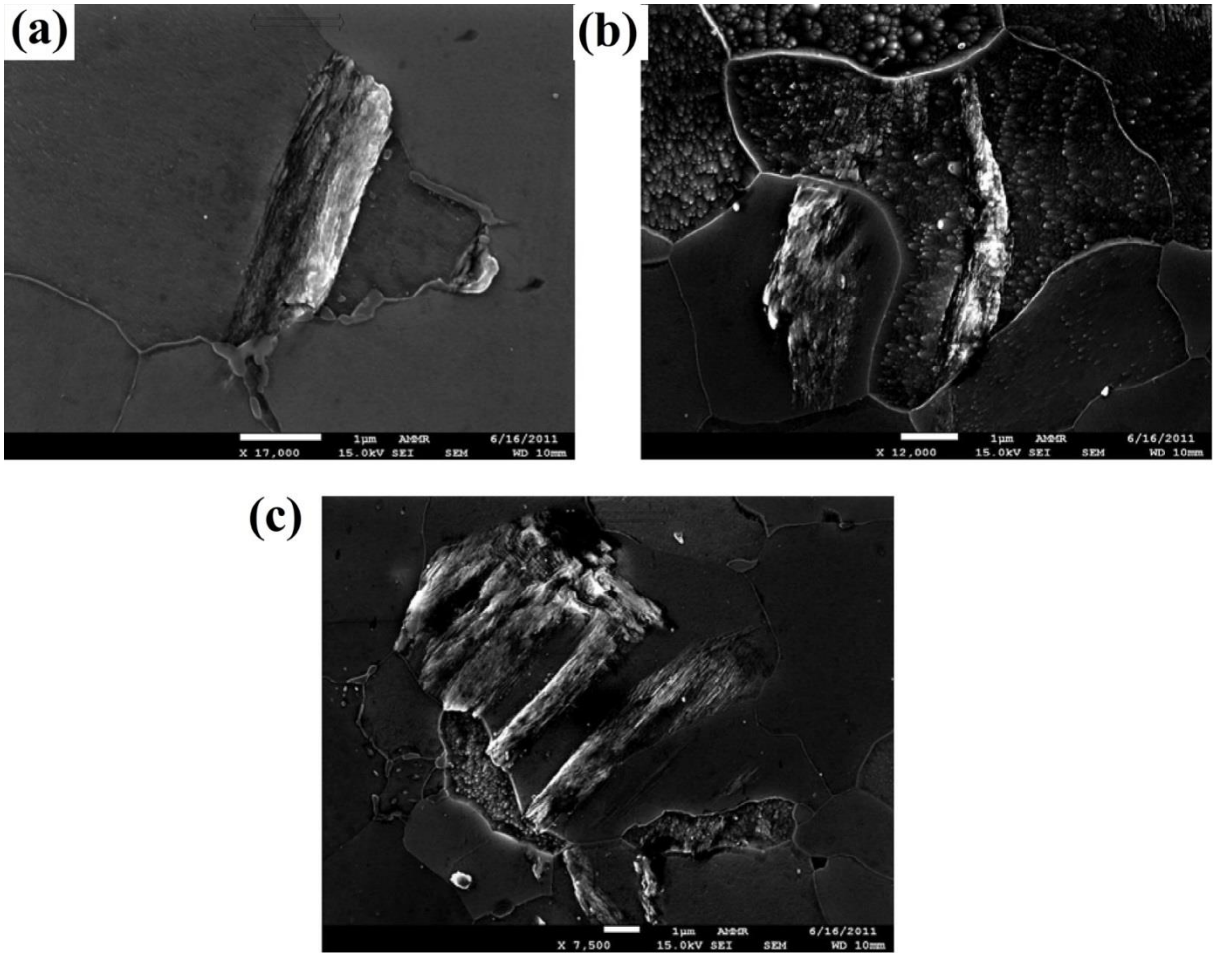

Figure 1.22 Three types of PSBs on surface of HSLA steel at 250 MPa during 2×10^6 cycles. (a) straight PSBs, (b) ‘‘comma shaped” PSBs, (c) example of a grain covered with PSBs. (Munier et al., 2017)

Low stress amplitudes (VHCF)

For the S-N curve, after 10^6-10^7 cycles at fracture, it is currently admitted that there is no asymptote corresponding to a fatigue limit. The curve decreases more or less among the materials (Bathias, 1999; Pyttel et al., 2011). In VHCF, only few PSBs are visible on the surface specimen (Wagner et al., 2016).

A new concept developed by Mughrabi (2009) is the cyclic slip irreversibility factor. The to-and-fro dislocation displacements lead to a cyclic slip irreversibility measured by a factor denoted *p*

and depending on the material. The cyclic slip irreversibility p is defined as the fraction of microstructurally irreversible cyclic plastic strain in the total plastic strain ($0 < p < 1$). When $p = 1$, the dislocation slip is totally irreversible (in LCF), whereas $p = 0$ refers to a completely reversible slip. In the VHCF regime, the factor p needs to be further investigated.

1.2.2 Fatigue crack initiation

The observations about the initiation of fatigue cracks using optical microscope have been widely studied in the last century (Ewing and Humfrey, 1903; Thompson and Wadsworth, 1958; Laird and Duquette, 1972), and significant efforts have been devoted to this field.

- At high loading amplitudes (LCF), many crack initiation sites can be usually detected at the surface, originating from Persistent Slip Bands (PSBs).
- At lower loading amplitudes (HCF), similar crack initiation sites can be detected at the surface but they are fewer in number than LCF conditions.
- At very low loading amplitudes (VHCF), two basic types of fatigue crack initiation in materials cyclically strained at ambient temperatures have been recognized:

  Type I, homogeneous materials, which contain only natural elementary defects like point defects, dislocations, stacking faults, twins and grain boundaries. Fatigue crack initiation always occurs at the surface.

  Type II, heterogeneous materials, like high-strength steels containing non-metallic inclusions. Fatigue crack initiates in the subsurface on second phase particles (e.g. inclusions) or from pre-exsiting defects.

➢ Surface crack initiation

In the LCF and HCF regimes, the fatigue damage is mainly related to the free surface (Forsyth, 1951, 1953). On the polished surface of the specimens, we can observe strips due to the formation of localized deformation bands, known as Persistent Slip Bands. These bands are formed on the sliding planes with a maximum resolved shear stress. These slip bands in polycrystalline specimens, which will lead to the formation of micro-cracks, appear at a 45 degree angle to the tensile axis. Only a few grains are involved in the formation of these bands. Orientation of the persistent bands and of the micro-cracks is significant, not only in

uniaxial loading but also in multi-axial loading. Researches (Brown and Miller, 1973; Miller, 1991) have found that the facet whose slip direction goes into the materials, are usually more dangerous than the facet whose slips direction is tangent to the free surface of the specimen.

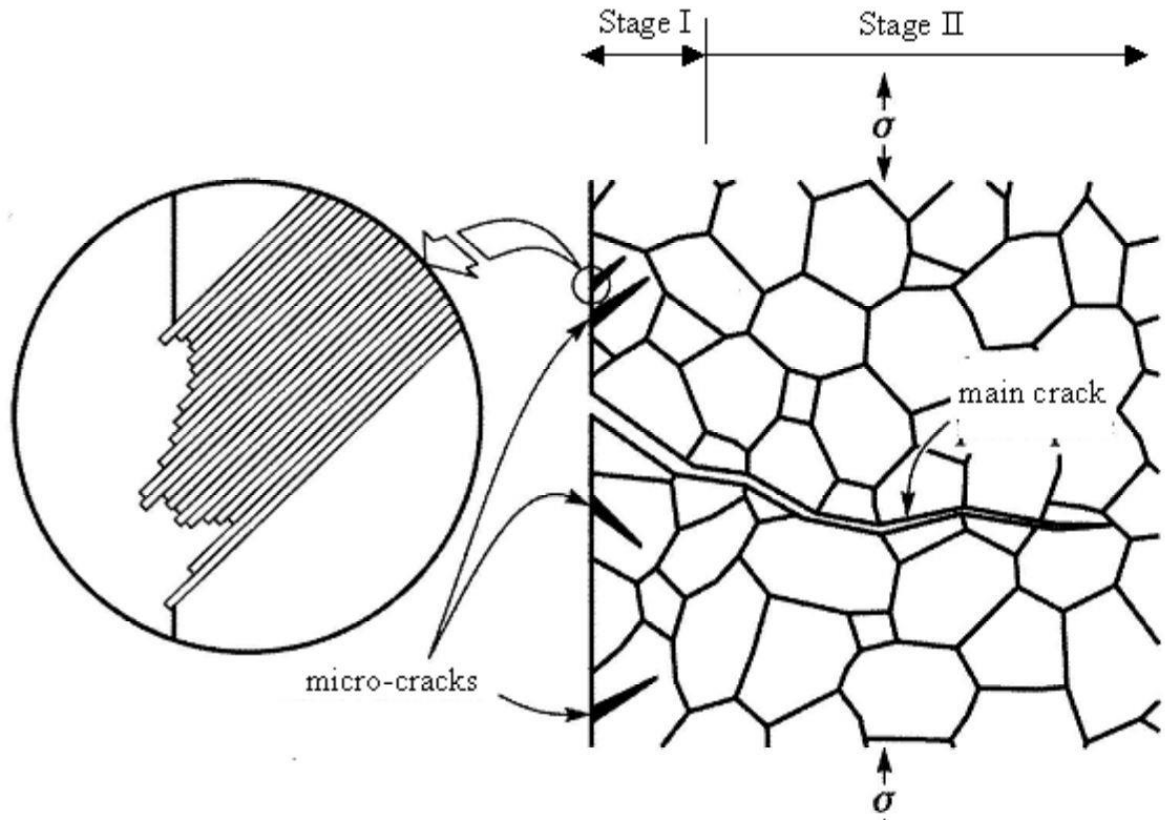

Figure 1.23 (left) Initiation of micro-cracks due to the sliding of alternate plans and to the formation of intrusion and extrusions at the free surface; (right) formation of a main crack from micro-cracks. (Bathias and Pineau, 2013)

As illustrated in Figure 1.23, fatigue crack initiation includes micro-crack formation in one certain grains (stage I in Figure 1.23) and main crack formed from micro-crack (stage II in Figure 1.23). The slips bands, which lead to the formation of stage I micro-cracks, appear at a 45 degree angle to the tensile axis. These bands lead to the formation of intrusions and extrusions at the free surface of the specimen.

Pronounced surface relief in the form of persistent slips markings is developed in cyclic straining at locations where the PSBs emerge on the surface. In some cases only extrusions are developed and intrusions are produced later in fatigue life. In polycrystalline copper, the extrusions and intrusions appear on the surface of the grain where PSBs are characterized by a ladder-like dislocation structure protruding on the surface. The crack-like intrusion shapes produce high stress and strain concentration and primary stage I crack starts growing from the

tip of intrusions. Similar features were observed in fatigued austenitic steel Sanicro 25 (0.1% carbon) by Polák et al. (2017). In Figure 1.24, in Sanicro 25 steel, at 962 cycles, it produces extrusions and intrusions with the same length of protrusion and insertion. At 1406 cycles, one micro-crack has been formed from the intrusion deeply into the bulk.

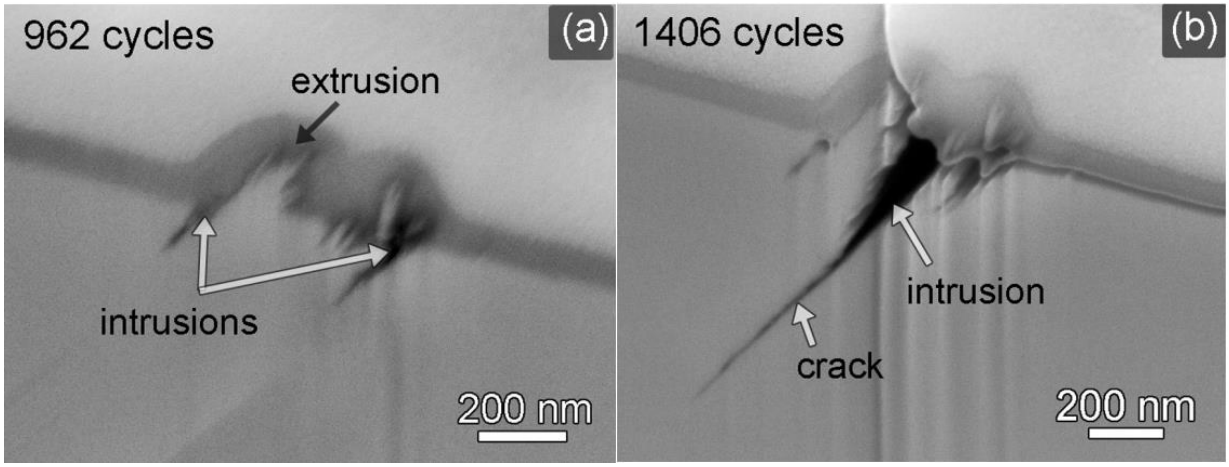

Figure 1.24 Evolution of persistent slip marks profiles during cycling of Sanicro 25 steel with constant strain amplitude 3.5×10^{-3}; (a) N = 962 cycles; (b) N = 1406 cycles. (Polák et al., 2017)

Forsyth (1963) explains why fatigue cracks always initiate from the free surface:

- Dislocations are easier to glide on free surface than in the bulk. Free surfaces have higher surface energy, there is always a driving force to create the low energy stable state.
- Free surface is the priority position to dislocation nucleation.
- Free surface are more susceptible to external environment.

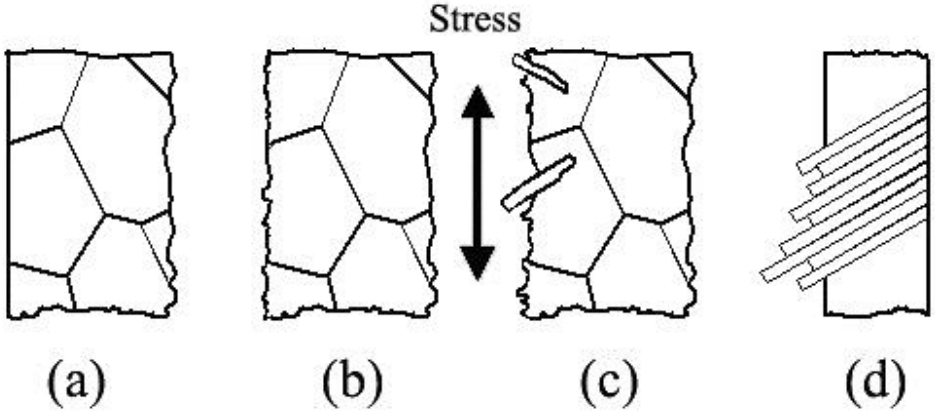

Figure 1.25 Schematic illustration of (a) Initial state, (b) early stage of surface roughening, (c) PSB formation at later stage, and (d) Persistent slip bands. (Mughrabi, 2006; Weidner et al., 2010)

In the VHCF domain (Mughrabi, 2006), regarding the mechanism of fatigue crack initiation, it is now proposed that when a critical state of surface roughness is reached, some valleys in the surface roughness profile act as sufficiently strong stress raisers to the extent that the local stress at such a site can exceed the PSB threshold value. This would then lead to the formation of an ‘‘embryonic’’ PSB, as indicated in Figure 1.25a-c. Such a PSB will only extend to a modest depth into the material. However, as the cyclic strain becomes localized in such PSBs, the notch-peak surface profile at the PSB sites is expected to become more accentuated with increasing numbers of cycles so that the PSBs will extend deeper into the material and that, finally, stage I micro-cracks will be initiated. If these cracks can propagate and grow subsequently, fatigue failure will occur ultimately, although the applied loading amplitude lies below the PSB threshold.

- Subsurface crack initiation

Most of the subsurface crack initiation starts from an inclusion, as shown in Figure 1.26a. For the subsurface crack initiation, it forms a fish-eye that contains a crack initiation region named Fine-Granular-Area (FGA) whose origin is not understandable at this time.(Wang et al., 2019) The fracture surface of FGA is relatively rough, and the fish-eye region outside FGA is relatively flat. Beyond fish-eye the fracture surface is of large roughness, which is the final crack. Figure 1.26b shows typical fractographies of the characteristic region for VHCF of high-strength steels (Hong et al., 2014).

Crack initiation depends on the quantity, size, nature and inclusion distributions (Lei et al., 2012), as well as on their shape regarding load direction. Generally, the material with smaller inclusions has higher fatigue strength and a longer fatigue life. When the inclusion size is smaller than the critical size, the fatigue failure originates from the inclusion clusters or surface matrix at PSBs or grain boundary (Zhang et al., 2007). In addition, cohesion of the matrix-inclusion interface plays a key role (Spriestersbach et al., 2014).

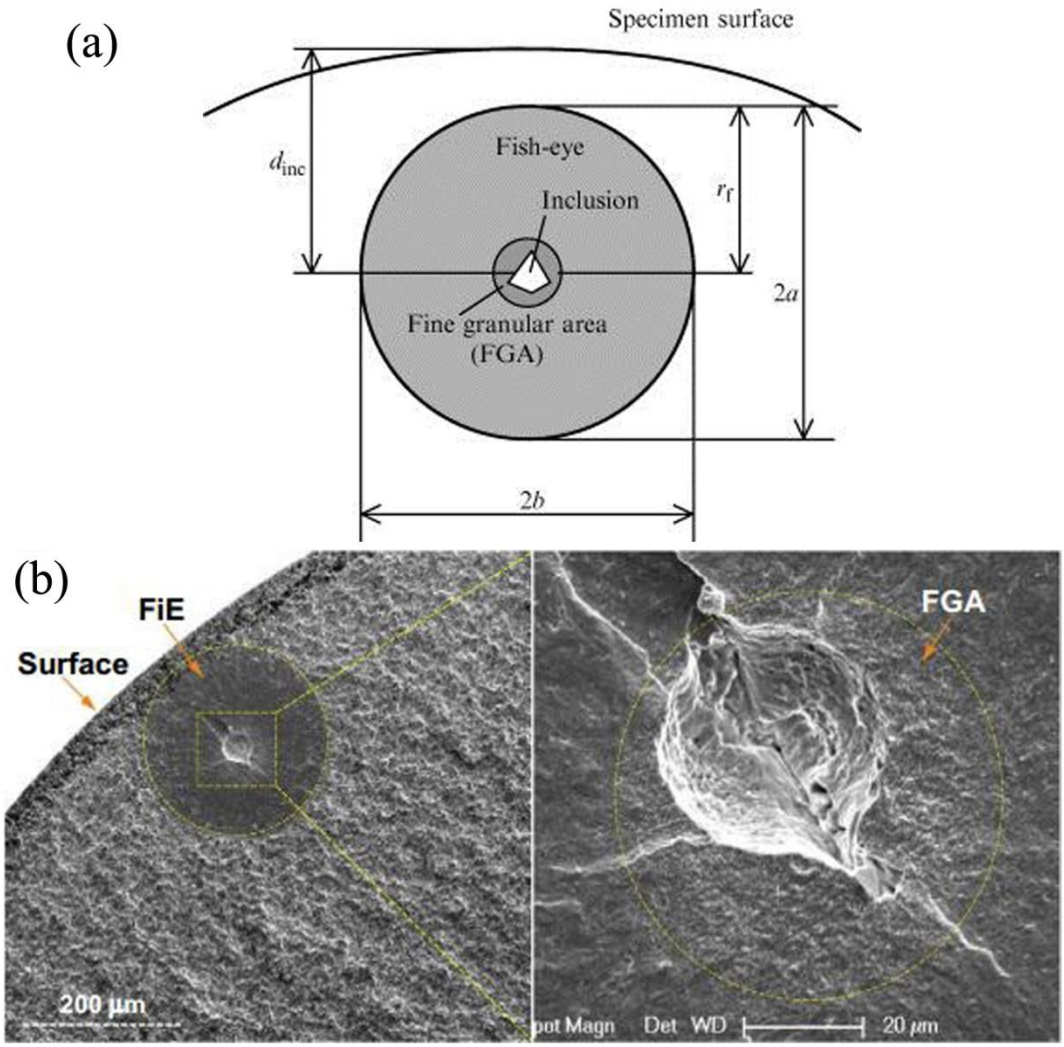

Figure 1.26 (a) Schematic figure for inclusion-induced fracture surface. (Sakai et al., 2002) (b) Typical morphology of characteristic region of crack interior initiation for a high-strength steel (1% C, 1% Cr) subjected to rotary bending with $N_f = 1.79\times10^7$ cycles. (Hong and Sun, 2017; Hong et al., 2014)

1.2.3 Fatigue initiation life

To evaluate the crack initiation stage, N_i has been defined by different authors as the number of cycles to crack initiation creating a crack length about 10 ~ 100 μm, at the order of grain size of many metallic materials (Bathias and Pineau, 2013). Actually, the transition from initiation to propagation is defined as being the point at which the linear elastic fracture mechanics (LEFM) and the Paris law are applicable.

In LCF and HCF, fatigue crack initiation stage is of very importance, which can be affected by many parameters, such as the applied stress amplitude, the specimen geometry, material properties, temperature, previous loading and environment.

In VHCF, the fatigue crack initiation accounts for the vast majority of the total fatigue life (Mughrabi, 1999, 2002; Zuo et al., 2008). For instance, Wagner et al. (2016) showed that for a BCC polycrystal Armco iron loaded up to the VHCF domain, crack initiation takes up ~90% of the fatigue life. Therefore, in the VHCF regime crack initiation is life-determining.

1.3 Thermographic experiments in HCF and VHCF

1.3.1 Fatigue properties estimation

For a better understanding of crack initiation in VHCF regime, thermography method is introduced to observe the temperature change and microscopic changes of BCC steels in VHCF domain. Infrared thermography is very popular as a non-destructive, real-time, and non-contact technique to detect the physical processes of damage, fatigue and failure on metallic specimens subjected to low and high cycle loadings. In the 1970s, Reifsnider and Williams (1974) and Charles et al. (1975) showed an attempt to use an infrared camera to measure the surface temperature during the tests and to predict the location of the impending fatigue cracks and map temperature field. Botny and Kaleta (1986) presented the temperature profile with three characteristic stages: initial temperature increase, temperature stabilization and final rapid increase.

It is obvious that the specimen temperature increase is dependent on the stress amplitude. Especially, when the stress is below the fatigue limit at 10^7 cycles, the temperature increase on specimen surface at 100 Hz loading is very low (below 1 ℃), but still superior to the experimental noise (Luong, 1998). Hence, Luong (1995, 1998) presented a two-curves method to interpolate the experimental data, one for the stress below the fatigue limit and the other for above the fatigue limit. Then, the corresponding intersection point was indicated as the fatigue limit, as illustrated in Figure 1.27a.

In these publications, the fatigue limit corresponds to the inflexion point of the S-N curve, comprised around 10^7 cycles. Also, this fatigue limit is the transition between HCF and VHCF regime, but doesn't represent the intrinsic fatigue limit. This method enables to observe the physical damage process, measure the intrinsic dissipation and rapidly evaluate the fatigue strength of the tested metals at around 10^7 cycles. These results were further developed and extended by Amiri and Khonsari (2010), Cura et al. (2005). Amiri and Khonsari (2010) utilized an empirical equation to deduce the number of cycles to failure as a

function of the initial rate of temperature rise. The similar method has also been applied in tension-compression loading. La Rosa and Risitano (2000) proposed "one-curve method" to rapidly estimate the fatigue limit of carbon steel (C30, C70 steels) by using the stabilization temperature under a low frequency tensile-compressive loading (10 Hz). The fatigue limit is determined by plotting the stabilization temperature against the applied stress and finding the intercept of the curve on the stress axis, as illustrated in Figure 1.27b.

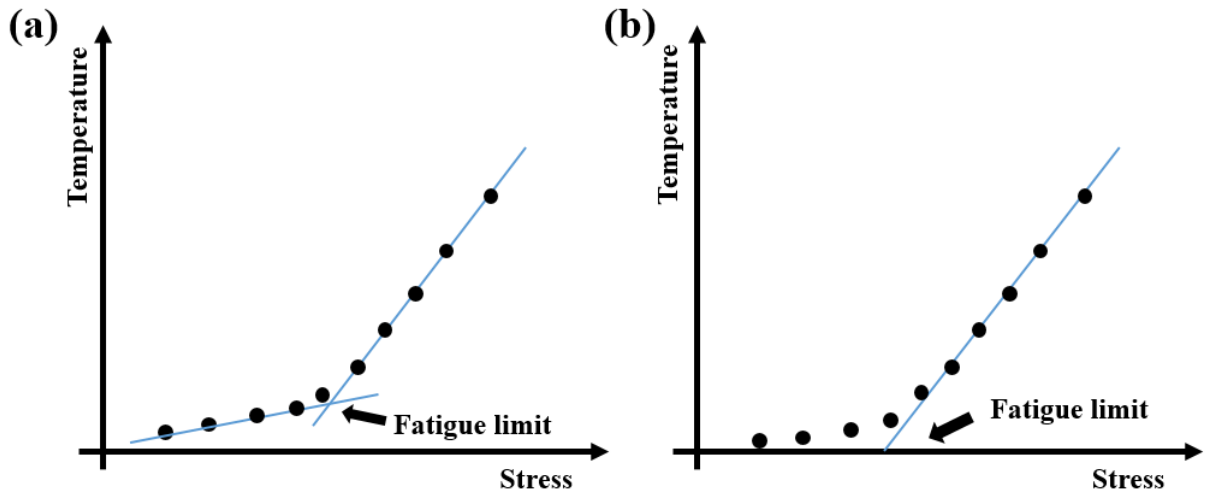

Figure 1.27 Graphical determination of the fatigue limit by using (a) Luong's two-curve method (Luong, 1995), (b) one-curve method (La Rosa and Risitano, 2000).

Munier et al. (2014) expanded this thought and performed the self-heating curves of sixteen steel grades. By using a two-scale probabilistic model, authors showed that the observed two dissipative phenomena correspond to two dissipative mechanisms in low frequency cyclic loading in the HCF regime. In most cases of LCF or HCF regimes, specimen temperature is lower than dozens of degrees (Luong, 1995; La Rosa and Risitano, 2000; Munier et al., 2014; Guo and Guo, 2016).

In order to study the mechanisms at the origin of the two self-heating regimes under cyclic loading observed for stress amplitudes lower and higher than the conventional yield stress. Microscopic observations have been carried out on the surface of several specimens after cyclic loading. All the results presented in Figure 1.28 have been obtained on an HSLA (i.e., High Strength Low Alloy) commercial steel. According to Luong's one curve method, the conventional fatigue limit stays around 230 MPa. Below this fatigue limit, optical microscopic and EBSD observations showed only a few rare PSBs as well as the appearance of intragranular misorientation in the majority of grains. Above this fatigue limit, many PSBs

in a random way could be observed on specimen surface. These observations provided rich information of main dissipative source in both self-heating regimes under cyclic loading.

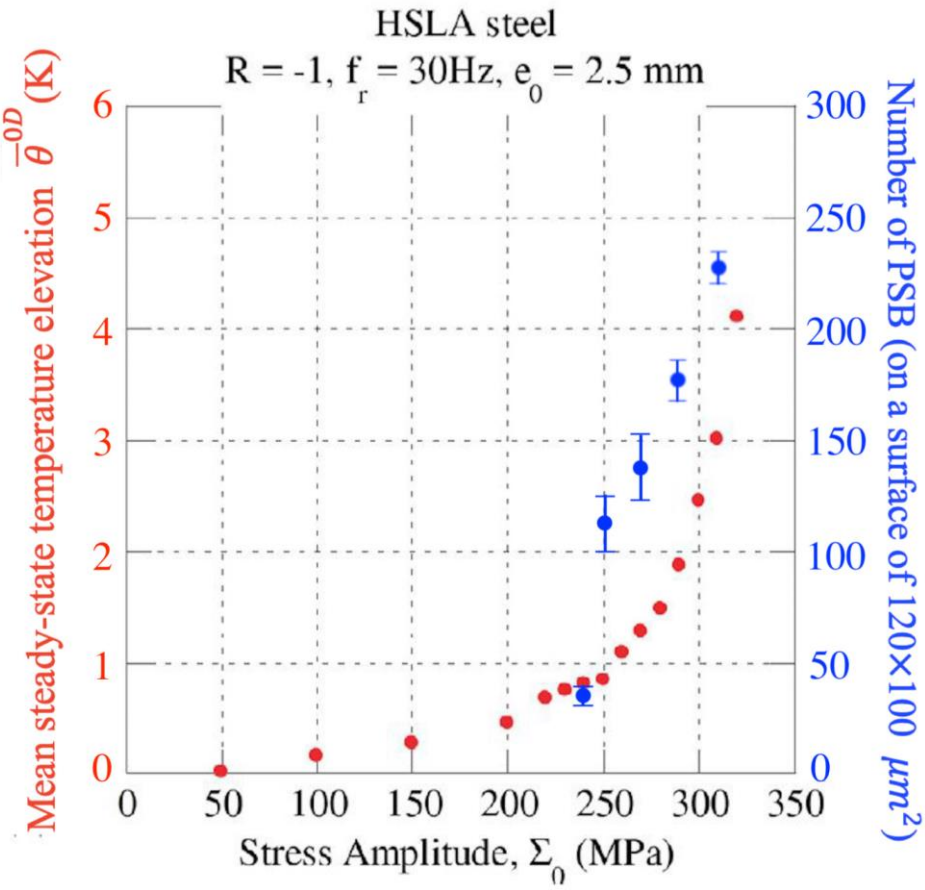

Figure 1.28 Evolution of specimen temperature and number of PSBs versus the loading amplitude. (Munier et al., 2017)

Nevertheless, the temperature field on the specimen surface during the fatigue tests can improve the understanding of damage evolution before the crack initiation at very low stress and strain amplitudes (Wagner et al., 2010).

In one word, results about the determination of fatigue limit between HCF and VHCF regime via thermographic method brought a clear and incisive analysis to evaluate the fatigue life at around 10^6 cycles. These results focus on HCF regime. Owing to the latest development of high frequency ultrasonic machine, researches on high-frequency (20 kHz, 30 kHz) cyclic loading in VHCF domain are not very abundant yet. In recent years, VHCF regime begins to draw more attention due to necessary component design up to 10^9-10^{11} cycles. Indeed, the fatigue tests performed after 10^6 cycles show a decrease of the fatigue limit with increasing number of cycles (Bathias, 1999). Furthermore, the strain rate sensitivity of materials can

make their fatigue and thermal behaviors in VHCF regime different from the LCF or HCF regimes (Mareau, 2009; Munier et al., 2014).

Another aspect is that some materials present a remarkable temperature increase under ultrasonic fatigue loading, comparing with that in LCF or HCF regimes, while the test is still running. In the VHCF range, the French ANR project DISFAT has given self-heating results on FCC and BCC materials (Favier et al., 2016). For the strain rate-sensitive BCC metals, their self-heating response is more important than for FCC metals. The dual phase steels with ferrite-pearlite or ferrite-martensite microstructure show an abnormal behavior at the higher stress amplitudes: a sudden, rapid and inevitable increase of the surface temperature which doesn't correspond to the specimen fracture, and metals could continue surviving for some cycles.

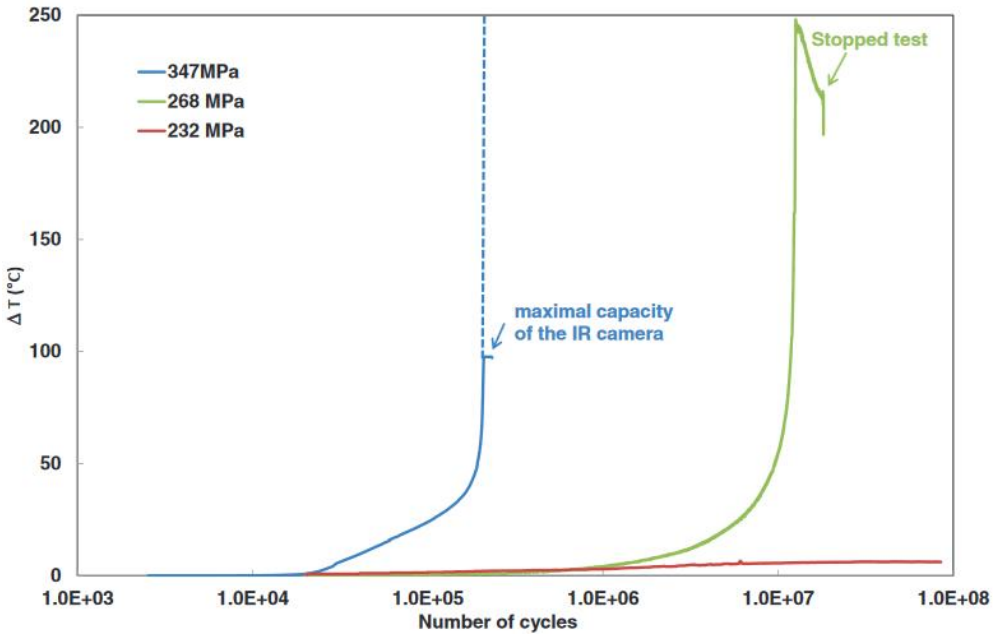

Figure 1.29 Increase of temperature of C45 steel under ultrasonic fatigue as a function of number of cycles for stress amplitudes of 232 MPa, 268 MPa and 347 MPa. (Ranc et al., 2015)

Huang et al. (2016) has firstly shown this phenomenon on C-Mn ferrite-pearlitic steels, A42 and A48. Up to a certain stress level, the specimen temperature would increase above 300 °C in one second. Ranc et al. (2015) found that C45 steel under 20 kHz ultrasonic cyclic loading has the same phenomenon, specimen temperature could reach few hundreds of degrees (in Figure 1.29), dependent on the applied stress amplitude: Below 200 MPa, the heating was less than 10 ℃ and no fracture was observed up to 10^{10} cycles. In the range of 200 MPa to 250 MPa, the heating reached few hundreds of degrees. Fatigue fracture took place. The crack

initiated at an internal non-metallic inclusion leading to the classical fish eye observed in VHCF. Above 250 MPa, the heating reached 800 ℃ and a ductile failure occurred. Torabian et al. (2016) and recently by Ouarabi (2018), have also shown this phenomenon on dual phase ferrite-martensitic steels. For DP600 ferrite-martensite steel in Figure 1.30, the specimen temperature could increase from the stabilized temperature to about 350 °C above 251 MPa.

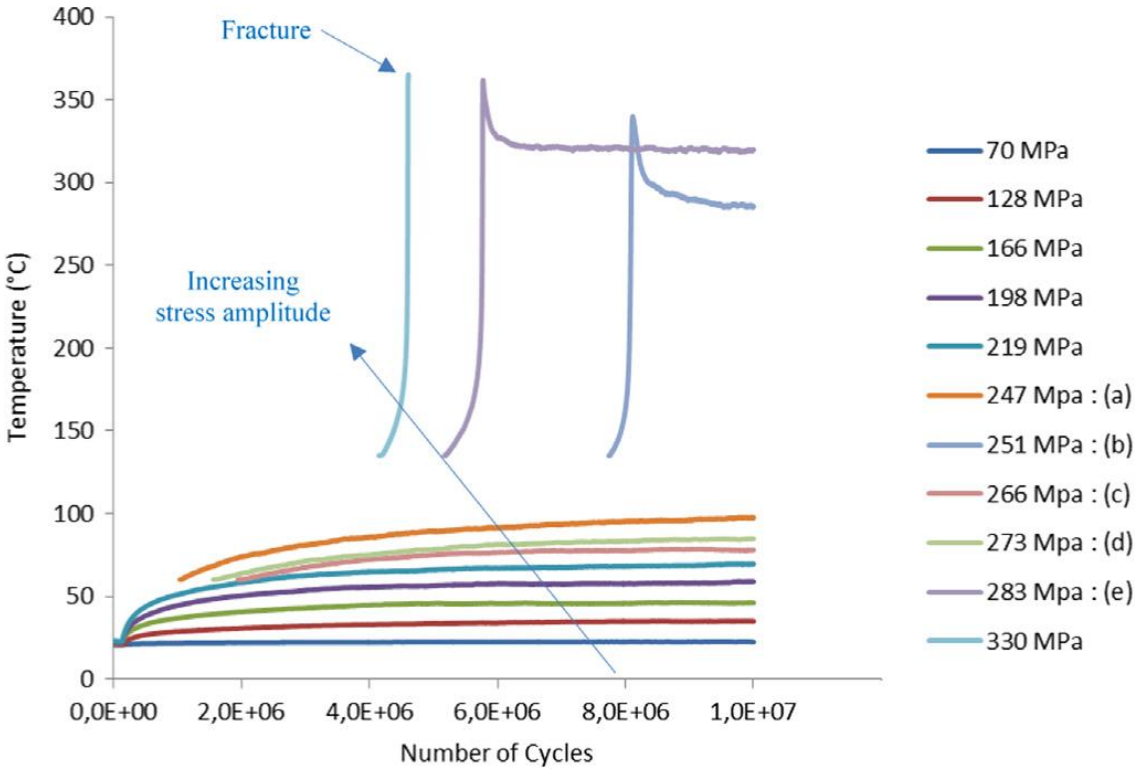

Figure 1.30 Temperature evolution versus number of cycles for different stress amplitudes for dual phase ferrite-martensite steel DP600. (Torabian et al., 2016)

1.3.2 Crack detection

In previous part, under high frequency loading, ferritic steels were reported to own the special phenomenon of sudden temperature increase to hundreds of degrees. Besides, the material rupture or crack formation is also sure to cause sudden temperature increase up to hundred of degrees.

In Figure 1.31, when DP600 steel is loaded at 330 MPa, the inhomogeneous temperature field caused by crack formation was detected by infrared camera. The temperature field around crack tip is higher than other positions.

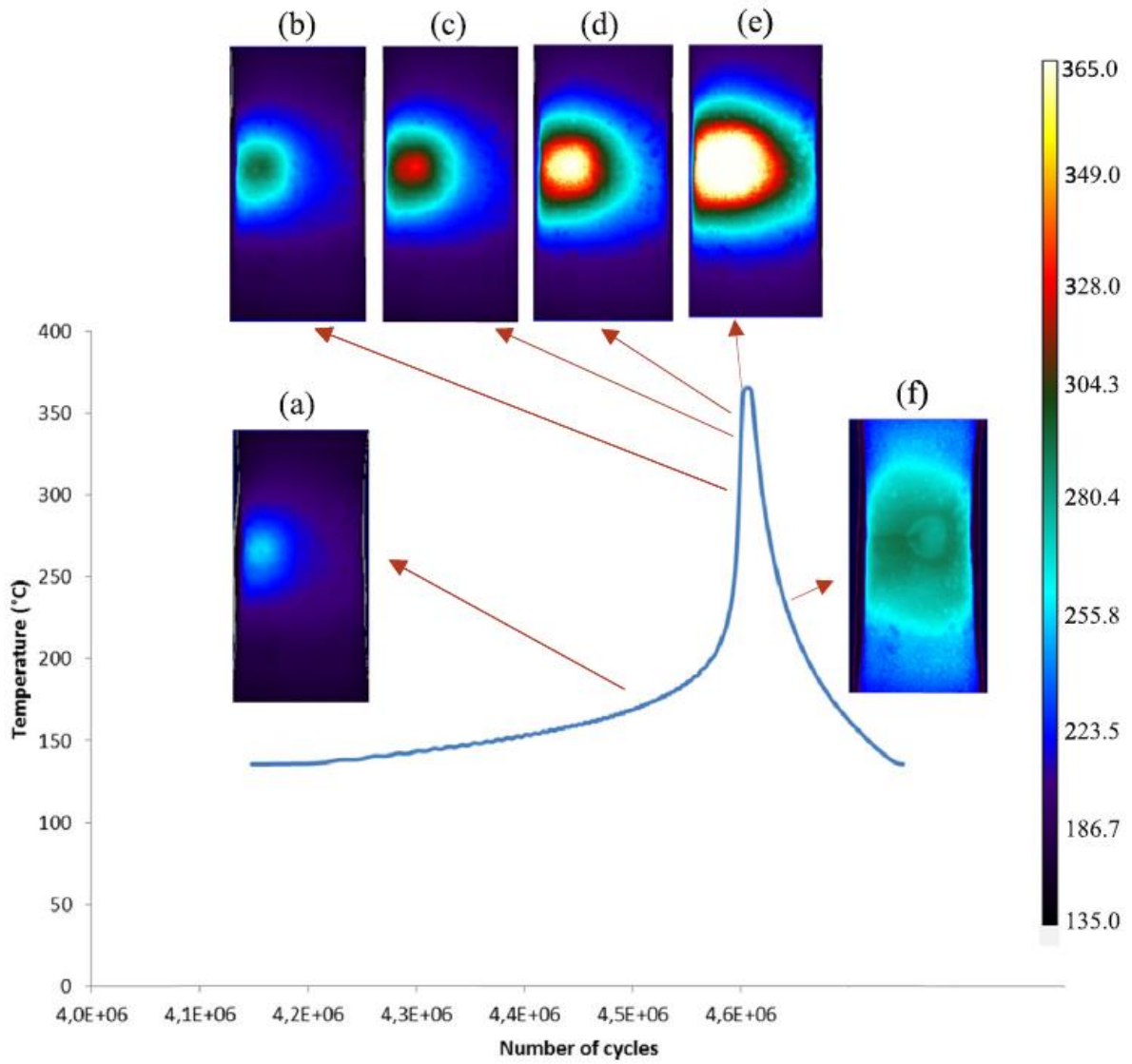

Figure 1.31 Temperature field of DP600 steel at 330 MPa.(Torabian et al., 2016)

Figure 1.32 shows the infrared information of low carbon martensitic steel AISI 5120 under 20kHz loading when the specimen temperature curve evolves near the sudden temperature increase. Owing to the thermal field recording on the specimen surface with an infrared camera, the transition between crack initiation and crack propagation stage is easily found, because the crack size at the transition and the heat sources produced at the short crack tip are sufficiently large and intense.

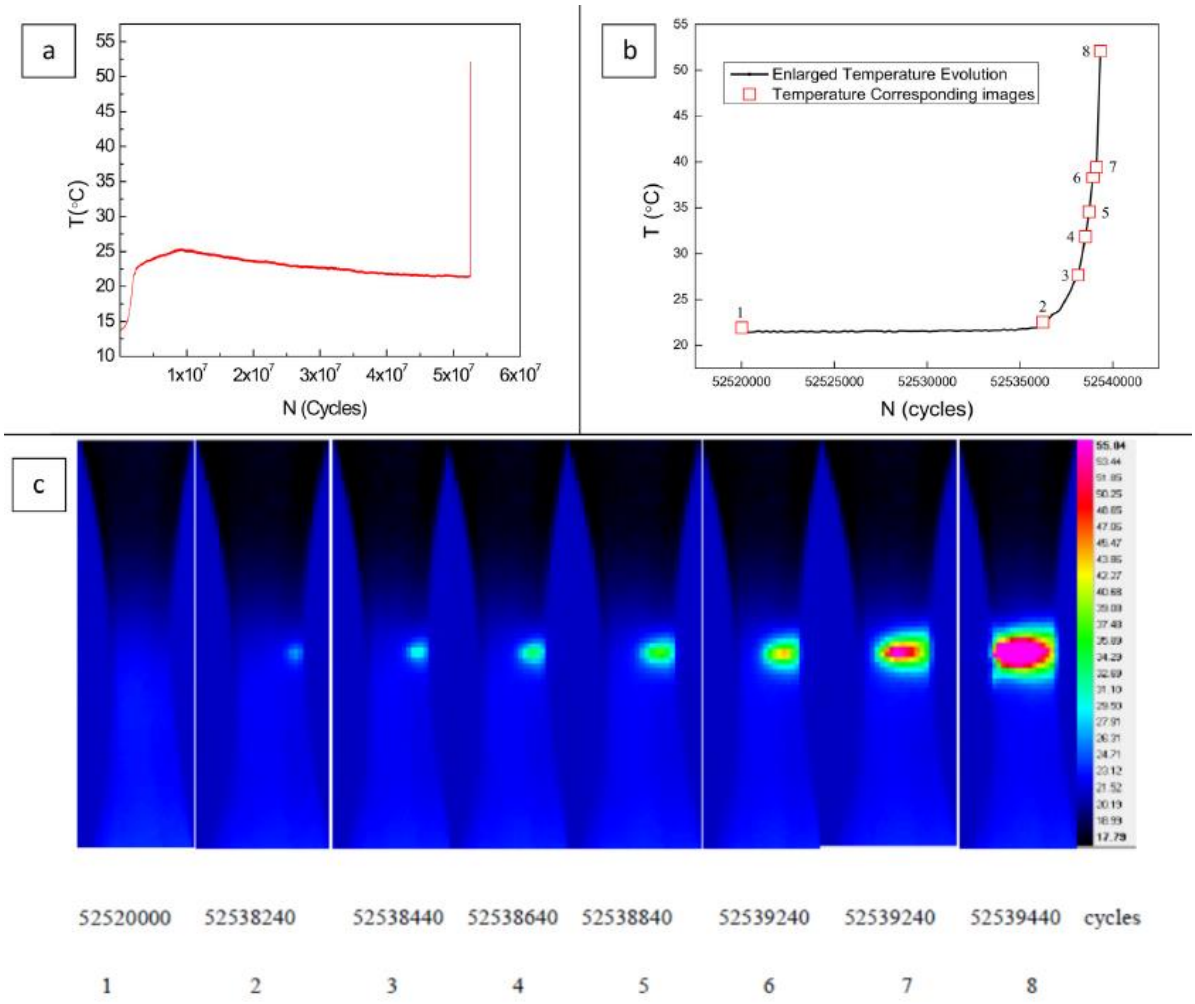

Figure 1.32 Thermal results for the low carbon martensitic steel AISI 5120 specimen (400 MPa, 5.25×10^7 cycles, R=0.1). (a) Evolution of the average temperature T in the center of the specimen as a function of the number of cycles N; (b) Enlarged part of (a) at the end of the test; (c) Thermal field recording on the specimen surface at the end of the test. (Wang et al., 2019)

To sum up, no matter the surface and subsurface crack initiation and propogation, they always accompany with the inhomogeneous temperature field in infrared recording, and the temperature of crack tip is much higher and intensive. As to the sudden temperature previously-mentioned in ferrous steels under high frequency loading, whether it's caused by crack formation needs to be investigated.

1.3.3 Application of heat dissipation

As explained above, temperature variation during fatigue tests can reflect to some extend material fatigue properties, like the traditional fatigue limit, and plastic deformation

mechanisms. However, it is not such a direct way to build the link between material mechanical behavior and its thermal performance in fatigue behavior. For this aim, alternative indicators of cyclic plasticity are heat sources, including intrinsic dissipation (pure mechanical heat source) and thermomechanical coupling heat sources. The relevant theories and equations will be introduced in Chapter 2. Guo Qiang (2016) succeeded to predict the traditional fatigue limit by intrinsic dissipation d_1 under a series of stress amplitudes, which achieved a similar result as that by temperature increment. But comparing with temperature increment, one advantage of heat sources is to benefit the comparison of thermal performance of same material studied at different time, or thermal performance of different materials.

Besides predicting the fatigue limit, heat source method can also help us investigate the heterogeneity of plasticity on specimen surface, and then indicate the onset of fatigue crack initiation (high intensity location of heat source). Wang Chong et al. (2014) drew the evolution of intrinsic dissipation of steel plate specimen during VHCF tests, as shown in Figure 1.33. High intensity of intrinsic dissipation emerged on one specimen location, which was same as the location of fatigue crack initiation on SEM observation, as in Figure 1.34. In the thesis, we will attempt to follow their work and use the heat source method to estimate the fatigue properties of different types of steels.

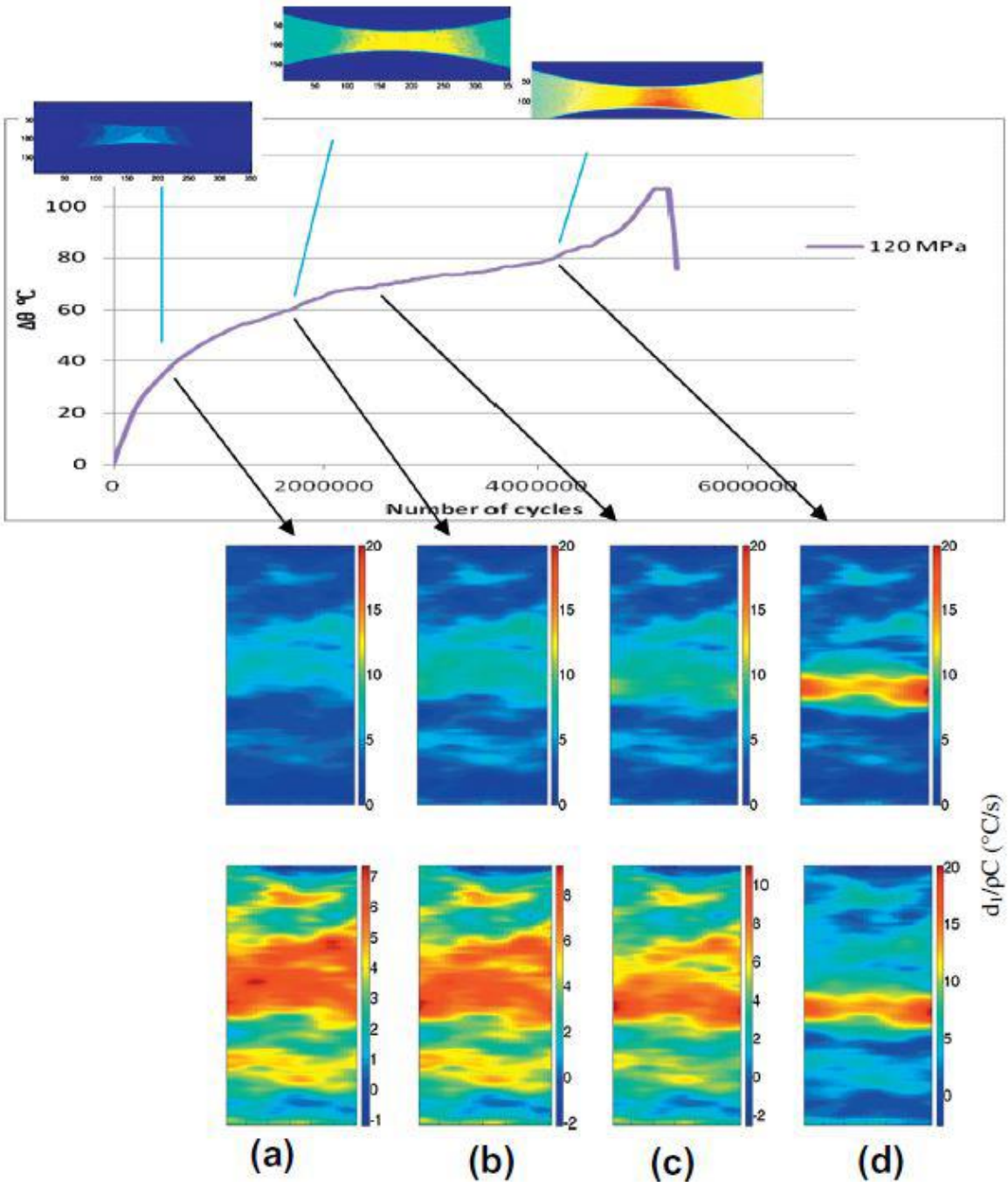

Figure 1.33 Infrared thermal images and intrinsic dissipation fields for different numbers of loading cycles. (Wang et al., 2014)

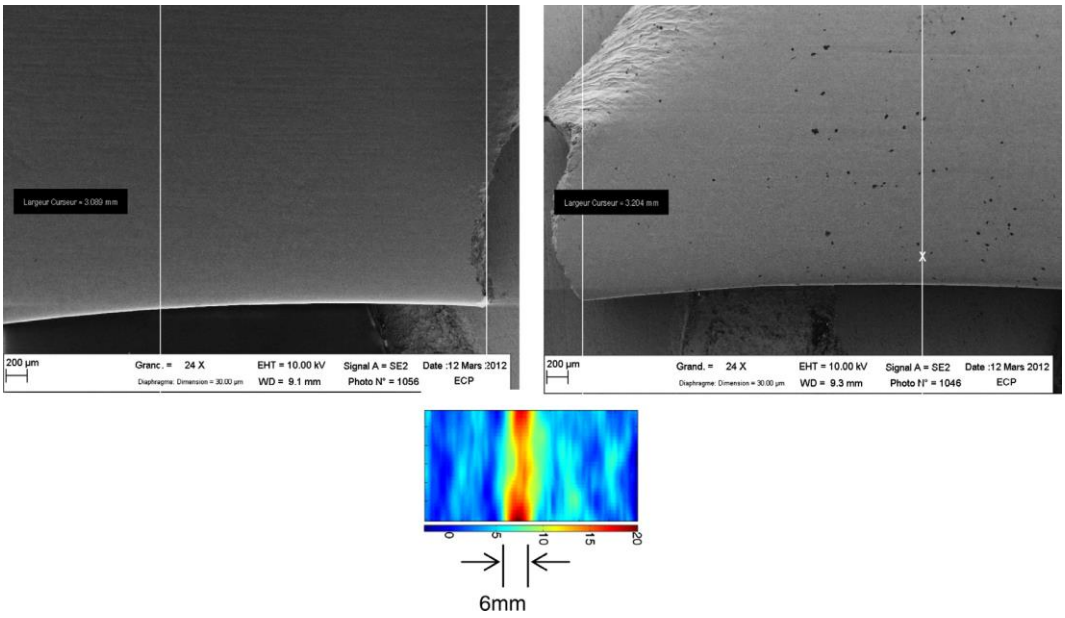

Figure 1.34 Correlation between intrinsic dissipation and PSB formation on armco iron specimen. (Wang et al., 2014)

1.4 Conclusions

This chapter mainly presents the general knowledge and research status about fatigue and the thermography method in C-Mn steels.

- Firstly, we begin to talk from the basic knowledge about crystal structure, thermal treatment of steels and hardening in steels. Therein, dynamic strain aging and temperature-dependent deformation mechanism in C-Mn steels are introduced. Herein, the important role of impurity atoms in C-Mn steels is addressed in this chapter.

- Secondly, fatigue damage mechanisms are summarized. Plastic deformation in crack initiation and formation of persistent slips bands in FCC and BCC metals are useful to understand the microstructure evolutions in chapter 3.

- Thirdly, the research status about self-heating tests is summarized, and mechanisms of the thermal response of ferrite steels under high frequency fatigue loading need to be further and eagerly investigated.

Chapter 2 Experimental devices and methods

With the development of technology, fatigue testing machine can make its loading frequency reach 20 kHz or higher. Various loading types (Arakere, 2016; Brugger et al., 2017; Jiang, 2018) have been developed in these decades. Therein, tension-compression mode is the most common and studied. In our work, the ultrasonic 20 kHz tension-compression testing system is used with the stress ratio R = -1.

For ultrasonic fatigue testing machine, the specimen must have the same natural frequency as the excitation frequency of fatigue machine. So the specimen geometry requires to be specially designed. Moreover, at the stress ratio R = -1, one end of the specimen needs to be fixed to the testing system, while the other end is free.

This chapter will talk about the 20 kHz fatigue system, the specimen design and their related simulation. Considering that the infrared camera and optical microscope are frequently applied in our work, brief introduction about specimen surface preparation and thermography analysis will be presented.

2.1 Experimental setups

2.1.1 Components and calibration of the ultrasonic machine

Fatigue tests are performed on a piezoelectric fatigue machine designed by C. Bathias et al. (2005). The vibratory fatigue system illustrated in Figure 2.1 is made of several elements:

– a Branson vibration generator that can reach a power of 2 kW and whose frequency is tuned between 19.5 kHz and 20.5 kHz. It gives a sinusoidal signal to the converter, which produces vibration;

Figure 2.1 Components of fatigue system: ①converter, ②amplifier, ③horn, ④generator, ⑤ laser sensor.

– a converter to turn electric vibrations into mechanical ones;

– an amplifier called “booster” to increase or decrease (1.5 times) the displacement of the converter;

– a horn made of a cylindrical part followed by a cone-shaped profile section. As the displacement amplitude of the converter + booster is limited, the cone allows to increase the vibratory amplitude of the specimen in order to reach the required stress. The specimen is fixed to the end of the horn using a screw;

- Calibration of the ultrasonic machine

In the controlling software of the ultrasonic fatigue machine, we need to give the specimen displacement amplitude. Then, the software converts this imposed displacement into a control voltage applied to the generator. Consequently, the software has to know the relation between the control voltage and displacement amplitude of the specimen. The determination of this relation stands as the calibration of the ultrasonic machine.

In our vibration system, there are three linear relations:

- a linear relation between the control voltage and the displacement amplitude of the piezoelectric ceramic in converter.

- a linear relation between displacement amplitude of the piezoelectric ceramic in converter and displacement amplitude of the horn.

- a linear relation between displacement amplitude of the specimen's free end and control voltage.

As a consequence, a linear relation exists between control voltage and displacement amplitude of the specimen's free end.

A laser sensor can be used to directly measure the vibratory amplitude at the end of specimen. In particular, the Keyence LK-H022 series available in the laboratory LEME has a maximum detection frequency of 392 kHz. During the calibration, 200 kHz is chosen to detect the 20 kHz vibration frequency of the fatigue system, so that in one sinusoidal wave, it can get 10 data points. The accuracy of the laser sensor is better than 0.1 μm. In Figure 2.2, for a given input voltage, a sinusoidal displacement is found at the free end of the specimen, and the corresponding displacement amplitude can be determined by discrete Fourier transform. The calibration curve can be drawn by measuring several points. Figure 2.3 shows an example of the calibration curve. This

one exhibits a good linear dependence between control voltage and displacement of the specimen.

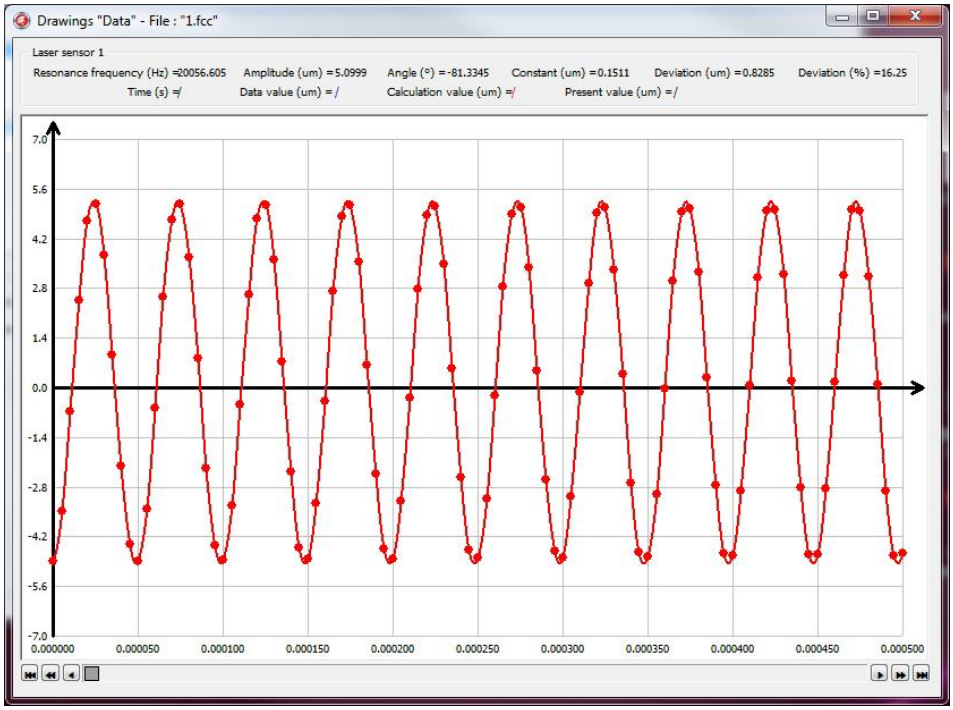

Figure 2.2 Wave obtained from laser sensor at the free end of specimen.

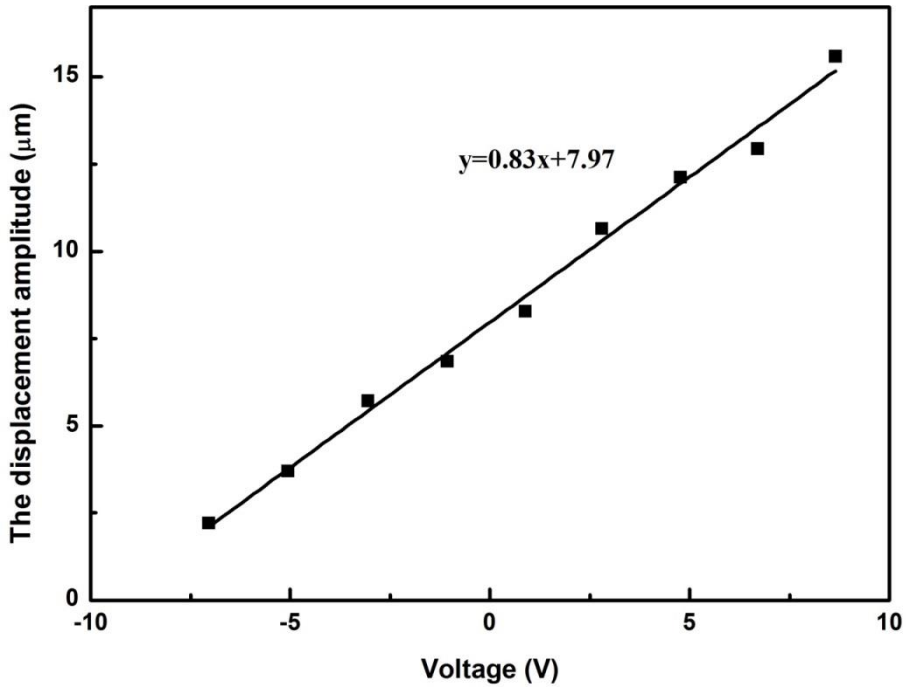

Figure 2.3 Variation of the specimen displacement versus generator input voltage during calibration of the fatigue machine.

2.1.2 Specimen design and numerical simulation

Working with an ultrasonic system requires that the specimen has the same natural resonance frequency as the piezoelectric ceramic, i.e. around 20 kHz ± 500 Hz in our case. In this work, due to the requirement of in-situ thermal and microstructural fields recording during testing, the geometry of the specimens under vibratory fatigue is purposefully designed with a flat profile (Figure 2.4).

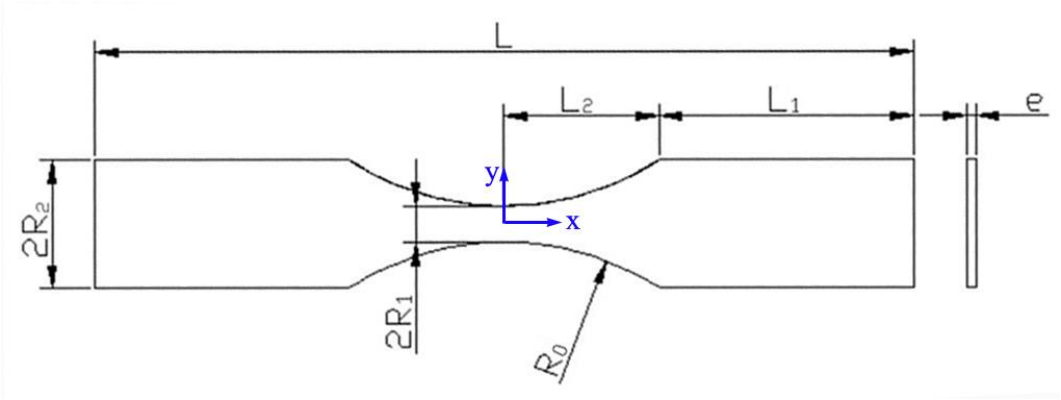

Figure 2.4 Profile of flat specimen used in ultrasonic fatigue tests.

For the flat specimen of Figure 2.4, the central part should have an hyperbolic cosine profile, i.e.,

$$y(x) = R_2, \quad L_2 < |x| < L/2 \tag{2.1}$$

$$y(x) = R_1 \cosh^2(\alpha x), \quad |x| < L_2 \tag{2.2}$$

with

$$\alpha_1 = \frac{1}{L_2} \operatorname{arccosh}\left(\sqrt{\frac{R_2}{R_1}}\right) \tag{2.3}$$

Then we can find the specimen's resonance length as follows.

$$L_1 = \frac{1}{k} \arctan\left\{\frac{1}{k}[\beta \coth(\beta L_2) - \alpha \tanh(\alpha L_2)]\right\} \tag{2.4}$$

with

$$\beta_1 = \sqrt{\alpha^2 - k^2} \tag{2.5}$$

$$k = \frac{\omega}{c} \tag{2.6}$$

where, $\omega=2\pi f$ is the angular velocity of loading pulse, $c=\sqrt{E/\rho}$ is the material parameter. R_1, R_2, and L_2 are arbitrarily chosen and we adopt the values reported by Wang (2013), and L_1 is determined so that the stress vanishes at the end of the specimen. In practice, for the sake of machining, the central part of the specimen is circular with a curvature radius R_0. R_0 is determined from the following geometrical relationship, based on Figure 2.4:

$$R_0 = \frac{L_2^2}{2(R_2-R_1)} + \frac{(R_2-R_1)}{2} \tag{2.7}$$

The dimensions of the ultrasonic specimen are presented in Table 2.1. Since a fatigue specimen owns variable sections, the corresponding amplitudes of strain and stress vary at each section. In order to obtain inherent frequency of specimen, it's necessary to use the numerical approach, such as the finite element method (FEM). Table 2.2 gives the relevant parameters used in our FEM calculations. Figure 2.5 is the screenshot of the displacement field of the specimen-horn group along the *x*-axis (direction of the system length) obtained under the first vibration mode in traction-compression and computed with the FEM software ANSYS (by modal analysis).

Table 2.1 Dimensions (in mm) of flat specimen in ultrasonic fatigue tests.

L_1	27.8
L_2	17
R_1	2
R_2	7
R_0	31.4
e	1

Table 2.2 Parameters used in FEM simulation.

Model		3D components (specimen-horn)		
Element	Type	SOLID 185		
	shape	Tetrahedron		
	Number	54191		
Material			Specimen (α-iron)	Horn (Titanium alloy)
		Young's modulus (GPa)	200	110
		Density (kg/m^3)	7800	4500
		Poisson's ratio	0.3	

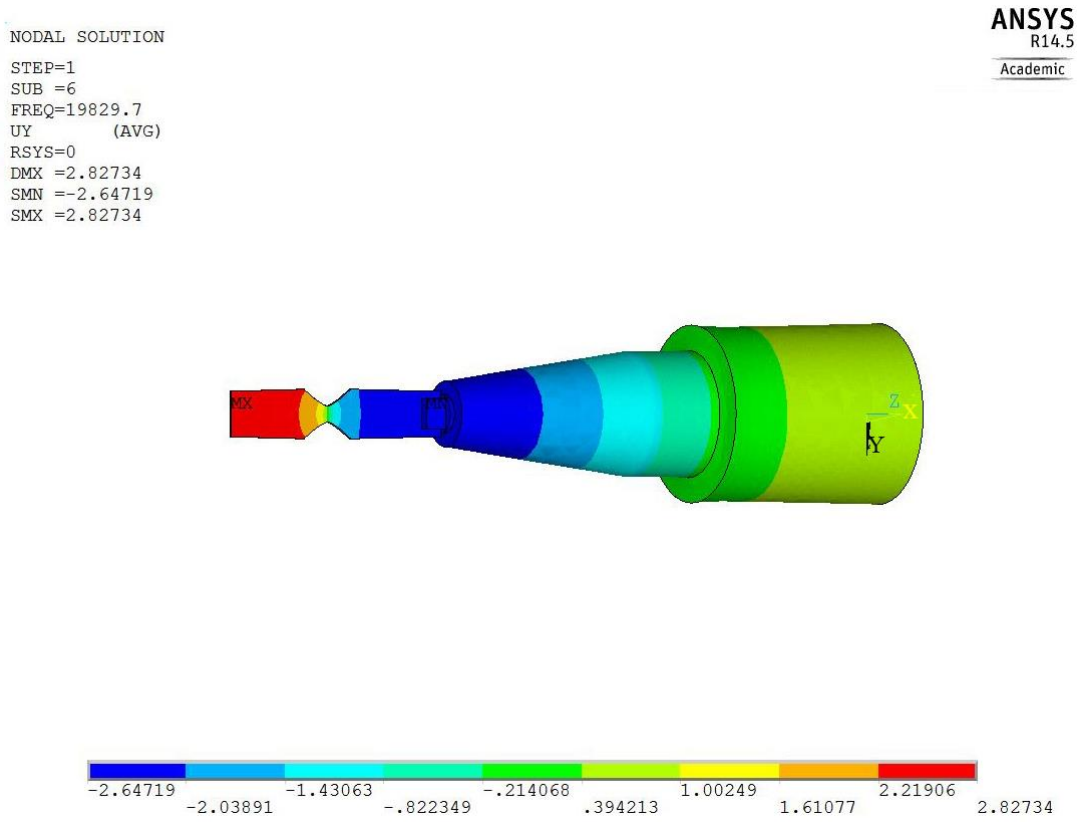

Figure 2.5 Longitudinal vibration mode of the whole fatigue system by modal analysis in ANSYS.

The calculated resonant frequency of the system in ANSYS is found to be 19830 Hz. After machining the specimens, we experimentally find that its working frequency is about 19960 Hz. The kind of frequency error is quite common, which may come from uncertainties on material properties and geometry of components in fatigue system, in

particular the geometry of the interior structure (e.g. the screw depth in the horn). But we think the working frequency (19960 Hz) is the natural frequency of the whole fatigue system, although this frequency is different from the modal frequency of ANSYS simulation. Therefore, when we do harmonic calculation in ANSYS, we prefer the established model to vibrate at its natural frequency (19830 Hz). From ANSYS result, we can deduce the stress magnification factor defined as the ratio of the maximum stress in the reduced section of the specimen and the corresponding displacement at the end of the specimen. Figure 2.6 shows the displacement and stress profiles along the specimen-horn group, on the condition that the end of specimen is applied to 3 μm displacement. By the FEM method, the stress magnification factor is 14.5 MPa/μm.

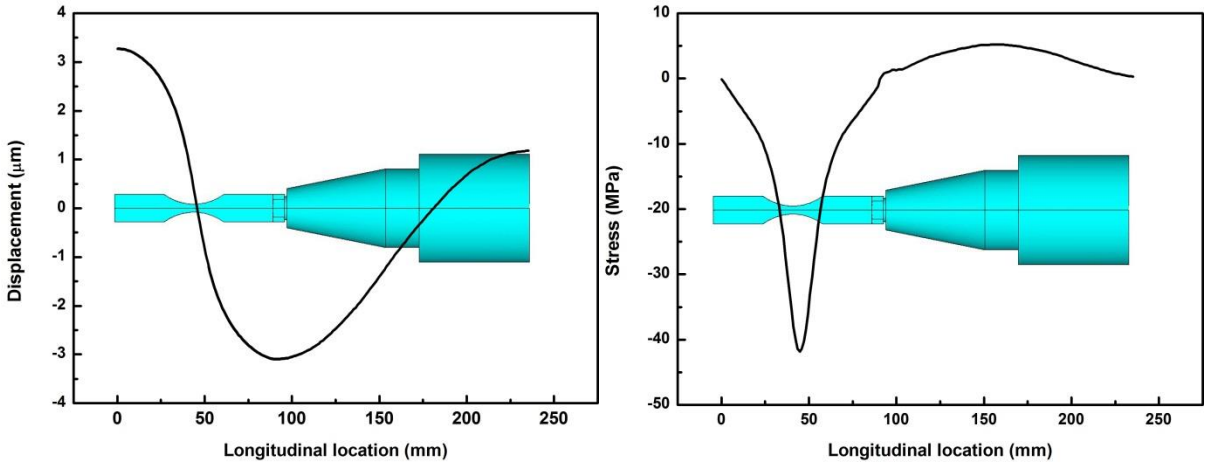

Figure 2.6 Variation of (left) displacement and (right) stress of specimen-horn group under modal frequency.

2.2 Thermodynamic framework

Based on the classical thermodynamic principles and Helmhotz free energy theory, A. Chrysochoos and H. Louche (2000) proposed the link between the temperature and the heat source fields, as specified by the heat diffusion equation:

$$\rho C_p \dot{T} - k\Delta T = d_1 + S_{thm} + r_e \qquad (2.8)$$

where ρ and C_p denote the mass density and the specific heat respectively. k is a constant, assuming an isotropic heat conduction of the material. Δ is the Laplacian operator. T is the absolute temperature. The right hand member of equation (2.8)

consists of three heat sources. d_1 represents the intrinsic dissipation. The thermo-mechanical coupling source S_{thm} is composed of the thermoelastic coupling source S_{the} and other possible thermo-mechanical coupling sources. In gigacycle fatigue tests, the cyclic loading is assumed with a constant stress amplitude, thus the average value of S_{the} over one cycle is zero. The term of S_{thm} will be neglected in the thesis, as suggested by Boulanger et al. (2004). Meanwhile, r_e denotes the external heat source. Here, r_e is time independent and can be reduced by introducing the relative temperature $\theta_{3D}(x, y, z, t)$.

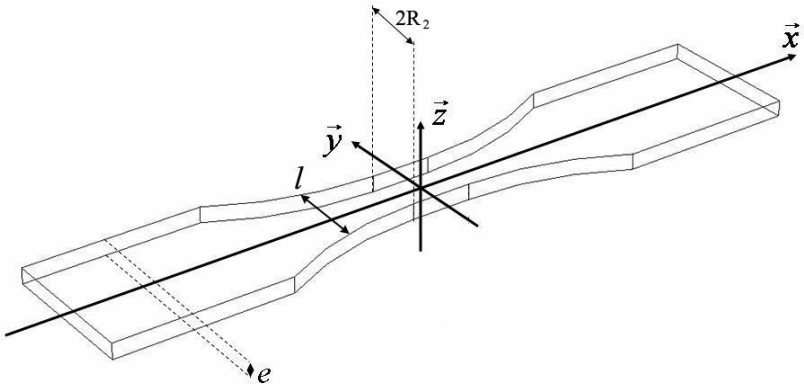

Figure 2.7 Dimension of the plate specimen.

In self-heating tests, a plate specimen with non-uniform cross section is used, as shown in Figure 2.7. The intrinsic dissipation will be calculated, based on the thermal response on the ***xy*** surface. In order to apply the heat equation (2.8) in the case of 2D thermal image processing with non-uniform cross-section, Doudard et al. (2007) proposed a simplified heat equation in 1D diffusion model, the conduction losses $k\Delta T$ can be deduced from an analysis of mean losses on each cross section, by introducing the temperature field:

$$\theta(x,t) = \frac{1}{S}\int_{-e/2}^{e/2}\int_{-l/2}^{l/2}\theta_{3D}(x,y,z,t)dydz \qquad (2.9)$$

The heat equation (2.8) can be rewritten as a 1D thermal diffusion problem:

$$\rho C_p\left(\frac{\partial\theta(x,t)}{\partial t}+\frac{\theta(x,t)}{\tau^{1D}}\right)-k\left(\frac{\partial^2\theta(x,t)}{\partial x^2}+\frac{\partial\theta(x,t)}{\partial x}\frac{\partial S(x)}{\partial x S(x)}\right)=\bar{d}_1(x,t) \quad (2.10)$$

with a characteristic time τ^{1D}:

$$\tau^{1D}(x) = \frac{\rho C_p el}{2h(e+l)} \quad (2.11)$$

where, $\bar{d}_1(x,t) = \frac{1}{S}\int_{S(x)} d_1 dS$ with *S(x)* representing the area of cross section on *x*; the constant *h* represents the lateral heat exchange coefficient between the surrounding air and the sample; *e* is here the thickness of the plate sample, *l(x)* denotes the width of the cross section at point *x*.

In the following parts, we will call and use $\tilde{d}_1 = \bar{d}_1/f$ the dissipated energy per cycle. Its value will be taken at the center of the specimen during stabilization stage. As the camera frequency (3.75 Hz) is much lower than the cyclic test frequency (20 kHz), it is not possible for us to evaluate the heat source and its evolution during a cycle from the measurement. So, $\tilde{d}_1$ gives the order of magnitude and an approximate estimation of the mean intrinsic dissipation along one cycle.

2.3 Experimental preparation

Besides the ultrasonic fatigue system, our frequently-used experimental setups in Figure 2.8 are an infrared camera on one side of the specimen and an optical microscope on the other side. The microscope is composed of a CCD color camera surmounted by a microscope objective lens and will be used to follow the microstructural evolution of the specimens during ultrasonic fatigue testings. The working frequency of this optical microscope camera is usually setted as 1 Hz. The light source for the camera is warm light from a small incandescent light bulb, so that the background of recordings looks a little brown-yellow in chapter 3.

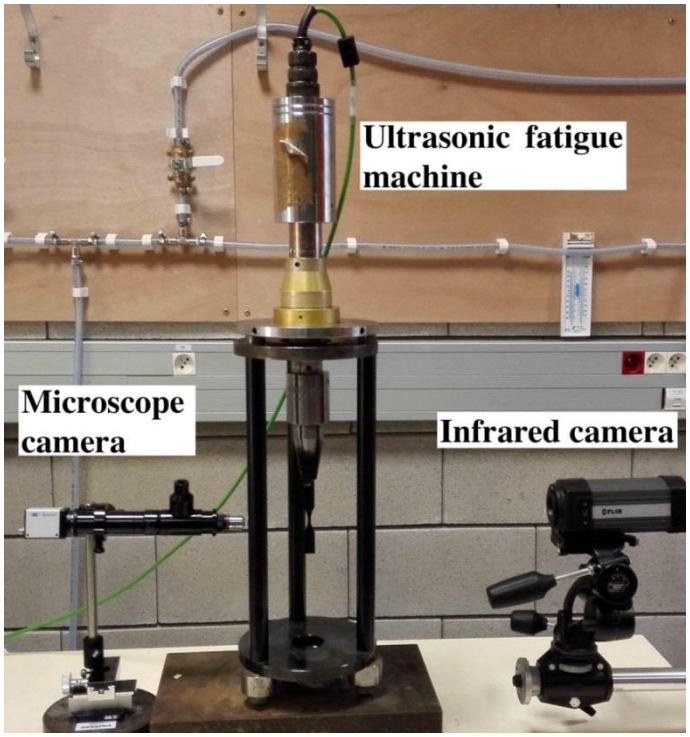

Figure 2.8 Experimental devices in this work.

In order to record the temperature field on the specimen surface, an infrared (IR) camera Flir A325 is used. This is a microbolometer-based camera with a 320×240 detector and a thermal resolution (noise equivalent temperature difference, NETD) of 0.1 ℃. The IR camera acquisition frequency is always fixed to 3.75 Hz. The spectral range of the camera is between 7.5 μm and 13 μm and it can be used to record temperature from 0 ℃ to 350 ℃. One side of the specimens is sprayed with a strongly emissive black paint to obtain a surface emissivity factor close to one.

Preparation of specimens includes the mechanical polishing and electrolytic polishing. The received metal bars are machined into flat specimens with the thickness of 1 mm and the specimen geometry is shown in Table 2.1. All the machined specimens need to be polished mechanically with a sequence of SiC papers (180#~2000#), finished with a 0.25 μm diamond paste.

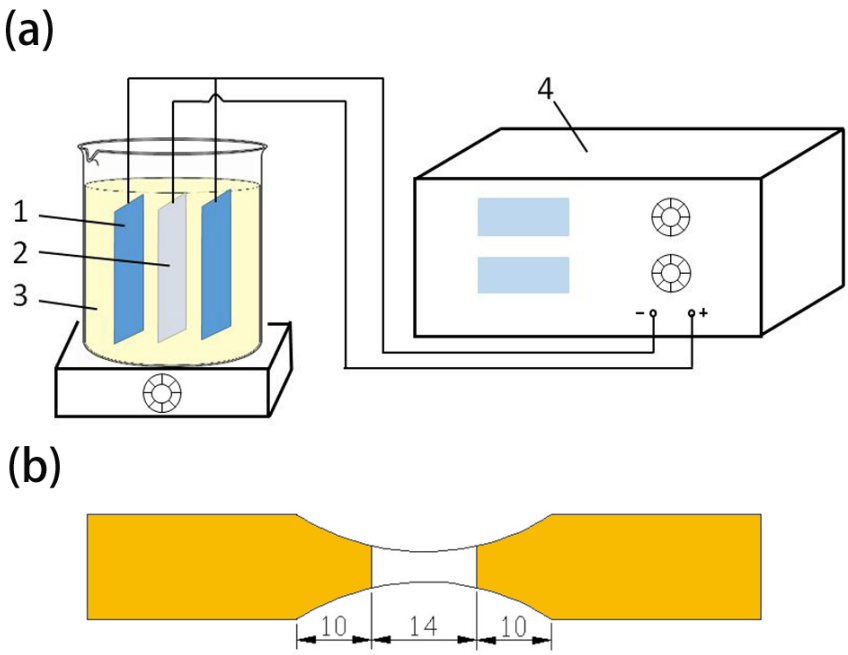

Figure 2.9 (a) Schematic figure of electrolytic polishing: 1. electrode; 2. specimen; 3. electrolyte solution; 4. power source. (b) The dimension of specimen covered by brown anti-corrosion tapes. (mm)

To reveal the microstructure of the specimens and for optical microscope recording observations during tests, the samples are necessary to be electrolytically polished and etched by using Struders A2 solution. The setups are showed schematically in Figure 2.9a. The flow rate of electrolyte solution has to be adjusted by experience. In order to not change the polishing condition, it's better to keep constant the area size to be polished. Before electrolytic polishing, the surface needs to be covered and protected by the brown anti-corrosion tapes. Since our polishing machine POLISEC C25 is not easy to adjust the voltage during polishing treatment, the uncovered area should be precisely controlled as Figure 2.9b. Although various steels have their own best voltages for polishing, they always can get the good polishing surface with the current of 0.9~1 A for 50~60 s, while etching condition is 0.01 A for 30 s.

2.4 Conclusions

This chapter concerns the design and calibration of plate specimen under 20 kHz fatigue loading. Through harmonic calculation in FEM, the stress magnification factor is calculated as 14.5 MPa/μm.

Chapter 3 Effect of pearlite phase fraction on thermal response in α-iron and C-Mn steels

This chapter investigates the effect of pearlite phase ratio on thermal responses and fatigue behaviors of an α-iron and two carbon steels (C12 and C65 steel), in self-heating fatigue tests as well as fatigue tests.

In this chapter, we focus on the thermal responses of these three materials in iterative self-heating tests. By means of in situ infrared thermography, a series of interrupted fatigue tests are carried out with increasing the stress amplitude, and the temperature field on specimen surface is recorded. The involved mechanisms are investigated based on the temperature curve and the microstructural changes. Besides, effect of loading sequences, i.e. “from high to low stress amplitude” and “from low to high stress amplitudes”, on thermal response are compared for these three materials.

3.1 Materials properties and preparations

3.1.1 Compositions and properties

The studied materials are a polycrystalline α-iron (1 mm thickness plate) and two dual-phase ferrite-pearlite steels (C12 and C65 steel, round bars of 25 mm and 28 mm diameter respectively). The chemical elements contents are listed in Table 3.1, whose carbon contents are 0.008 wt%, 0.028 wt% and 0.61 wt%, respectively. In spite of the very low carbon in steel named C12 (0.028%) which corresponds rather to a "C3", this steel will be named after C12 as the purchaser told to us. From these chemical analysis, it appears that the C12 steel has the highest nitrogen content and the least aluminum content. Probably, this steel is a little sensitive to DSA (cf. Chapter 4). Figure 3.1 shows their microstructures on specimen surface observed by optical microscope. The bright grains are ferrite and the dark are pearlite. Their grain sizes are very similar, about 20-50 μm. The grain orientation for C12 steel is performed by Electron Black Scattering Diffraction (EBSD) and no special orientation is found in Figure 3.2.

Table 3.1 Mass percentage (in wt%) of chemical elements.

Material	C	N	Al	Si	Mn	S	P	Cu	Ni	Cr
α-iron	0.008	0.002	0.0016	0.005	0.048	0.0035	0.007	0.001	0.014	0.015
C12	0.028	0.0175	0.0002	<0.03	0.4	0.028	0.12	<0.095	0.039	0.024
C65	0.61	0.0085	0.0091	0.24	0.71	0.012	0.02	0.17	0.089	0.1

Figure 3.3 is the surface mophorlogy of C12 steel without etching. Pearlite phase and precipitations are marked in the photo. Lamellar cementite of pearlite phase can be observed in Figure 3.4. For the C12 steel with the higher sulphur content, elongated inclusions in the longitudial direction of the bars are found (Figure 3.1). Energy Dispersive Spectrometer (EDS) is used to measure the compositions of the precipitations. From Figure 3.6, we can know that the inclusions are mainly maganese sulfide (MnS). Figure 3.5 provides SEM photos of inclusions in the longitudinal and transverse direction of C12 steel.

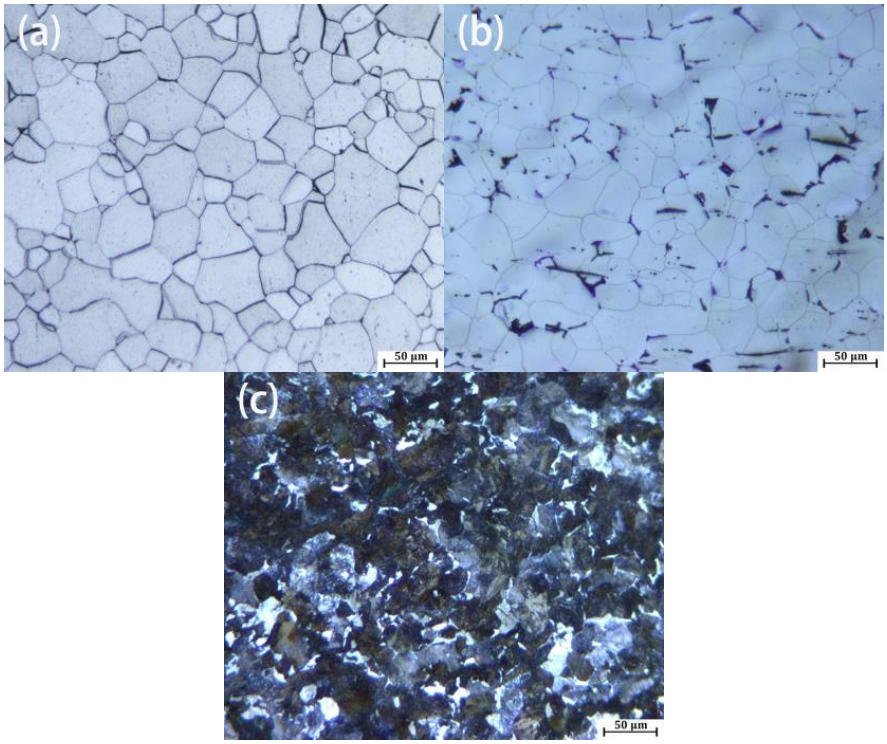

Figure 3.1 Microstructure of (a) α-iron, (b) C12 steel and (c) C65 steel.

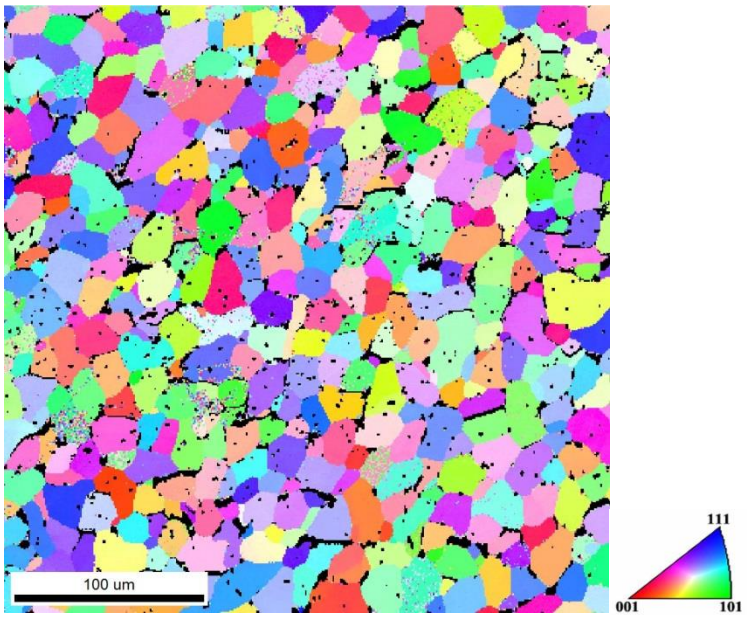

Figure 3.2 Grain orientations on C12 steel investigated by EBSD.

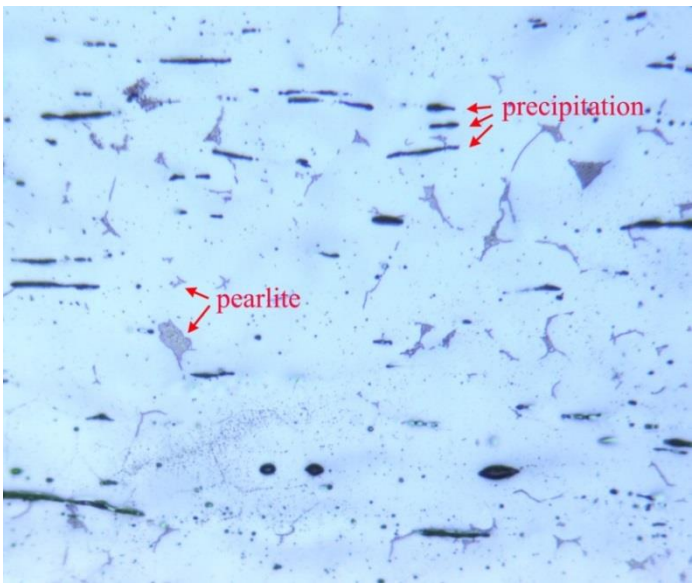

Figure 3.3 Surface of C12 specimen without etching.

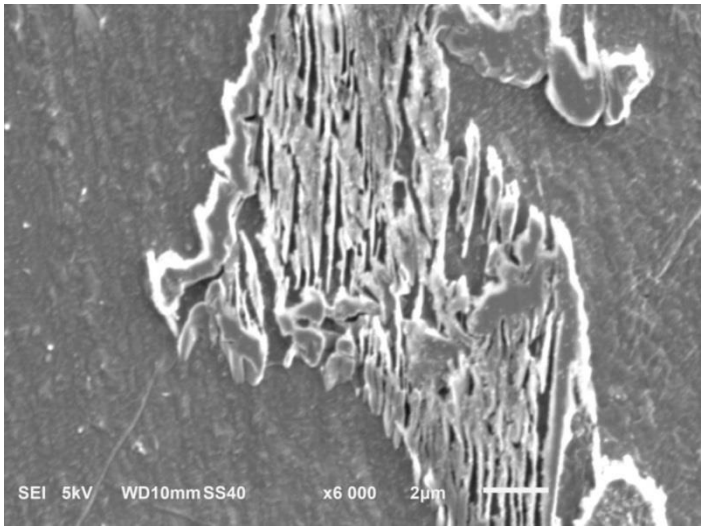

Figure 3.4 Lamellar cementite of pearlite phase in C12.

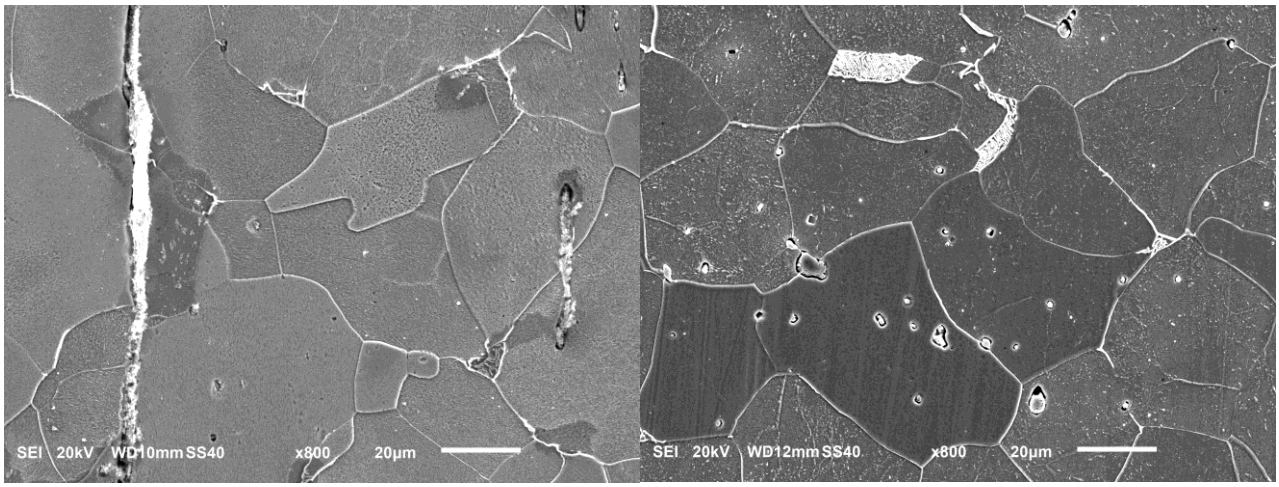

Figure 3.5 Inclusions in C12 steel (left) in the longitudinal direction and (right) in the transverse direction.

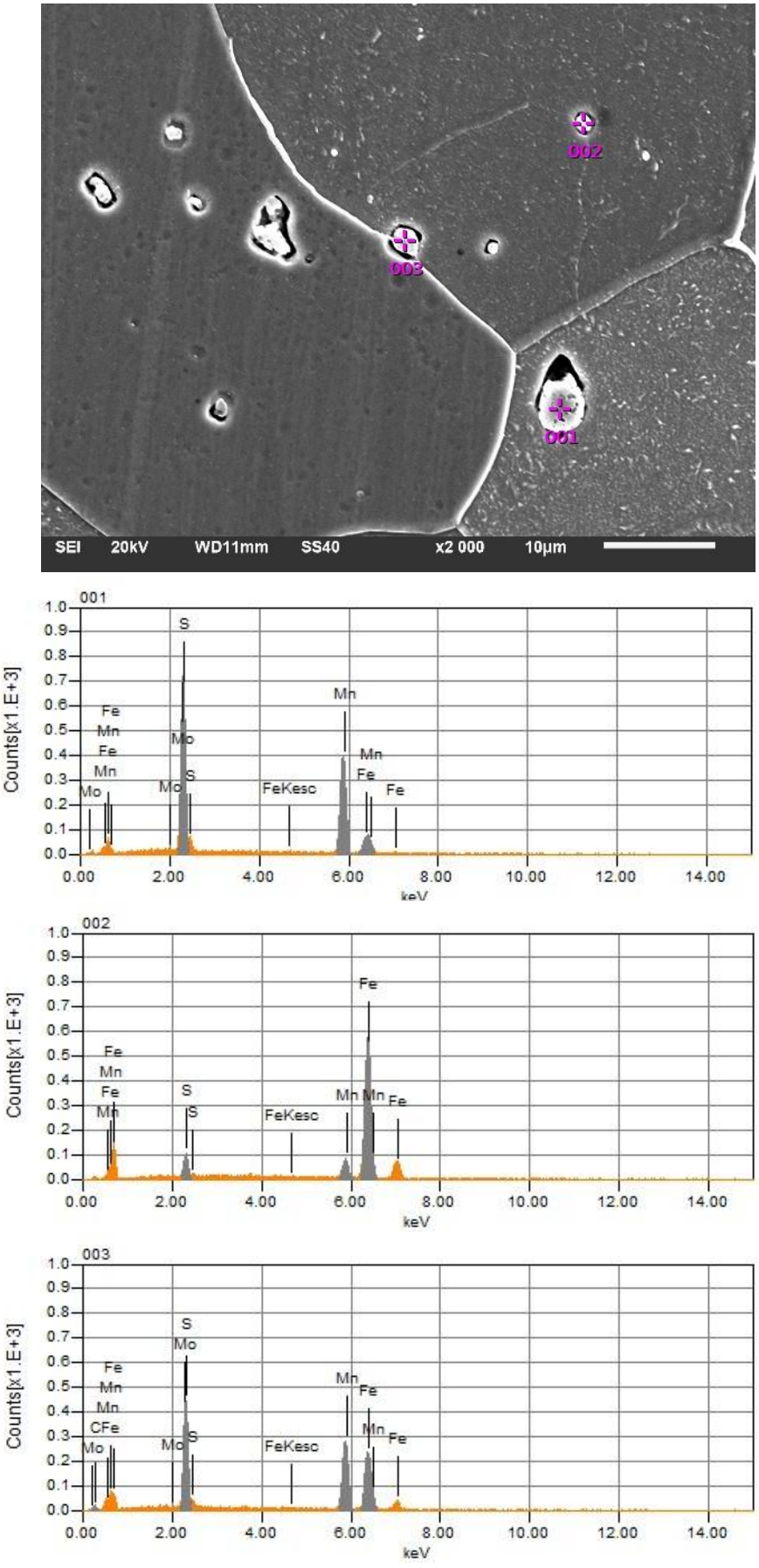

Figure 3.6 Composition of the inclusions in C12 steel determined by EDS.

The percents of ferrite and pearlite phase measured from Fe-C phase diagram are listed in Table 3.2.

Uniaxial tensile curves of three steels are displayed in Figure 3.7, and the corresponding mechanical properties are listed in Table 3.3. Increase of carbon content enhances largely the strength and reduces the ductility. Thermal conductivity $\boldsymbol{k}$ and specific heat $\boldsymbol{C_p}$ are measured for these materials by the transient plane source method, also listed in Table 3.3.

Table 3.2 Mass percentage of proeutectoid ferrite/pearlite phase.

Material	Proeutectoid ferrite (wt%)	Pearlite (wt%)
α-iron	100	0
C12	98.9	1.1
C65	16	84

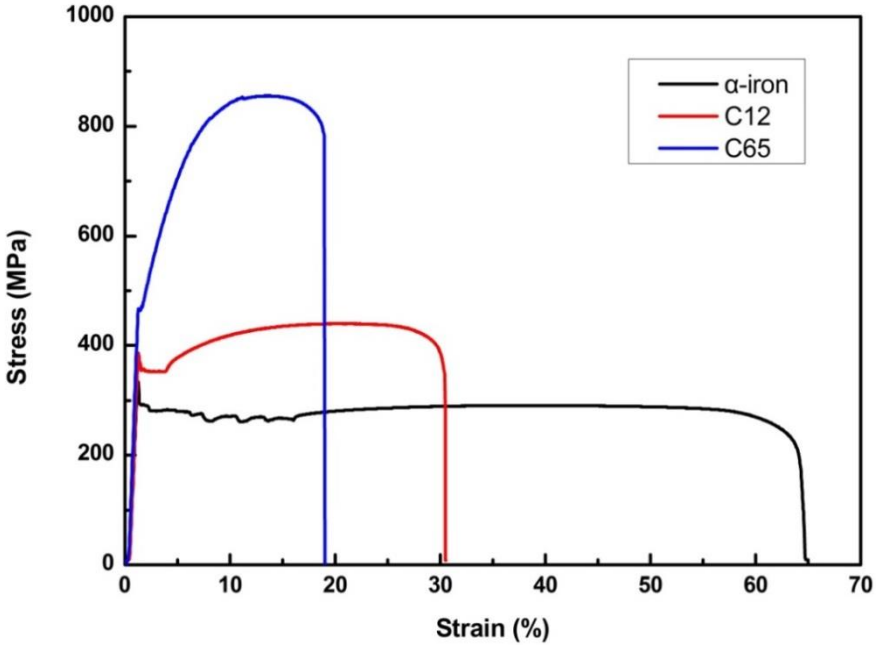

Figure 3.7 Uniaxial tensile tests of α-iron and two carbon steels.

Table 3.3 Mechanical and physical properties of three materials.

Material	Lower yield stress (MPa)	Ultimate tensile stress (MPa)	C_p (J kg^{-1} K^{-1})	k (W m^{-1} K^{-1})
α-iron	288	320	469	76.9
C12	357	446	458	60.7
C65	467	860	473	42.3

3.1.2 Experimental procedure

All the specimens are machined as Figure 3.8. The mechanical polishing is necessary for all the specimens to remove the rust on surface, and the electrical polishing is used for optical microscope observations during tests. The details of operation have been intruduced in chapter 2.

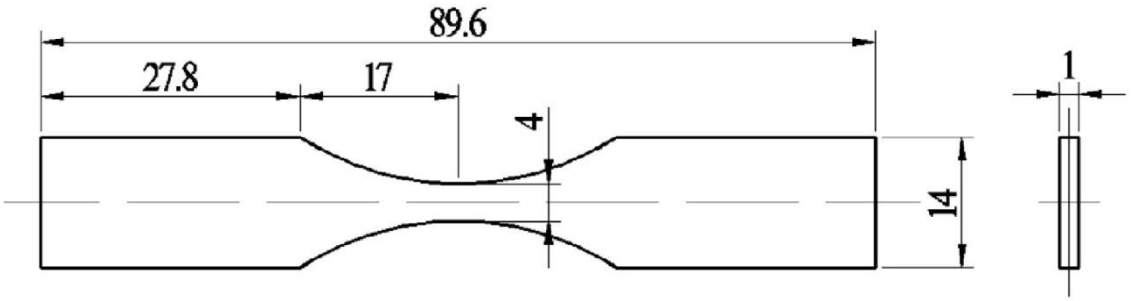

Figure 3.8 Geometry of specimens in ultrasonic fatigue tests.

The self-heating tests performed on each steel consist of a series of cyclic loadings with an increase of stress amplitude, as illustrated in Figure 3.9. At each stress amplitude, a fatigue test is carried out up to 2.5×10^7 cycles when the specimen temperature is stabilized for a long period, and then interrupted. After the specimen cools down to the room temperature, another loading step restarts for a next loading step. Temperature field on specimen surface is registered at each step by infrared camera.

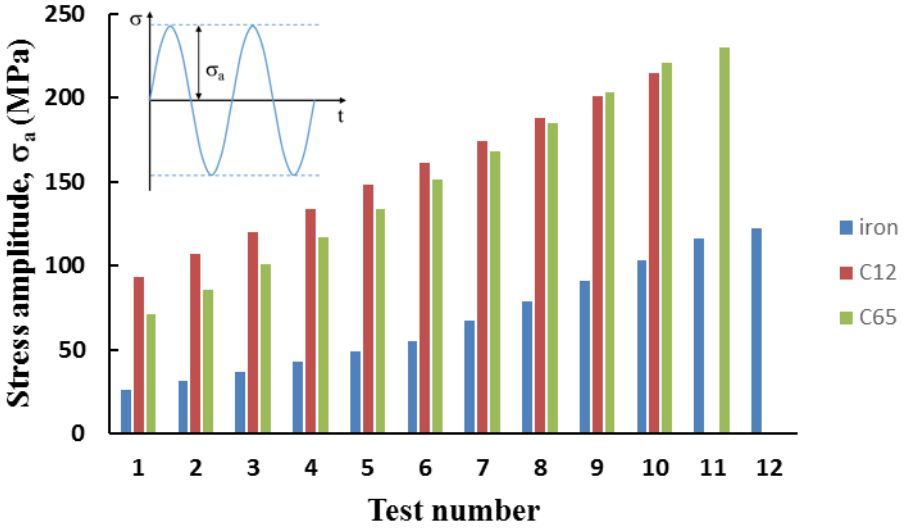

Figure 3.9 Successive fatigue loadings in iterative self-heating tests (each block corresponds to 2.5×10^7 cycles).

For instance, Figure 3.10a shows the temperature field on the specimen surface at 2.5×10^7 cycles and Figure 3.10b is the evolution of the mean temperature T extracted from the rectangular zone in Figure 3.10a during one loading step. According to the temperature evolution profile, two periods can be distinguished: first, the specimen temperature increases rapidly at the beginning (Period I, $< 1\times10^7$ cycles) and then, it reaches the stabilization (Period II, 1×10^7 cycles ~ 2.5×10^7 cycles).

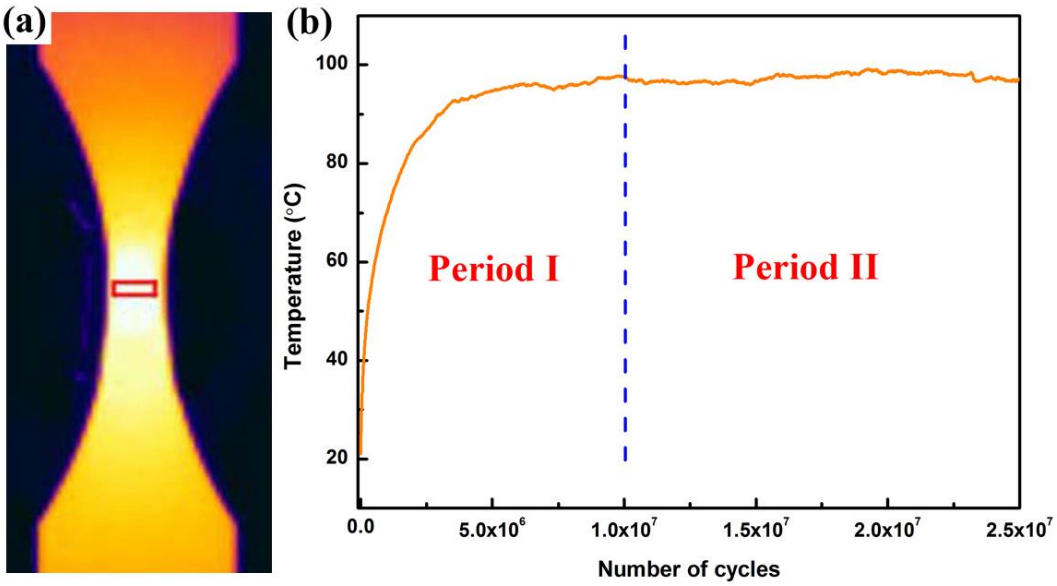

Figure 3.10 Schematic illustrations for α-iron at one loading step. (a) Temperature field on specimen surface at 2.5×10^7 cycles; (b) partition for Period I and Period II in temperature evolution curve.

The temperature elevation ΔT is the mean temperature variation ($\Delta T=T - T_{ini}$) in the rectangular zone and T_{ini} is the mean initial temperature of the specimen that is recorded each time before starting the tests.

3.2 Results

3.2.1 Self-heating tests

1. Temperature variation during cycling

The temperature evolutions T for some of the loading steps with different stress amplitudes are shown in Figure 3.11. This figure shows that by increasing the stress amplitude, regardless of the type of steel, the specimen temperature evolves in accordance to Figure 3.10. It is worth noting that in the case of α-iron loaded at 122

MPa, the temperature suddenly increases (Figure 3.11a) but no fracture is observed. Figure 3.12 is the corresponding IR screenshots of α-iron at 122 MPa. Similarly, for C12 (Figure 3.11b) and C65 steels (Figure 3.11c), the specimen temperature also reaches several hundreds of degrees at 228 MPa and 230 MPa respectively, without specimen fracture. The self-heating test is stopped, since the temperature is beyond the upper measurement limit (350 ℃) of the infrared camera. Figure 3.12 is the screenshots of infrared camera recording for α-iron, corresponding to the temperature curve at 122 MPa in Figure 3.11a. The detailed temperature field around the sudden temperature increase could be considered homogenous as displayed in Figure 3.12b and this temperature change is not related to crack formation. Figure 3.13 shows the appearance of α-iron after the sudden temperature increase. It doesn't fracture and presents a colorful zone in the central part due to oxidation at high temperature.

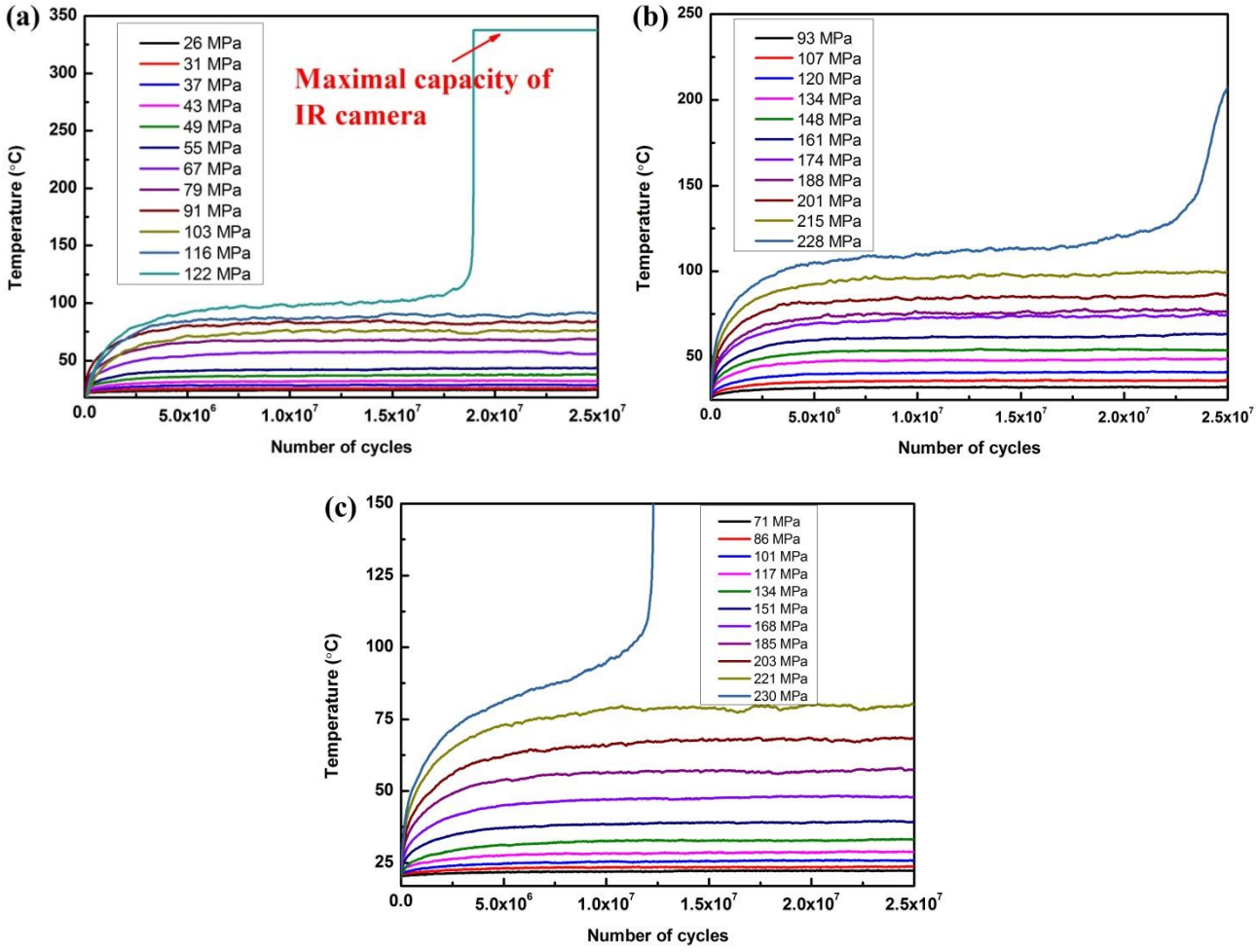

Figure 3.11 Temperature evolutions versus number of cycles under different stress amplitude for (a) α-iron, (b) C12 steel, (c) C65 steel.

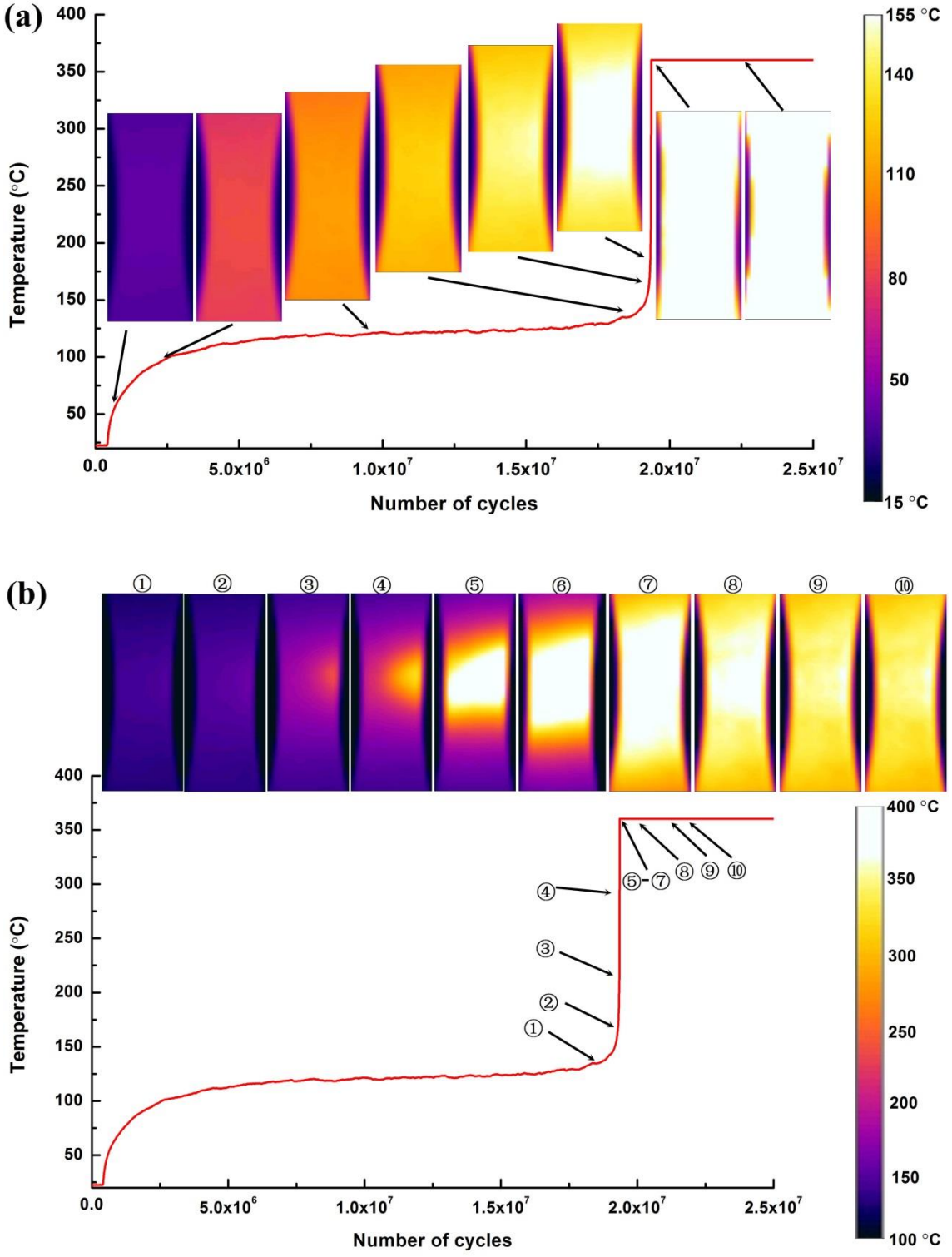

Figure 3.12 Screenshots of α-iron specimen in self-heating test of 122 MPa displayed in Figure 3.11a. (a) Temperature field during the whole test; (b) The detailed temperature field changes when the sudden temperature increase up to hundreds of degrees.

Figure 3.13 Photo of α-iron specimen after successive self-heating tests displayed in Figure 3.11a.

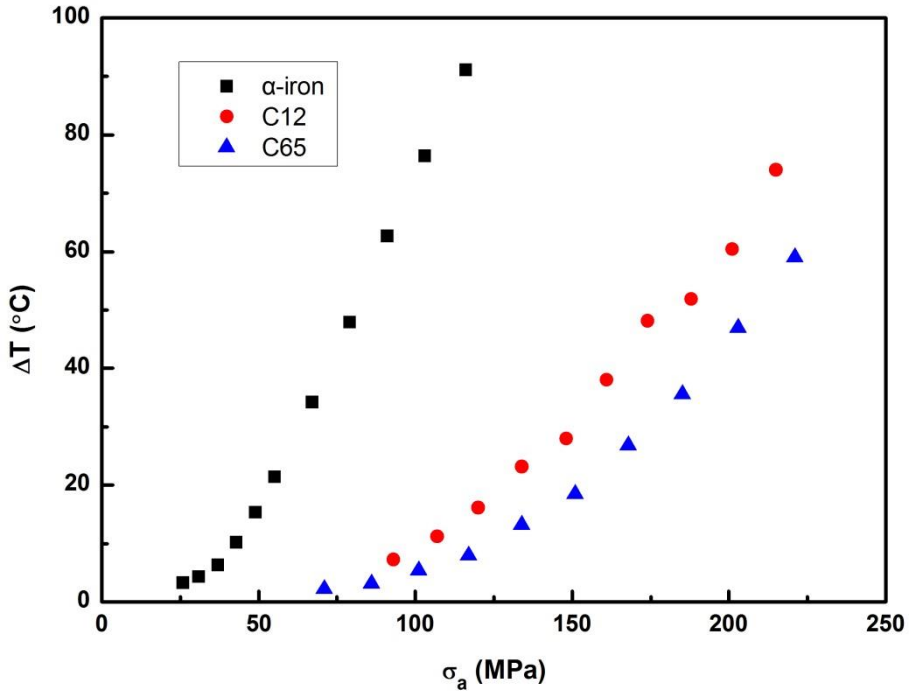

Figure 3.14 Temperature increase ΔT at stabilization state (Period II) of three steels in self-heating tests.

For each loading step in Figure 3.11, the stabilized temperatures reached during Period II are plotted for the three steels in Figure 3.14. Figure 3.14 shows that the temperature elevation ΔT increases gradually by increasing the stress amplitude. The relation of stress amplitude and temperature elevation is obviously non-linear. The maximum stabilized temperature increase ΔT before the sudden increase is ~90 ℃ for α-iron, ~75 ℃ for C12, and ~60 ℃ for C65, respectively.

2. Calculation of intrinsic dissipation

In our work, no cooling air is applied around the specimen and horn. Only, the cooling air (2 bars) from a thin tube is used to cool down the converter (Figure 2.1). It is assumed approximately that there is no forced air around flat specimens and the heat

exchange between specimens and air can be considered as natural convection. For the air natural convection, the heat exchange coefficient *h* should be in the range of 5 to 25 W/(m^2·K) (Yang, 2002).

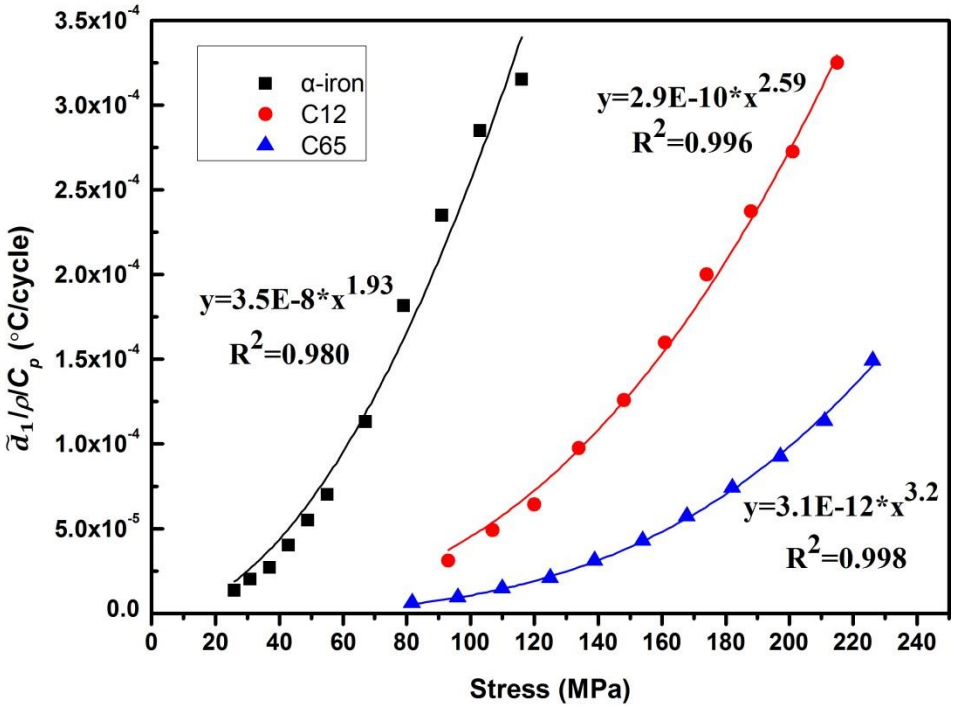

Figure 3.15 Dissipated energy per cycle versus stress amplitude under ultrasonic loading. The solid points are calculated from equation (2.10) at 2.5×10^7 cycles.

Figure 3.15 shows the measured dissipated energy per cycle as a function of stress amplitude, calculated from equation (2.10), under the condition of the *h* value equal to 8. Due to the uncertainty of *h* at the range of 5~25 W/(m^2·K), the maximum error to d_1 is less than 10%. The higher stress amplitude produces the higher dissipated energy. At a given stress amplitude, α-iron always dissipates the most energy, while C65 steel releases the least dissipation. The curves could be well fitted as the power function, and their power exponents increase with carbon content.

3. Effect of loading sequences on thermal response

In this section, we compare the thermal response of α-iron and two carbon steels at different loading sequences, i.e. from high to low amplitude, or from low to high stress amplitude, as explained in Figure 3.16. The applied stress amplitude in self-heating tests

are carried out as Table 3.4. The same experimental condition and operations in experiments are kept. At each stress amplitude, the fatigue test is carried out until 2.5×10^7 cycles. After the specimen cools down to the room temperature, another loading step restarts.

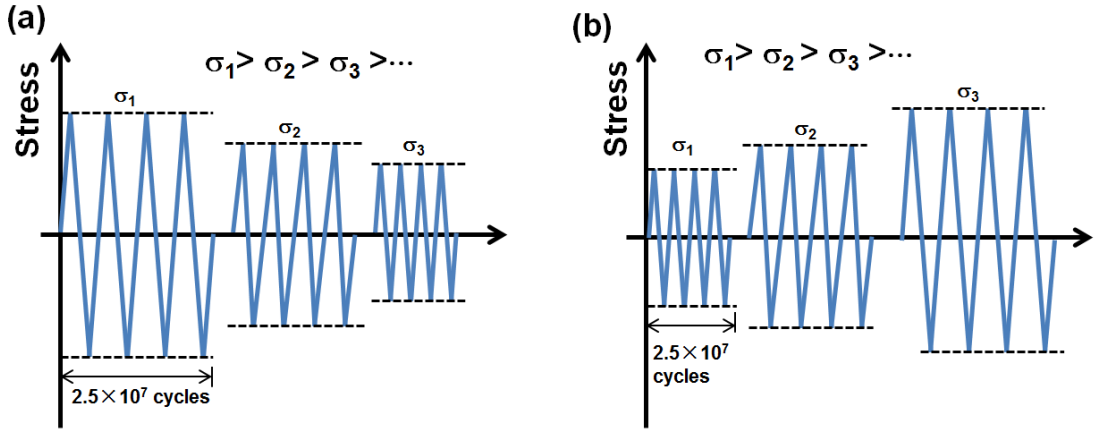

Figure 3.16 Spectrum of loading sequence in multiple step self-heating tests (a) from high to low stress amplitude, (b) from low to high stress amplitude.

Table 3.4 List of interrupted loading range (2.5×10^7 cycles at each stress amplitude)

Specimen N°	Stress in self-heating tests	Corresponding Stress tendency
C0-1#	26 MPa → 122 MPa	low → high
C0-2#	122 MPa → 26 MPa	high → low
C65-1#	81.6 MPa →197 MPa	low → high
C65-2#	197 MPa → 81.6 MPa	high → low
C12-1#	93 MPa → 201 MPa	low → high
C12-2#	201 MPa → 93 MPa	high → low

Figure 3.17(a, b) and Figure 3.17(d, e) are the temperature evolution of α-iron and C65 in the cases of increasing and decreasing the stress amplitude, respectively. Regardless of the stress amplitude, all the temperature evolution curves for α-iron and C65 show clearly that specimen temperature always increases quickly, and then reach the stabilization. Nevertheless, the temperature fluctuation of stabilization stage in C65-2# is larger, especially the black curve at 197 MPa. Figure 3.17(c, f) show the temperature elevation ΔT versus the stress amplitude. When the stress amplitude decreases, the ΔT is generally 3 °C ~ 10 °C higher than that when the stress amplitude increases, for α-iron and C65.

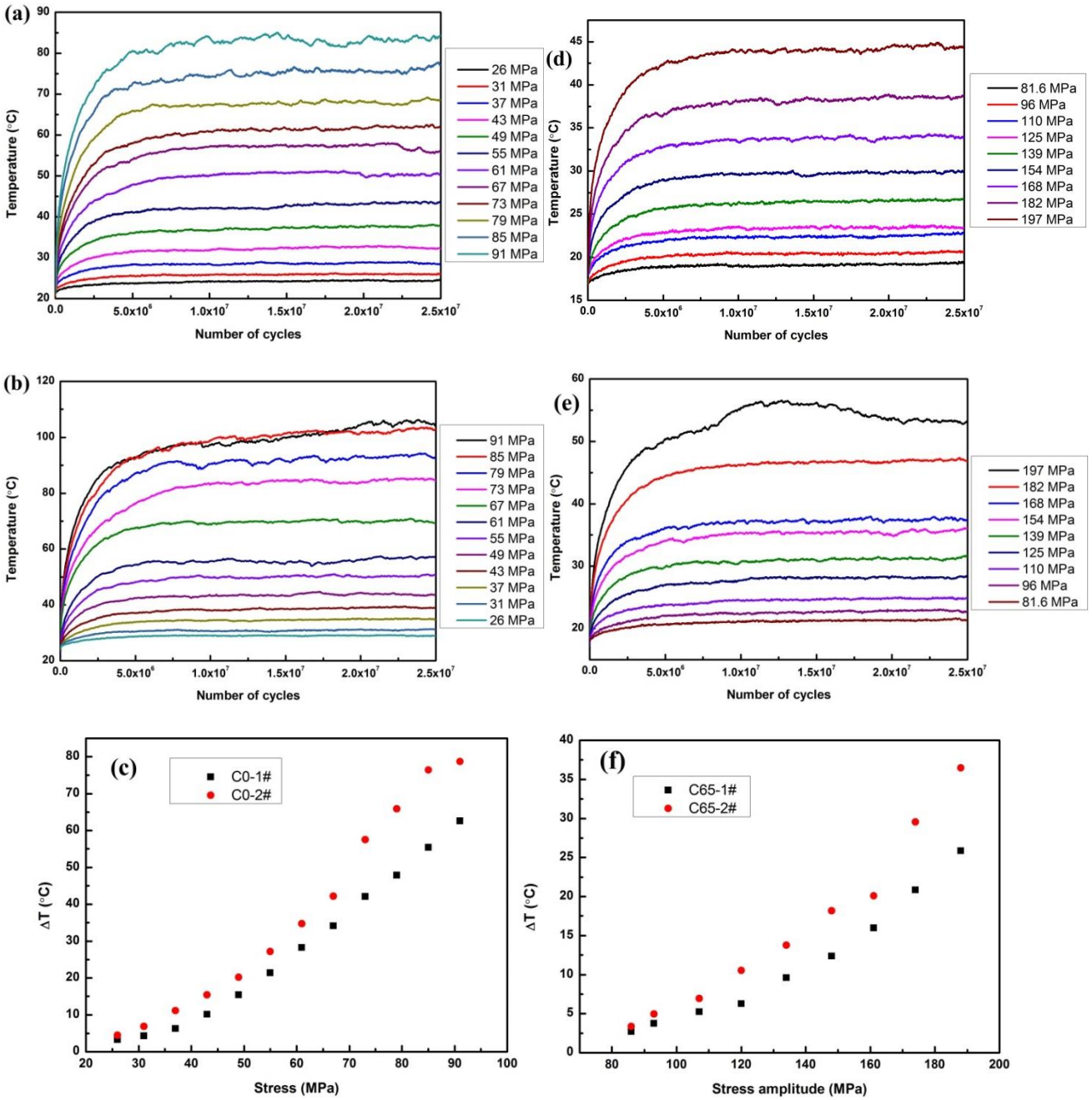

Figure 3.17 Temperature evolution of (a, b) α-iron and (d, e) C65 steel in self-heating tests, (a, d) increasing the stress amplitude; (b, e) decreasing the stress amplitude. (c) and (f) are the temperature increase ΔT of α-iron and C65 in above two cases.

In the case of increasing the stress amplitude, under the first applied stress amplitude, mobile dislocations and dislocations forest will be created in steel. But mobile dislocations gliding is responsible for the specimen temperature elevation, rather than immobile dislocations forest. Dislocations movement in next loading sequence could be hindered by already-formed dislocations forest. So we always observe the weaker temperature increase in these pre-strained specimens.

However, when decreasing stress amplitude, the first maximal stress causes the maximum damage in steel. The maximum stress amplitude has the ability to produce the most dislocations and the longest mean free path in steel, comparing with the subsequently lower stress amplitudes. Supposing that some already-existed mobile dislocations could still move in existed dislocations path in lower stress amplitude, mobile dislocations could glide more total paths than cases of increasing stress amplitudes. The corresponding specimen temperature would be higher than cases of increasing stress amplitudes.

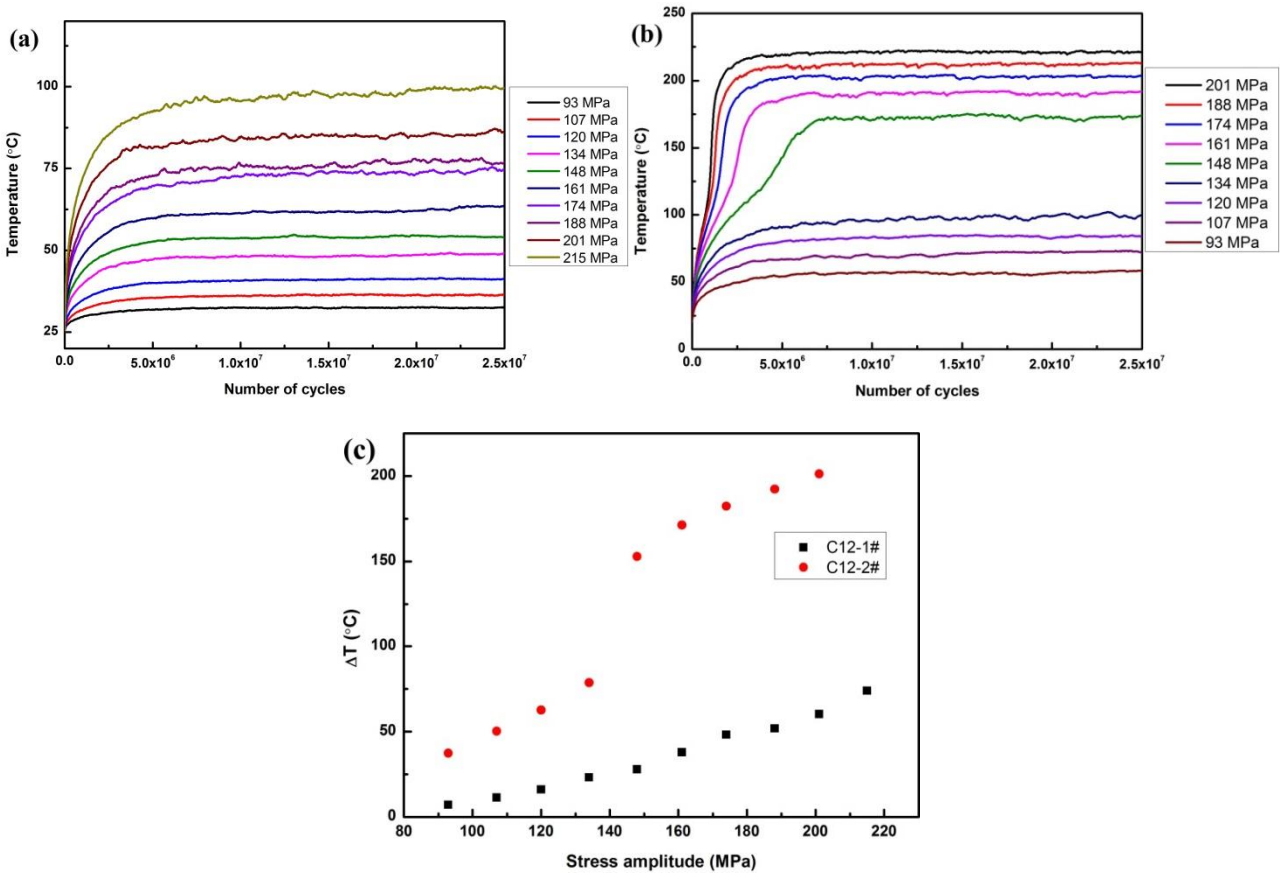

Figure 3.18 Temperature evolution of C12 steel in self-heating tests under the condition of (a) increasing and (b) decreasing the applied stress amplitude, (c) temperature increases ΔT in two cases.

Figure 3.18 are the temperature curves of C12 steels, under the sequence of increasing (C12-1#) and decreasing (C12-2#) stress amplitudes, respectively. Surprisingly, the temperature profiles of C12 in these two cases are rather different. When increasing the stress amplitude, the specimen temperature behaves as α-iron and C65. When decreasing the stress amplitude, at high stress amplitudes, the specimen temperature

shows twice stages of increase: the first increase up to 100 °C then a fast increase, and finally the stabilization.

At low stress amplitudes (increasing or decreasing), the temperature curves don't show the secondary temperature increase any more. In this case, the maximum temperature increase is below 100 °C. They would directly reach the stabilization after the first temperature increase. In Figure 3.18c, the temperature increase ΔT in the case of decreasing the stress amplitude is 30 °C ~ 150 °C higher than that when increasing the stress amplitude.

Comparing Figure 3.17 with Figure 3.18, the great difference in temperature for C12 is not merely caused by the effect of loading sequences. The involved mechanism will be investigated in chapter IV. We will report the same phenomenon as in C12 steel.

3.2.2 S-N curves

Figure 3.19 shows the conventional S-N curve of α-iron, C12 steel and C65 steel. From S-N curve, the fatigue limit at 2×10^9 cycles are about 105 MPa, 190 MPa, and 210 MPa for α-iron, C12 and C65 steels, respectively. Correspondingly, the saturated flow stress ($> T_0$) in self-heating tests from Figure 3.11, are about 122 MPa, 228 MPa and 230 MPa, respectively. Furthermore, this result is a little higher than fatigue limit at 2×10^9 cycles found in the conventional S-N curves. Similarly, DP600 is also published that the estimated endurance limit (253 MPa) from self-heating tests is a little higher than fatigue limit (247 MPa) from traditional S-N curves (Torabiandehkordi, 2017).

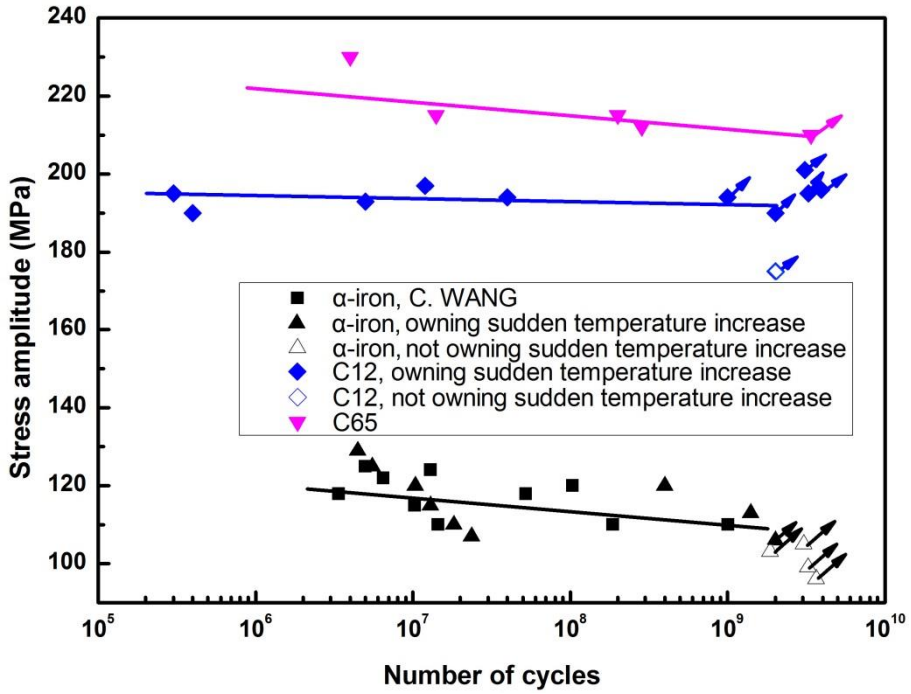

Figure 3.19 Traditional S-N curves of α-iron, C12 steel and C65 steel. The black square points of α-iron from C.WANG (Wang, 2013).

3.3 Discussion

3.3.1 Mechanisms about sudden temperature increase

According to the characteristics of the temperature evolution in Figure 3.11, the applied stress amplitudes can be classified into two stages:

For α-iron, Stage I: < 122 MPa, Stage II: ≥ 122 MPa

For C12, Stage I: < 228 MPa, Stage II: ≥ 228 MPa

For C65, Stage I: < 230 MPa, Stage II: ≥ 230 MPa

Stage I is for the stress range without the sudden temperature increase, and steels always can reach the stabilization temperature. Whereas, Stage II is for the stress range higher than that in Stage I. The specimen temperature suddenly increases up to hundreds of degrees, and can continue vibrating.

1) Stage II: Stress ranges with the sudden temperature increase

As introduced in chapter I, BCC metals own the strain rate- and temperature-dependent deformation mechanism. At each strain rate, the temperature-dependent deformation mechanism is shown in Figure 3.20. The deformation mechanisms are classified by the transition temperature T_0. Below the transition temperature T_0, it's named as "thermally activated regime" or "thermal regime", and above T_0, it's called as "athermal regime". Below T_0, screw dislocations are nearly immobile and the dislocation movement is dominated by the to-and-fro glide of edge dislocations. Above T_0, the mobilities of edge and screw dislocations become comparable and screw dislocations can cross slips easily. The mobility of screw dislocations is the key point to distinguish thermal regime from athermal regime.

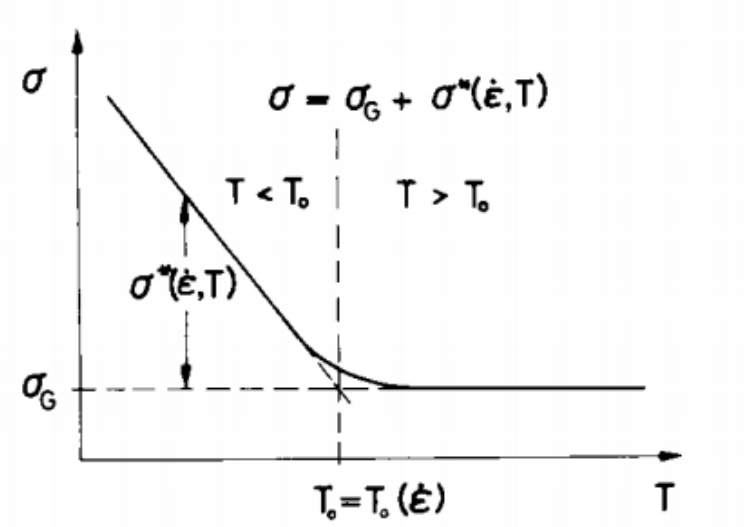

Figure 3.20 Schematic diagram of flow stress in BCC metals versus temperature. (Mughrabi, 2009)

Flow stress $\sigma = \sigma(T, \dot{\varepsilon})$ is defined as the instantaneous value of the stress required to continue plastically deforming the material. It depends on strain rate $\dot{\varepsilon}$, and temperature T for any plastic strain (Mikell P. Groover, 2007) and it can be written as the sum of an athermal stress σ_G and a thermal stress $\sigma^*(T, \dot{\varepsilon})$:

$$\sigma(T, \dot{\varepsilon}) = \sigma_G + \sigma^*(T, \dot{\varepsilon}) \qquad (3.1)$$

Flow stress increases non-linearly with increasing strain rate. For α-iron, below 10^3 s^{-1}, flow stress increases with increasing strain rate (Luo et al., 2017), but decreases with increasing temperature (Abdel-Salam M. Eleiche, 1981; Bao, 2010). For the mild carbon steel, it follows the same rule, as the tensile curves in Figure 1.14. For a given stress rate, flow stress decreases as the temperature rises and levels off to athermal

stress σ_G. The critical temperature from thermal stress to athermal stress is the transition temperature T_0. The transition temperature T_0 would be affected only by strain rate, as shown in Figure 1.16 (Campbell and Ferguson, 1970). Under 20 kHz ultrasonic loading, strain rate lies around $10\sim10^2$ s^{-1}, higher than those ($10^{-3}\sim10^{-2}$ s^{-1}) generally encountered in the LCF and HCF regimes. The high strain rate leads to transition temperature T_0 between the thermally activated regime and the athermal regime for BCC metals (Mughrabi, 2009) far higher than room temperature. In the flow behavior diagram of 0.12 wt% carbon steel (Figure 1.16), T_0 increases from 25 ℃ to 100 ℃ with strain rate from 0.01 s^{-1} to 1 s^{-1} and continue increasing above 200 ℃ when the strain rate reaches 100 s^{-1}.

Generally, flow stress of BCC metals greatly depends on temperature. Moreover, the yield stress at hundreds of degrees drops greatly compared to that at room temperature with the shortening and then the disappearance of the Lüders plateau. As reported by the Figure 3.21, for a carbon manganese steel with 0.2% of carbon, the yield stress decreases from 300 MPa to 150 MPa with the disappearance of the Lüders plateau when the temperature increases from 20 ℃ to 300 ℃.

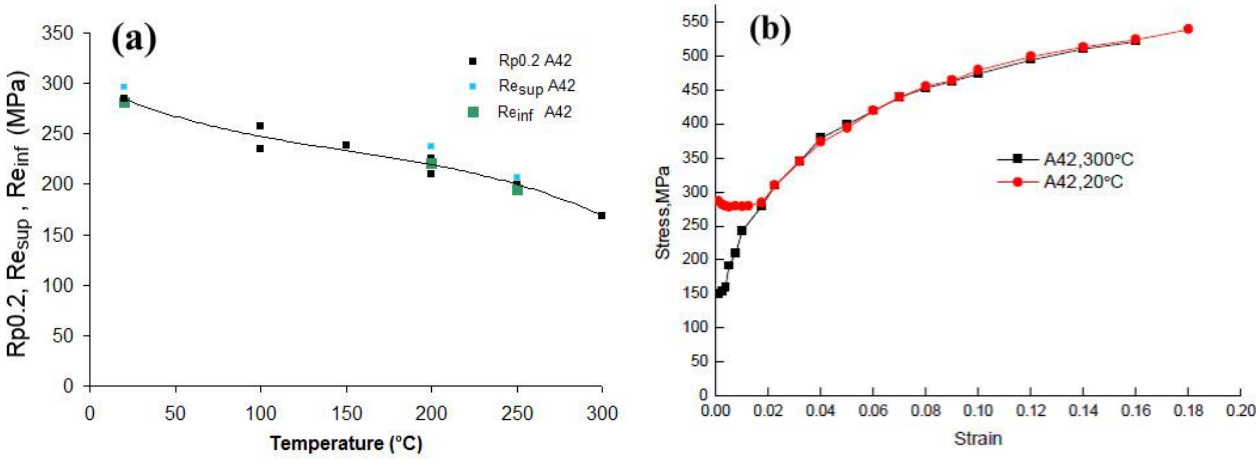

Figure 3.21 (a) 0.2% proof stress (Rp0.2), upper yield stress (Re_{sup}) and lower yield stress (Re_{inf}) of French standard A42 steel. (b) Uniaxial tensile curve of the same steel at room temperature and high temperature. (Huang, 2010)

The sudden temperature increase is an inevitable phenomenon under 20 kHz ultrasonic fatigue loading. Besides our observations, other BCC steels were also published the similar phenomena at 20 kHz high frequency fatigue loading, such as DP600 (Torabian et al., 2016), C45 (Ranc et al., 2015), A42 and A48 (Huang et al., 2016), and so on. The

sudden temperature increase up to hundreds of degrees is always observed when stress amplitudes reach a certain level.

Figure 3.21 presents the surface appearance of α-iron specimen after sudden temperature increase, whose loading history is exactly illustrated in Figure 3.11a. It experiences the sudden temperature increase at 122 MPa from 2×10^7 cycles to 2.5×10^7 cycles. Although the specimen color has changed, we still can see dislocations slips densely distributed on the surface.

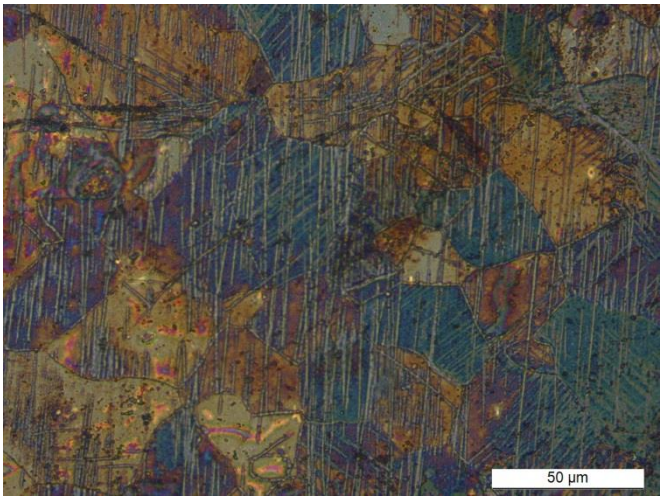

Figure 3.22 Surface of α-iron full of PSBs after the sudden temperature increase.

Marks of the dislocation glide are visible on the specimen surface, and the irreversible microstructure changes also appear in the bulk. This assertion was checked by cutting this α-iron specimen in the center which experiences the self-heating tests shown in Figure 3.11a with the final loading of 122 MPa. Before SEM observation, the cross-section is prepared by gentle polishing and etching by 4% Nital solution. Figure 3.23 displays its SEM photo and schematic illustration of fractograghic observation. Figure 3.24 is the corresponding magnifications of SEM photo in Figure 3.23.

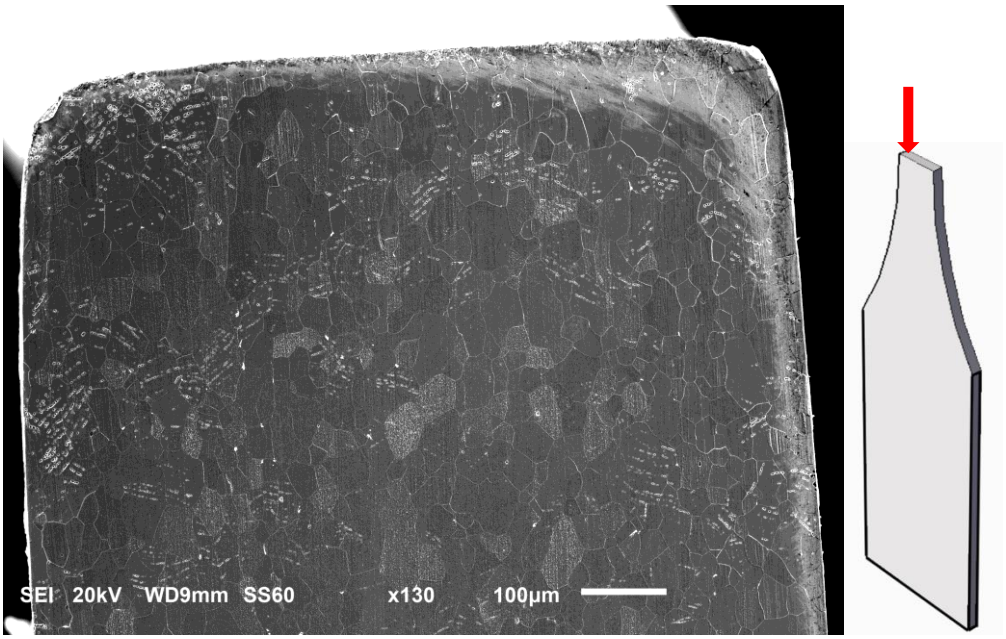

Figure 3.23 SEM photo and schematic illustration of fractograghic observation.

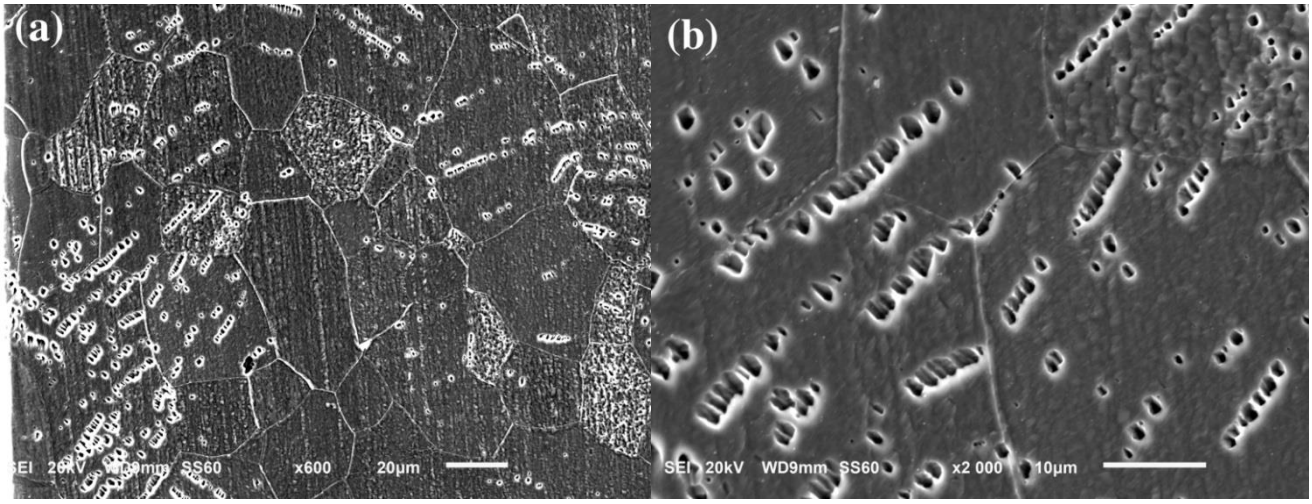

Figure 3.24 Magnification of the micro-voids on cross-section in Figure 3.23.

In Figure 3.23, we can see many “dotted lines” distributed on whole half-surface. In Figure 3.24, these “dotted lines” are the well-ordered micro-voids, about 1 µm. Numerous well-ordered micro-voids exist in some grains, while some other grains seem intact, without any visible damage. An attempt to measure crystal orientation by EBSD failed, because the too much deformation on cross-section which considerably decreases the signal-to-noise ratio. And, electrolytic polishing after multiple attempts is possible to remove the deformed grains. Furthermore, the micro-voids are assembled in straight lines, crossing through the grain and preferentially orientated in localized zones. These

long streaks of micro-voids can sometimes cross the grain boundaries as observed Figure 3.24b.

After the sudden temperature increase, specimen surface appears saturation of dislocation slips and the specimen produces many micro-voids in bulk. Oppositely, we don't observe the similar damage in the specimens without the sudden temperature increase. The associated discussion will be presented subsequently. As to the formation cause of the micro-voids in bulk, it can be explained from the aspect of dislocation intersections.

In dislocations intersections, edge dislocations always lead to the mis-orientation in grains, only intersections between screw dislocations can produce new points defects in materials. The traces of vacancies or voids should be attributed to the movement of jogged screw dislocations (Hull and Bacon, 2011), in Figure 3.25. The jogs formed on screw dislocations are not in the slip plane of original screw dislocations, with account that all resultant jogs would own the characteristics of edge dislocations, i.e. dislocations line is perpendicular to burgers vector, so they would impede the glide of screw dislocations. Screw dislocation takes the jogs with it only by a non-conservative process, as described in Figure 3.25, and the process requires stress and thermal activation. Although jogs are immobile in slip plane, they can climb under enough stress. When subjected to the shear stress on slip plan, due to the inhibition of immobile jogs, the screw dislocation line would bow out between jogs in the slip plane. When the bowing-out radius reaching the critical radius, the stress is enough higher than stress needed for non-conservative dislocation climb. Consequently, the jogs would move forward with the bowing-out circle, leaving a trail of vacancies or interstitials behind each jog, as in Figure 3.25. Certainly, this kind of situation is only suitable to the jogs which are only 1~2 atoms width. When reaching several atoms, jogs are impossible to be moved, owing to strong pinning effect.

However, this micromechanism is impossible to directly produce micron-sized vacancies. From SEM photo in Figure 3.24, we can find that the size of microvoids is ~ 1 μm (after 2.5×10^7 cycles). Another SEM photos (cf. Figure 4.11) show the microvoids have the size about 2~3 μm (after 2×10^9 cycles), and microvoids are interconnected in rows. We suppose that the initially-produced nano vacanies can keep growth by void coalescence under plastic strain, to form micro-voids in SEM photos.

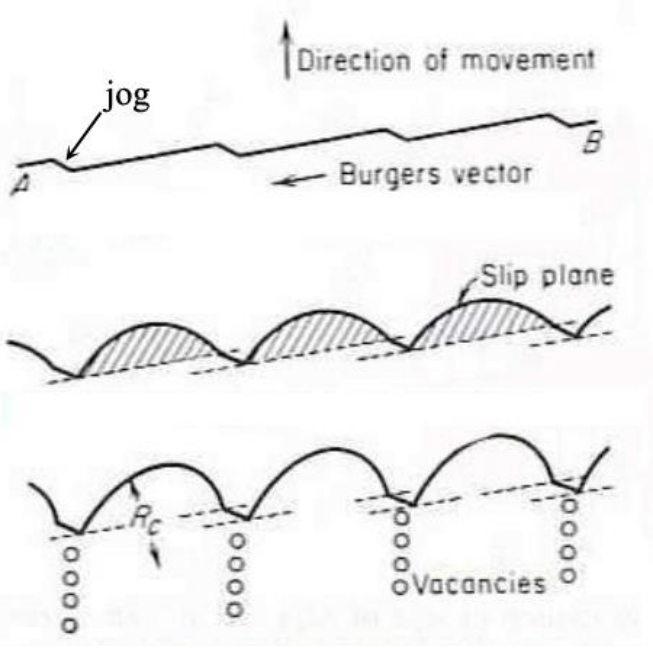

Figure 3.25 Glide of jogged screw dislocation producing trails of point defects. (Hull and Bacon, 2011)

Therefore, appearance of micro-voids aids to confirm that the screw dislocations multiplication has occurred after the sudden temperature increase. And it is verified by the densely-distributed PSBs on the surface (in Figure 3.22), which is possible to be caused by the cross slips of screw dislocations.

Unfortunately, the microstructure evolution during the interrupted fatigue tests was not recorded by the optical microscope camera. So, a new specimen of α-iron was subjected to the stress amplitude of 106 MPa during 2×10^9 cycles while recording the temperature field and the microstructure evolution as previously described in section 3.1.2. Figure 3.27 gives the temperature evolution at the center of the specimen (average on the rectangular zone drawn in Figure 3.10a) and the corresponding persistent slips bands (PSBs) evolutions. The first PSBs occur in few grains (image ①). From the image ③, a sudden temperature rise to hundreds of degrees happens, with the rapid increase of the surface PSBs density.

On the basis of optical observations, it is rational to consider that the sudden temperature rise to hundreds of degrees in Figure 3.11 is caused by multiplication of screw dislocations, corresponding to the transition between thermal and athermal

regimes. The disappearance of the Lüders plateau with the temperature increase probably accelerates this phenomenon. At the image ⑤, the whole view field is full of PSBs. So, no PSBs localization occurs and the specimen still survives at high temperature. That indicates that the steep rise in temperature is not related to crack initiation. Furthermore, due to oxidation at high temperature, the specimen color is observed to change.

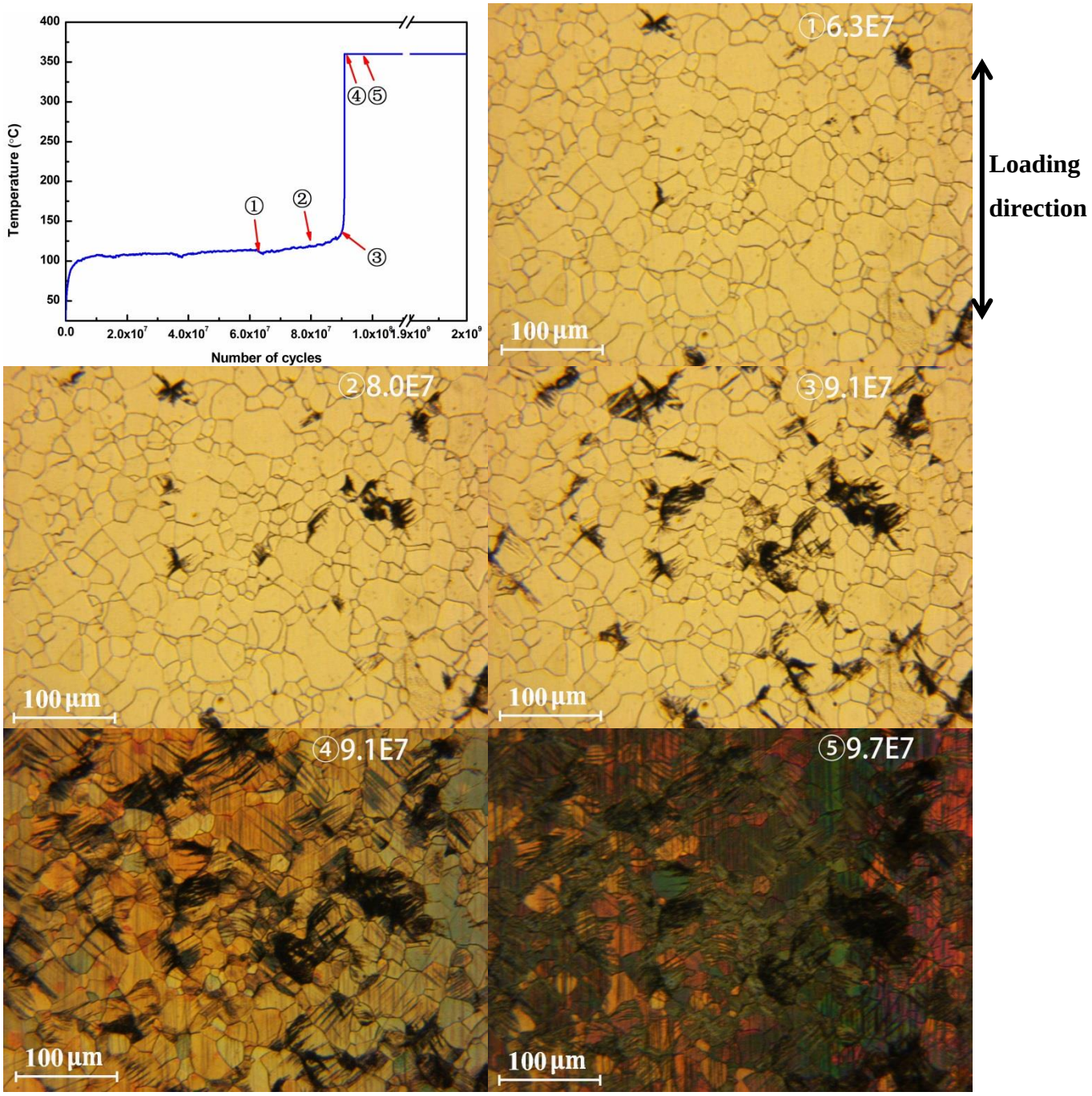

Figure 3.26 Temperature evolution and corresponding microstructure evolution showing the PSBs multiplication along the test of α-iron at 106 MPa.

On the basis of optical observations, it is rational to consider that the sudden temperature rise to hundreds of degrees in Figure 3.11 is caused by multiplication of screw dislocations, corresponding to the transition between thermal and athermal regimes. The disappearance of the Lüders plateau with the temperature increase probably accelerates this phenomenon. At the image ⑤, the whole view field is full of PSBs. So, no PSBs localization occurs and the specimen still survives at high temperature. That indicates that the steep rise in temperature is not related to crack initiation. Furthermore, due to oxidation at high temperature, the specimen color is observed to change.

The same test was performed on the C12 steel at a stress amplitude of 216 MPa until 3×10^9 cycles. The same result could be found with a sudden temperature increase during which the PSBs density rapidly multiplies on surface. According to BCC temperature-dependent mechanism, these experimental phenomena indicate that the sudden temperature increase to hundreds of degrees is related to screw multiplication, implying the transition from thermal regime ($< T_0$) to athermal regime ($> T_0$) under 20 kHz fatigue loading.

For all ferrous dual-phase steels, e.g. ferrite-pearlite steels (Ranc et al., 2015; Huang et al., 2016), and ferrite–martensitic steels (Torabian et al., 2016; Ouarabi, 2018), the sudden temperature increase in self-heating tests is due to the plastic deformation in ferrite phase which is related to the transition from the thermal regime to the athermal regime. Their second phase (i.e. pearlite, martensite), does not belong to the perfect BCC atomic arrangement structure. Pearlite phase is the lamellar alternating layers of ferrite and cementite, while martensite phase has supersaturated carbon. So the second phase is possible not to follow the BCC deformation mechanism. Figure 3.26 is the temperature curve of pure martensitic steels under 20 kHz fatigue loading (R = -1). It's obvious that the similar temperature change doesn't occur in this steel (Huang et al., 2013). The specimen directly fractures about 55 °C. So, it can be assumed that the "sudden temperature increase" phenomenon is only related with the ferrite phase.

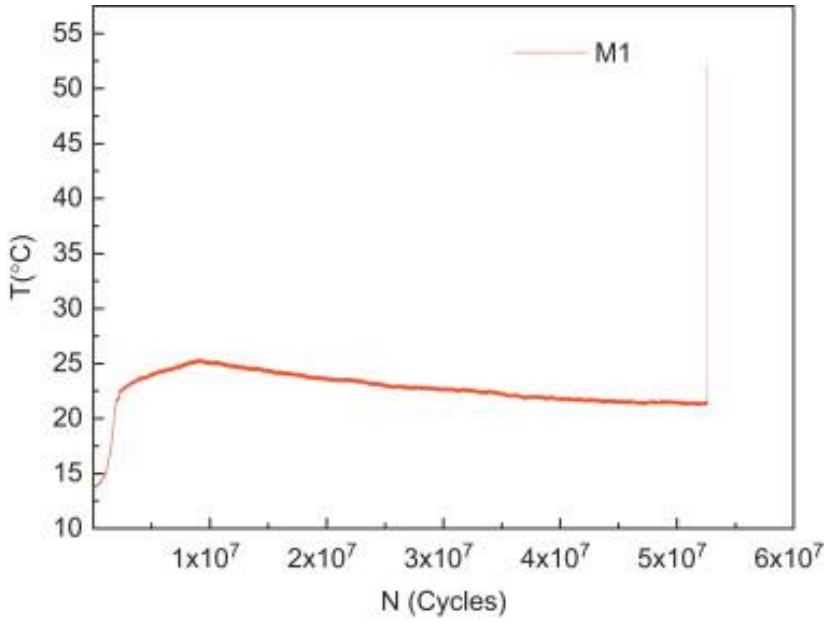

Figure 3.27 Temperature evolution of pure martensite steel (0.22 wt% carbon) under 20 kHz fatigue loading. (Huang et al., 2013)

So, it can be assumed that for ferrite-pearlite steels, as well as for ferrite–martensitic steels, the sudden temperature increase in self-heating tests is due to:

- the ferrite phase in which the transition from the thermal regime to the athermal regime occurs. In pure martensitic steels, the sudden temperature increase doesn't occur.
- the diffusion rate of carbon and nitrogen atoms in solid solution which starts and increases at temperature above 100 ℃.
- and the yield stress which decreases with the temperature.

2) Stage I (Stress range without the sudden temperature increase)

According to the above analyses, this non-linear ΔT-σ_a relation in Figure 3.14 belongs to the thermal regime ($< T_0$). In LCF and HCF, since the temperature is very small (about 10 °C), the tendency displays quasi-linearity. Scholars used to define the relation by one or two straight lines for convenience. They also are puzzled whether the temperature-stress relation is sure to be linearly dependent. Actually, the ΔT-σ_a relation for steels is indeed non-linear under 20 kHz loading.

Figure 3.22 collects statistics of the stabilization slopes at Period II (from 1×10^7 to 2.5×10^7 cycles) from several self-heating tests. Each data point respectively denotes the mean value and its standard deviation along Period II. It can be seen that stabilization slopes at Period II for all materials generally is rather small and can be negligible. It can

verify that specimen temperatures in self-heating tests have been completely stable till 2.5×10^7 cycles.

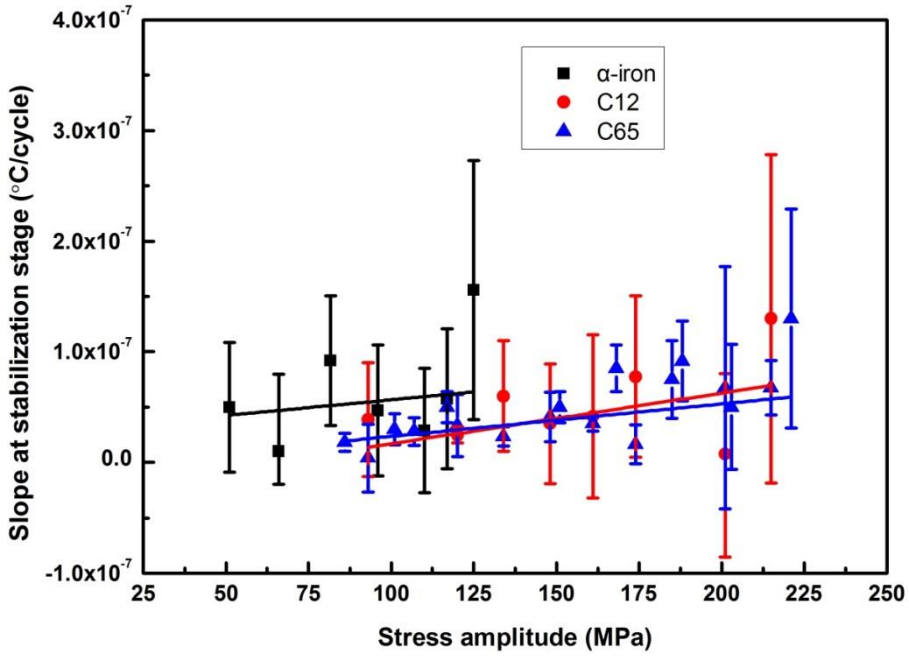

Figure 3.28 Slope of temperature increase at stabilization stage (Period II, 1×10^7 ~ 2.5×10^7 cycles) of three steels in self-heating tests.

The gap of fatigue limit between S-N curves and evaluation from self-heating tests in our work is possible to be caused by cumulative strain hardening in Period II of self-heating tests. Although the hardening at each cycle could be very low, cf. Figure 3.27 the cumulative strain hardening can be very large because of very high number of cycles. According to equation (3.1), the dominant contribution to σ^* arises from the lattice friction stress experienced by dislocations, the athermal component σ_G arises from the elastic interaction of the dislocations during glide and is usually related to the dislocation density ρ, as (Mughrabi et al., 1981):

$$\sigma_G = \alpha G b \sqrt{\rho} \tag{3.2}$$

Finally, the Taylor equation described the relationship between flow stress and dislocation density:

$$\sigma = \sigma_0 + \alpha G b \sqrt{\rho} \tag{3.3}$$

Where, σ_0 is the lattice friction stress, α dislocation strengthening constant, G the shear modulus, b the modulus of the Burgers vector. The equation (3.3) manifests that the increase of dislocations density during each interrupted test, especially the accumulation

of immobile dislocations density owing to dislocations pileup, would increase the saturated flow stress of materials. That is to say, the hardening in pre-strained specimens will raise the flow stress, compared to new virgin specimens.

3.3.2 Explanation about intrinsic dissipation tendency

From Figure 3.23, it's found that the intrinsic dissipation and the applied stress amplitude agree with the function $d_1 = ax^b$, in which *a* and *b* are two constants related to materials properties. We try to seek for an explanation to this relation from the existing theory.

According to the thermodynamic theory, in particular the Clausius-Duhem inequality, the intrinsic dissipation energy d_1 is the product of the total plastic energy minus the stored energy. As proposed by Chrysochoos (1989), d_1 is expressed as the following equation:

$$d_1 = \sigma\dot{\varepsilon}_P - X\dot{\alpha} - R\dot{p} \approx \beta\sigma\dot{\varepsilon}_P \ \ (\beta < 1) \tag{3.4}$$

where, (X, α) and (R, p) are the couples (thermodynamical force, state variable) associated with the kinematical and isotropic hardening, respectively. β is the Taylor-Quinney coefficient, representing the proportion of plastic energy to be dissipated. For steel materials in tensile tests, the value of β tends to be 0.5~0.8 (Chrysochoos et al., 1989; Knysh and Korkolis, 2015; Rittel et al., 2017). Along Period II, β can be considered as a constant value per cycle, since temperature is stabilized and the thermal and mechanical boundary conditions don't vary.

Furthermore, the relation between plastic strain rate and the stress amplitude is assumed to satisfy a Norton flow rule (Norton, 1929):

$$\dot{\varepsilon}_p = \left(\frac{\sigma}{K}\right)^n \tag{3.5}$$

with K and n two materials parameters. Therefore, combining the Equations (3.4) and (3.5), the intrinsic dissipation energy can be expressed as a power function of stress amplitude:

$$d_1 = C(\sigma)^m \tag{3.6}$$

where, C is related to the parameters K and β, and $m = n + 1$. The results in Figure 3.23 show that the power fitting is in good agreement with the above equation (3.6) and the fitted power exponents increase with carbon content.

3.3.3 Effect of ferrite/pearlite phase fraction

Pearlite phase fraction greatly affects the materials structure and properties, such as, mechanical properties (YS, UTS, et al.), fatigue strength, thermal conductivity (Table 3.3), dissipative behaviors and so on.

Fe_3C in pearlite phase is a bad conductor to transfer heat comparing with ferrite phase, so thermal conductivity would decrease with more pearlite fraction. With pearlite fraction increasing, micro-hardness of ferrite grains in α-iron, C12 and C65 are 179 HV, 197 HV and 243 HV, respectively.

Due to the increase of pearlite phase in three materials, mechanical properties in uniaxial tensile curves (Figure 3.7) improve greatly, especially the ultimate tensile stress. Fatigue limits at 2×10^9 cycles of these three materials (α-iron, C12 and C65) found in conventional S-N curves (Figure 3.27) are about 105 MPa, 190 MPa and 210 MPa, respectively.

The resistance to plastic flow increases with pearlite fraction. The minimum stress amplitudes which cause the sudden temperature elevation in Figure 3.11 also increase with carbon content. In Figure 3.14, the maximum stabilized temperature elevations ΔT in thermal regime of α-iron, C12 and C65 steel respectively lie around ~90 ℃, ~75 ℃ and ~60 ℃. The tendency of temperature ΔT may correspond to the tendency of transition temperature T_0. Consequently, T_0 is remarked to decrease with pearlite fraction. These temperature are mean temperature on the surface in the specimen center. It will be interesting to have the localized temperature only in ferrite grains.

Dissipative behaviors also depend upon the phase constituents. As for α-iron, C12 and C65 steels, since the hardness of pearlite phase is much higher than ferrite, dislocations preferentially glide in the soft ferrite phase. As listed in Table 3.5, micro-hardness of ferrite grains will increase with total carbon content. The higher hardness is not beneficial to dislocation movement in ferrite. Irrespective of the texture and grain size,

smaller ferrite phase fraction is the main reason why the dissipated energy of these three steels (α-iron, C12, C65) lowers respectively.

3.4 Conclusions

The three materials with different pearlite fraction, α-iron (0 %), C12 (1.1 %) and C65 (84 %), are studied to compare their thermal response and fatigue behavior in self-heating tests and fatigue tests.

1. Under 20 kHz fatigue loading, when the applied stress amplitude is enough high, specimens temperature could suddenly increase to hundreds of degrees, which mainly corresponds to the transition from thermal regime ($< T_0$) to athermal regime ($> T_0$).

-In athermal regime, a series of optical microscopic observations give the evidences to the temperature increase is caused by dislocations multiplication thanks to the enhanced mobility of screw dislocation from the temperature transition T_0, and micro-voids will be produced in bulk.

-In thermal regime, the tendency of ΔT-σ_a curves is non-linear for these three materials. The dissipated energy per cycle always displays the power relation with stress amplitude.

2. The cumulative hardening effect would cause the flow stress increase and temperature variation decrease.

3. More pearlite fraction in steels leads to lower thermal conductivity, and produces higher fatigue strength. Temperature elevation and dissipated energy decline with increasing the carbon content.

Chapter 4 Effect of stress amplitudes on damage and crack initiation mechanisms in gigacycle fatigue tests

In previous chapter, we have observed the experimental phenomena of sudden temperature increase at some certain stress amplitude, in α-iron and two C-Mn steels. We have proved the relevant mechanism about transition from thermal regime to athermal regime in BCC metals.

In this chapter, the applied stress amplitudes could be classified into high stress amplitudes and low/very low stress amplitudes, according to the temperature curves in fatigue tests whether they will experience the sudden temperature increase. α-iron and C12 steel are studied for the effect of different stress amplitudes (high, low, very low) on damage and crack initiation mechanisms in VHCF domain assisted by microscopic and fractographic observations. We will summarize and discuss the appearance of slips marks mainly on α-iron.

4.1 Experimental procedure

In this chapter, new specimens will be subjected to a given stress amplitude until fracture or a very high number of cycles (typically 2×10^9 cycles or 3×10^9 cycles). No cooling air is applied around specimens during tests. Optical microscope camera and the infrared camera are placed on two sides of flat specimen, as shown in Figure 2.8. The optical microscope camera and infrared camera are used in situ to record the microscopic changes and temperature change during tests. The details about machines and specimen preparation have been introduced in chapter 2.

In this part, both optical microscopic camera and desk type optical microscope are used in morphology observations. In order to distinguish the optical microscope camera (in Figure 2.8) and the common desk type optical microscope, it should be aware that photos taken by the optical microscope camera present a brown-yellow background, due to the warm light source. Oppositely, the desk type optical microscope doesn't have the apparent background color with a cold white light source.

4.2 Results

Due to the presence of cumulative strain hardening, the same experimental phenomena, e.g. the sudden temperature increase to hundreds of degrees, will occur from different stress amplitude in self-heating and fatigue tests. According to the characteristics of temperature curves and the experimental phenomena, we sort the applied stress amplitudes into three groups from a qualitative perspective:

- ✧ The sudden temperature increase will occur. ⇒ **At high stress amplitude**s
- ✧ The sudden temperature increase will not occur, including two situations:
  - PSBs will appear. ⇒ **At low stress amplitudes**
  - PSBs will not appear. ⇒ **At very low stress amplitudes**

4.2.1 α-iron

- ➢ At high stress amplitudes (σ_a > 105 MPa)

New specimens of α-iron are subjected to the stress amplitude while recording the temperature field as well as the microstructure evolution by optical microscope camera as previously described in section 3.2.1. The fatigue tests will stop either fracture or stopping the fatigue machine at very high cycles (2×10^9 cycles or 3×10^9 cycles).

Figure 4.1, Figure 4.2 and Figure 3.19 are three groups of temperature and PSBs evolutions of α-iron recorded by optical microscope camera and infrared camera, at 113 MPa, 107 MPa and 106 MPa, respectively. The tendency of these three groups is almost the same, except the cycle of sudden temperature increase. So we choose one as an example to elaborate.

In Figure 4.1, specimen temperature increases and reaches the stabilization until the sudden temperature elevation happens at 1.4×10^7 cycles. At 2.7×10^6 cycles (image ①), the trace of PSBs emergence (marked by red arrow) is recognized on the left of image ①. So this PSBs site is moved to the center of optical microscope camera view field. From the beginning of fatigue test, the surface doesn't show apparent changes. Until 1.0×10^7 cycles (image ②), the PSBs marks have appeared obviously in several grains. The initial slip bands in one or two grains have evolved crossing from two directions, but the surrounding grains remain undamaged. The root zone of this sudden temperature increase (image ③④⑤) corresponds to the slips appear in the grains. After the specimen temperature to hundreds of degrees (from 1.364×10^7 cycles, image ⑤), PSBs saturated but not fracture. From this moment, the specimen color changes owing to the oxidation, as shown in Figure 3.13.

Besides, early slip markings always appear at about 45 degree angle to the loading direction, aggregating in one or two grains as clusters. After the beginning of the sudden temperature increase, the isolated slips markings propagate straightly into grains. This kind of intragranular slips is also inclined at 45 degree angle to loading direction.

Photos in Figure 4.1 clearly present the surface before temperature saturation. In Figure 4.2 and Figure 3.19, at the moment the sudden temperature rise to hundreds of degrees, the whole camera field is full of PSBs and the surface PSBs number quickly saturates. It is certain that multiplication of PSBs occurs very quickly and evolves massively on surface, exactly at the same time the specimen temperature changes.

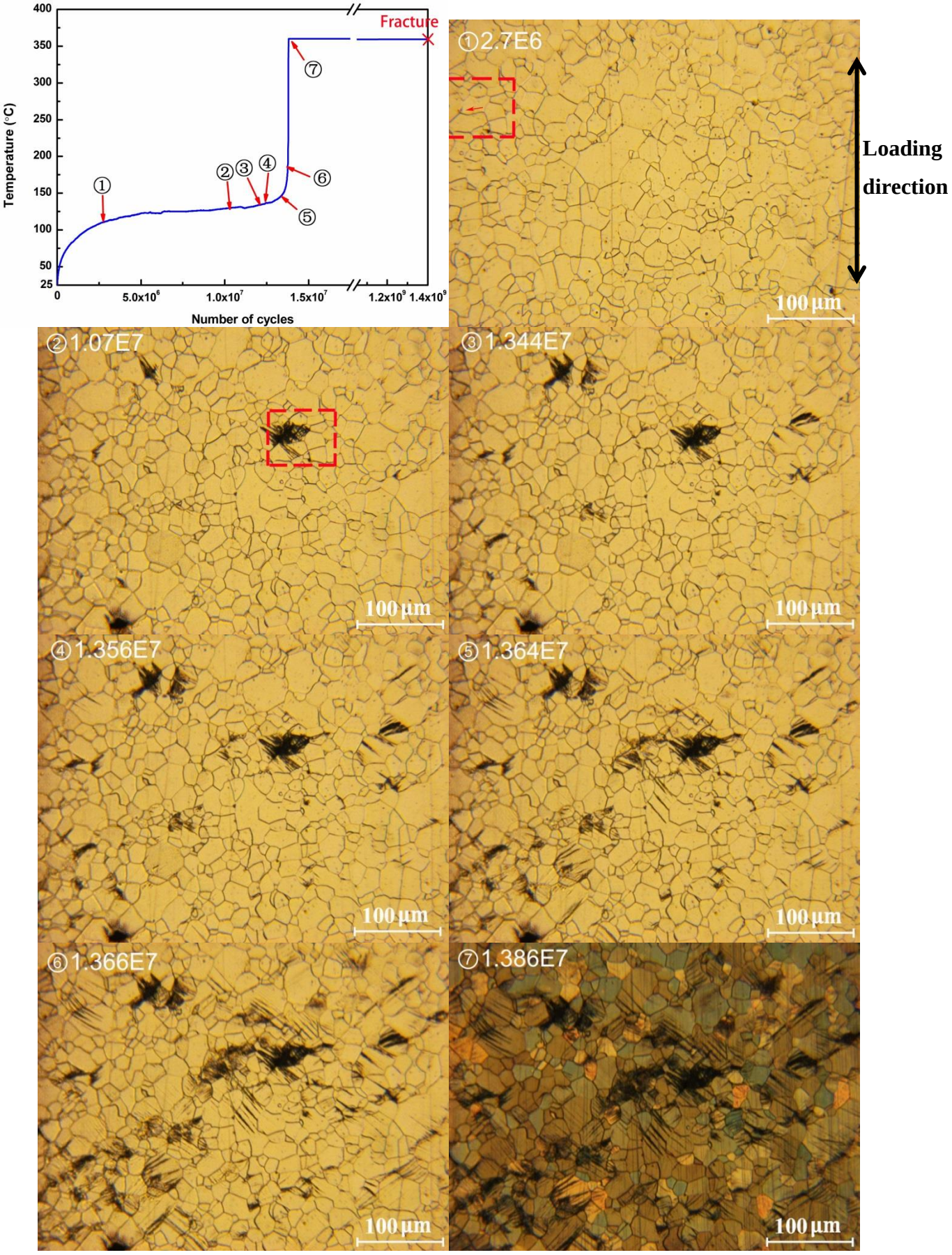

Figure 4.1 Temperature evolution and the corresponding PSBs evolution of α-iron at 113 MPa. From ① to ②, view of microscope is shifted left for recording the site of initial PSBs.

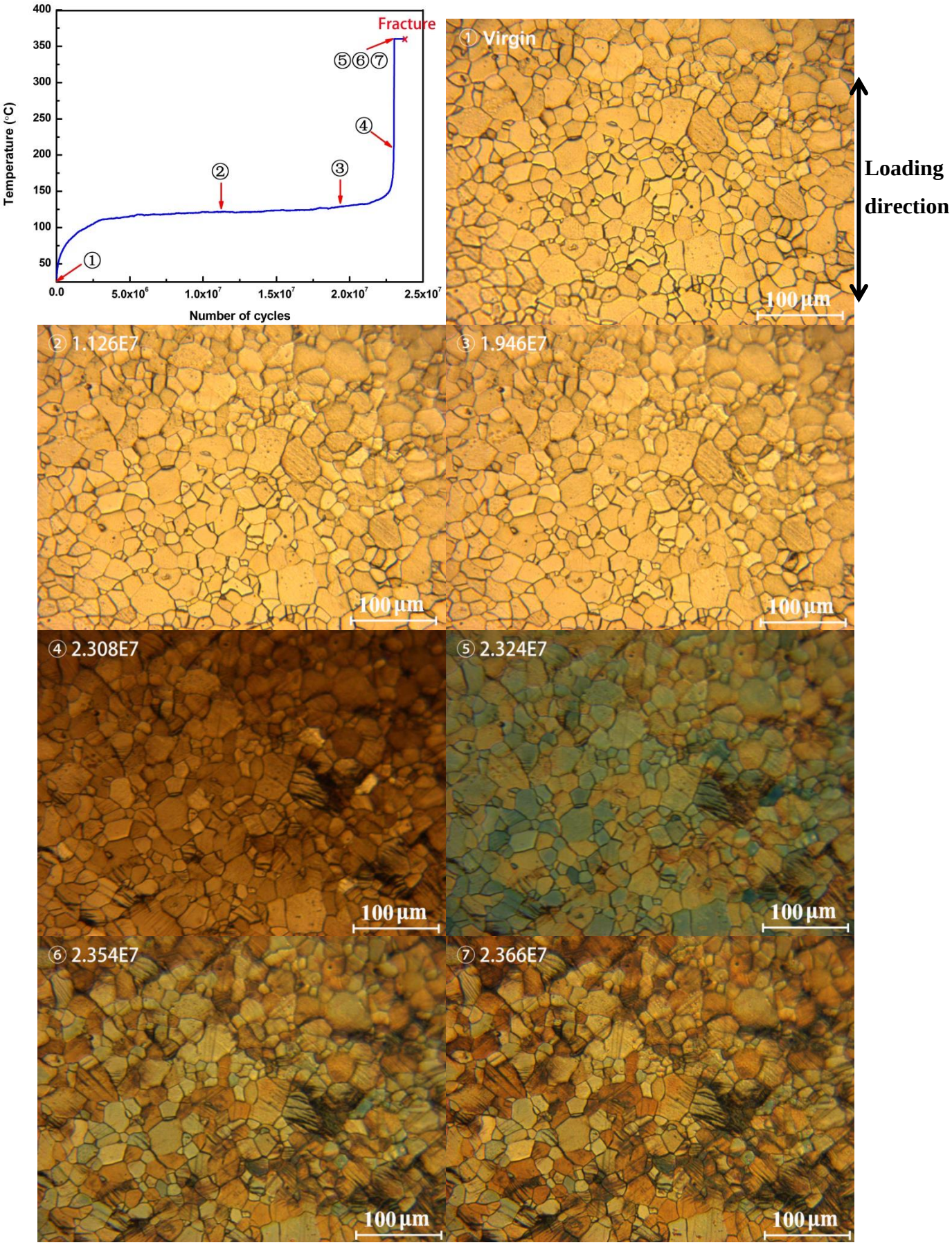

Figure 4.2 Temperature evolution and the corresponding PSBs evolution of α-iron at 107 MPa.

And observations in self-heating tests (Figure 3.22-3.24) has the same phenomenon after the final stress amplitude at 122 MPa. On the basis of these optical observations and our discussion about BCC temperature-dependent mechanism, we can verify that the sudden temperature rise to hundreds of degrees under high frequency loading corresponds to the transition from thermal regime ($< T_0$) to athermal regime ($> T_0$). Screw dislocations can slip, resulting in an accelerated of PSBs fromation on surface.

The cycles in which the sudden temperature increase happens are exactly 1.4×10^7 cycles at 113 MPa (in Figure 4.1), 2.3×10^7 cycles at 107 MPa (in Figure 4.2), 9×10^7 cycles at 106 MPa (in Figure 3.25). The higher stress amplitude corresponds to the earlier cycles to activate athermal regime ($> T_0$).

- At low stress amplitudes ($\sigma_a \sim 105$ MPa)

At low stress amplitude, the sudden temperature increase will not appear any more. The temperature will stabilize below 100 ℃. Figure 4.3 is the temperature and microstructure evolution of α-iron at 105 MPa. Specimen temperature always remains 93 ℃ even up to 3×10^9 cycles, completely different from behaviors at high stress amplitudes. In addition, PSBs are found only in few adjacent grains, and most grains have no slip markings at all, even after 3×10^9 cycles.

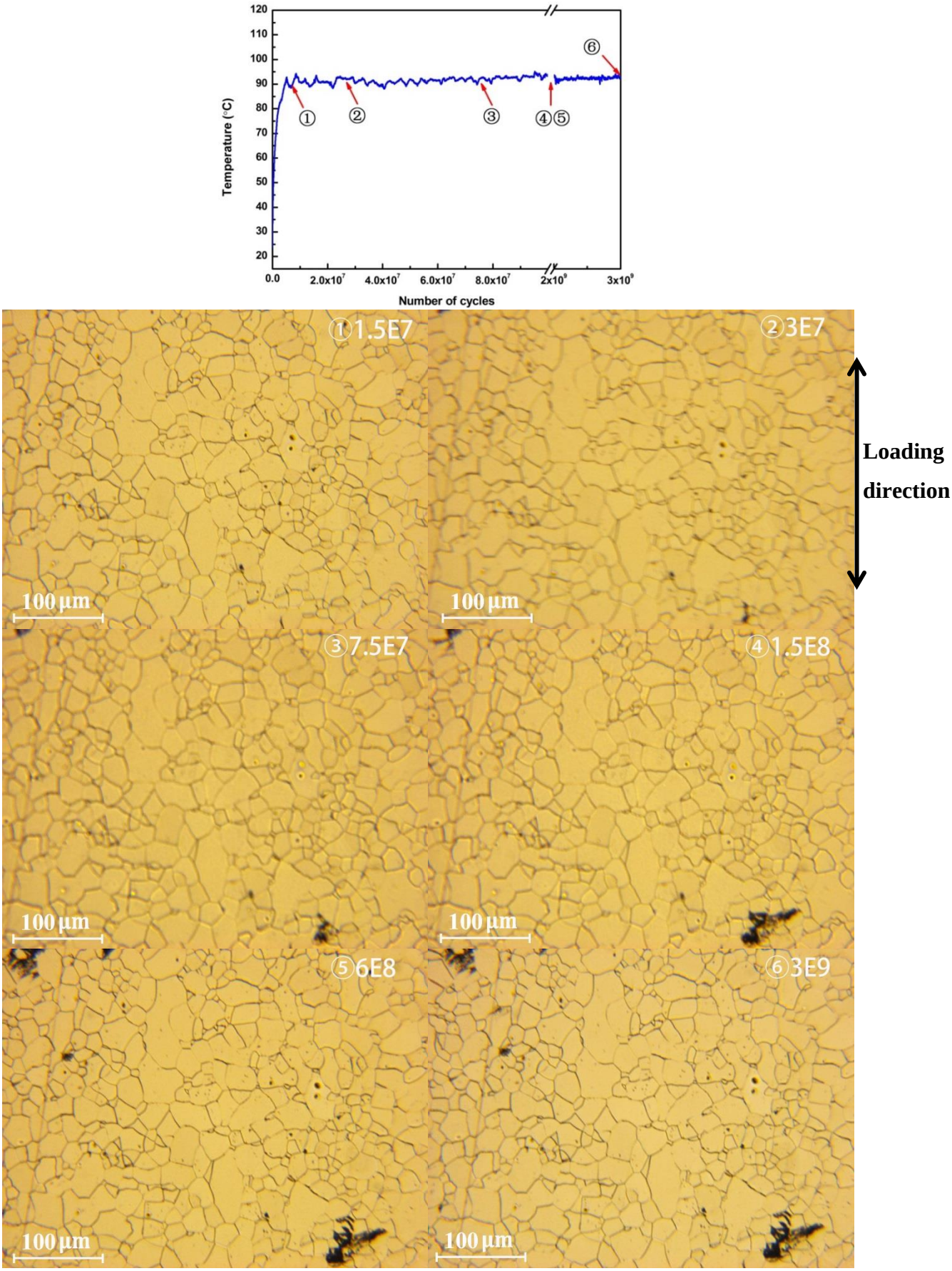

Figure 4.3 Temperature evolution and corresponding PSBs evolution of α-iron at 105 MPa.

Through the photos in Figure 4.3, it's sure that PSBs can appear in the case of without the sudden temperature increase. Surface grains are easier to deform than interior grains, due to the presence of interfacial energy. PSBs threshold is also related to grain information, such as grain orientation, grain arrangement and so on.

We collect all the initial cycle of recognizable PSBs appearance on α-iron surface. Figure 4.4 compares the cycles of PSBs appearance and specimen failure. The same number means the results from the same specimen. The data point without arrows represents the fracture of specimens at specific cycles, whereas arrows mean run-out. Therein, for the points 2/2' and 3/3', they are probably caused by that microscopic camera view cann't cover horizontally the whole specimen surface, their initial PSBs appearances are not localized in the microscpic view field. The fitted line of PSBs appearance indicates that the higher stress amplitude is, the earlier PSBs would tend to appear in the whole fatigue life. In most situations, the initial PSB marking can be found before ~1×10^7 cycles, that's to say, PSB has been appeared before specimen temperature stabilization (in Period I as marked in Figure 3.10). Whereas, expansion of these PSBs into adjacent grains requires rather long time, far over 10^7 cycles.

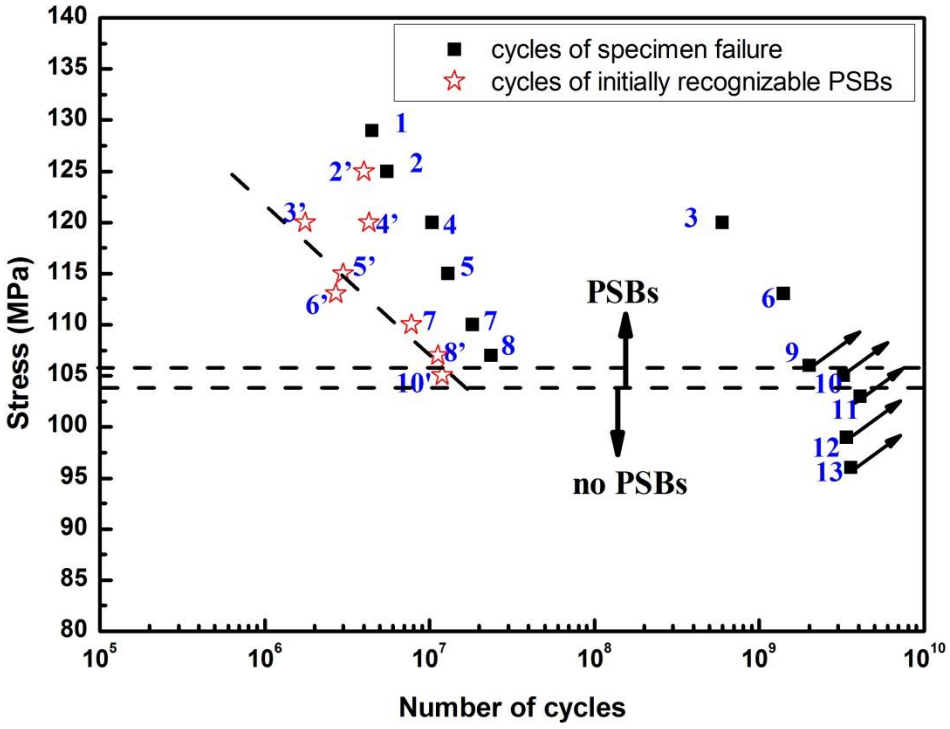

Figure 4.4 The cycles of initial appearance of PSBs observed by optical microscope camera for α-iron. Details can be found in annex.

- At very low stress amplitude (σ_a < 103 MPa)

At lower stress amplitude, no PSBs will be going to appear at all on surface. Besides no PSBs on the surface, no micro-voids are observed on cross-section. One test at a stress amplitude of 80 MPa and an another one at 103 MPa were cut transversely and observed in SEM, and don't show any subsurface damage. However, another dislocation structure emerges on surface of iron. Figure 4.5 and Figure 4.6 are SEM photos of α-iron at 103 MPa and 99 MPa above 3×10^9 cycles. In some isolated grains, they seem to be small strips or knots. Some other grains still appear smooth. In order to contrast, surface of one new α-iron specimen just after polishing without fatigue cycles is displayed in Figure 4.7.

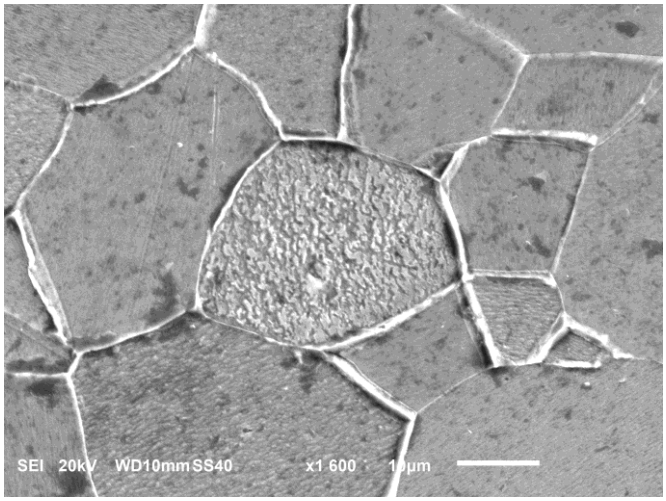

Figure 4.5 SEM photo of α-iron at 103 MPa after 4×10^9 cycles.

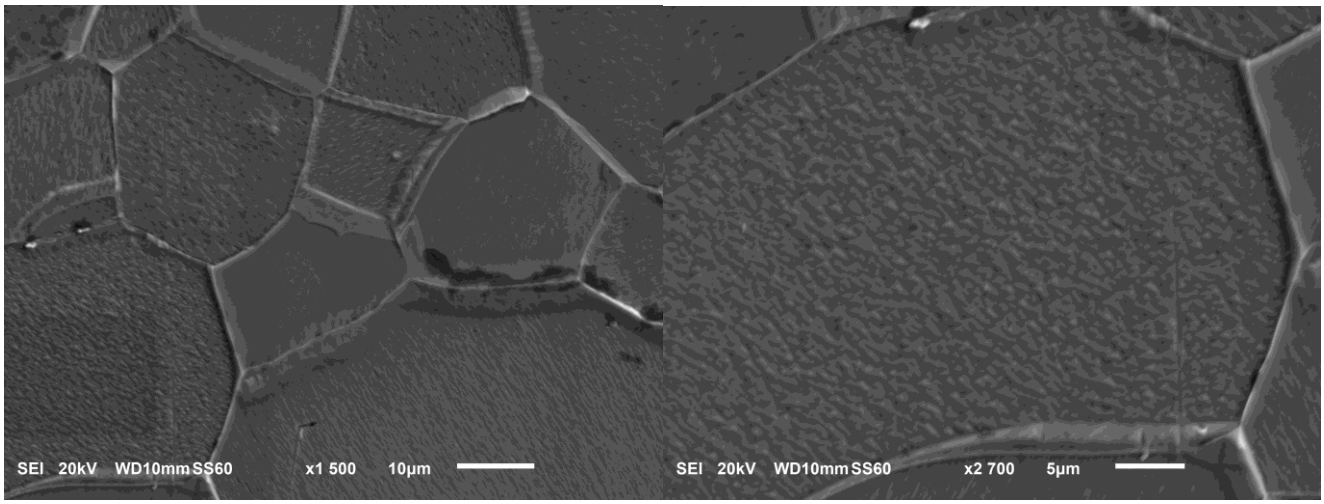

Figure 4.6 SEM photos of α-iron at 99 MPa after 3.3×10^9 cycles.

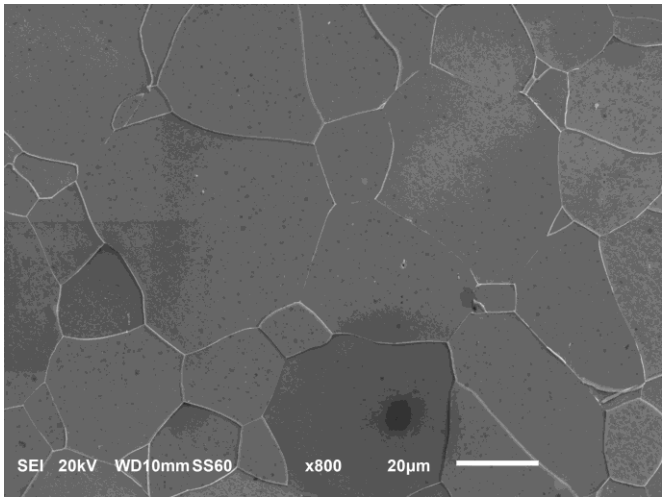

Figure 4.7 SEM photo of α-iron surface never subjected to any stress amplitude.

Comparing with the virgin specimen surface in Figure 4.7, it can be sure that the surface roughness in Figure 4.5 and Figure 4.6 is the result of deformation under stress.

4.2.2 Carbon steel C12

Since carbon steels contain a certain amount of black pearlite phase, it becomes more difficult to observe the surface damage by in-situ optical microscope, comparing with pure iron. Thus, only C12 will be discussed in this part.

- At high stress amplitude

In Figure 4.8, the temperature evolution of C12 steels at 216 MPa is displayed and this specimen doesn't fracture even up to 3×10^9 cycles. And another two photos are the strain localization region on C12 surface after 3×10^9 cycles taken by SEM and desk type optical microscope. It's found that carbon steel C12, different from pure iron, will not produce large amount of PSBs after specimen temperature to hundreds of degrees. PSBs cannot be observed on the whole surface, merely in some limited regions. This may be to be related with the elongated MnS inclusions (black strips in Figure 3.1) and more pearlite content. Similarly, C12 specimen colour also have changed after temperature increase. The grains in the photo (Figure 4.8c) are blue.

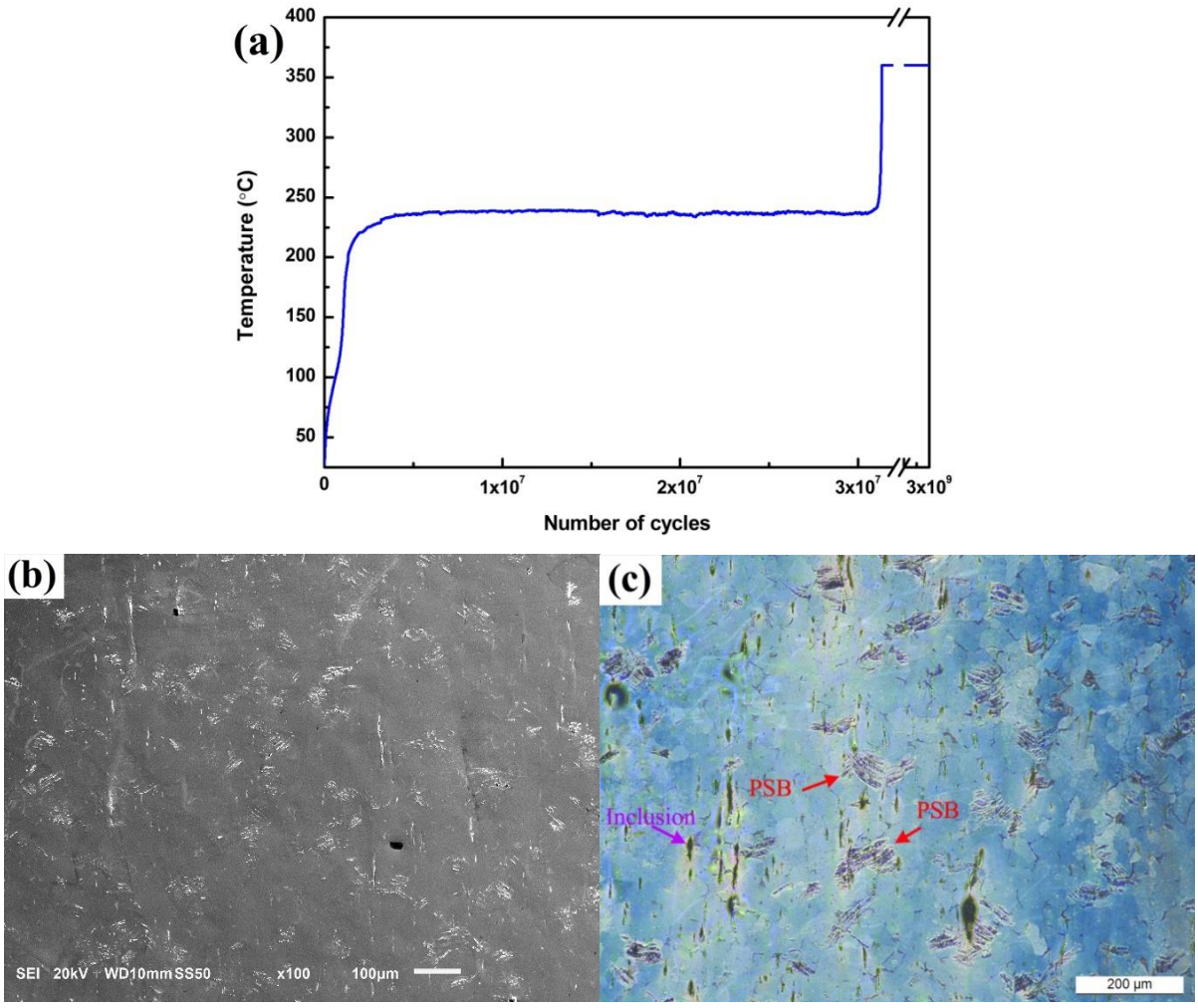

Figure 4.8 (a) Temperature evolution of C12 steel at 216 MPa. Specimen surface after 3×10^9 cycles taken (b) by SEM and (c) by desk type optical microscope.

Dislocations gliding would be hindered by MnS precipitations as well as pearlite phase. Thus, PSBsnumber after the sudden temperature increase is focused on more restricted areas than α-iron.

Photos in Figure 4.9 present the PSBs evolution of C12 steel at 194 MPa. The surface is only treated by electrolytic polishing without etching, since pearlite phase and precipitations on surface would seriously affect brightness of photography, and I cannot see clearly the trace of slip marks. In photo ② of Figure 4.9, the slip marks appear in the vicinity of inclusions from about 1.2×10^7 cycles. Due to the sudden elevation of specimen temperature after some cycles, the specimen color caused by oxidation becomes dark brown and it turns difficult to continue recording the PSBs by optical microscope camera. And the dark vision in microscope cannot offer some

useful information. Correpondingly, Figure 4.10 is the slip marks on C12 surface after 194 MPa observed by desk type optical camera.

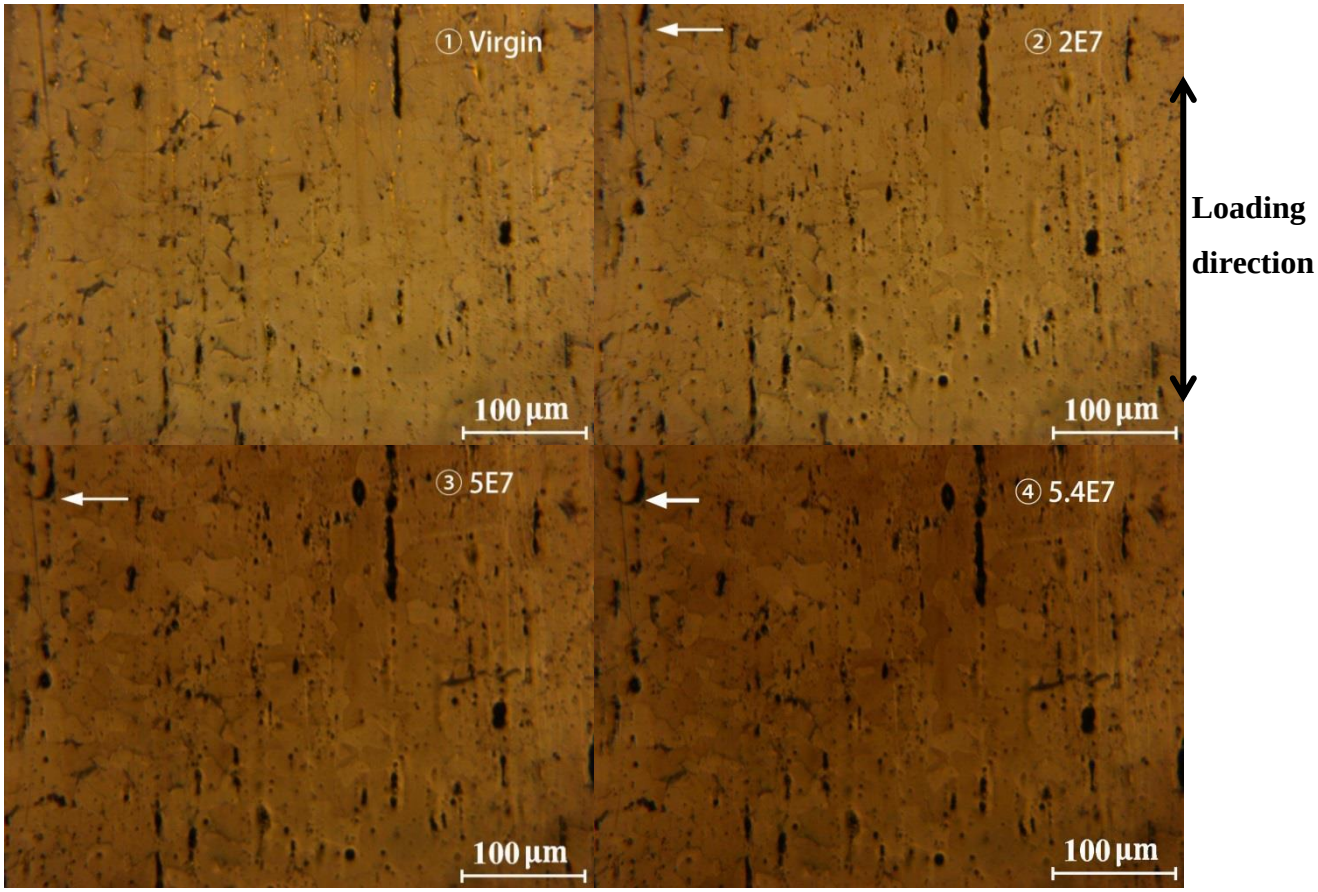

Figure 4.9 Slip marks on C12 steel surface at 194 MPa observed by optical microscope camera.

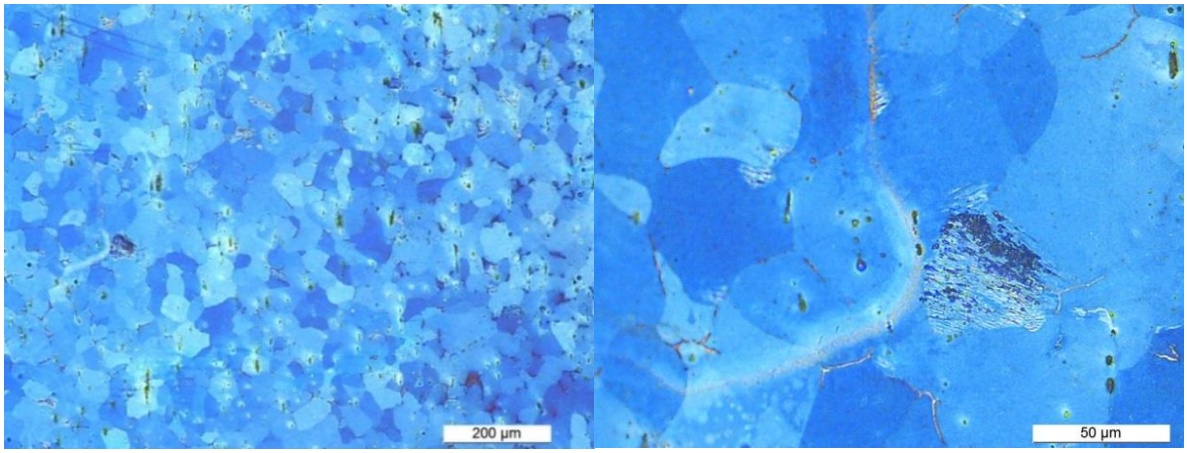

Figure 4.10 Surface of C12 steel at 194 MPa after 3×10^9 cycles, observed by desk type optical microscope.

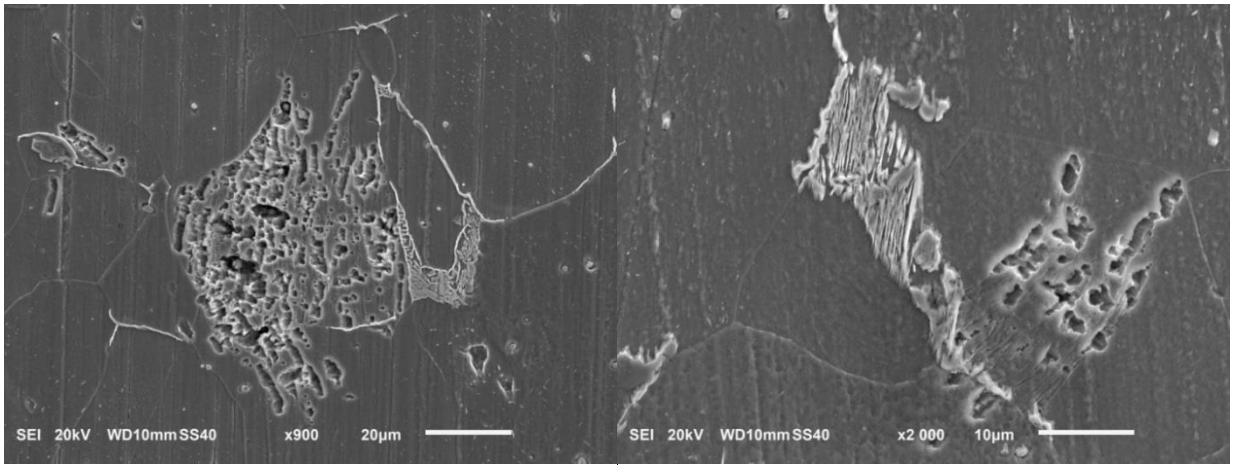

Figure 4.11 SEM photos of C12 steel at 190 MPa after 2×10^9 cycles.

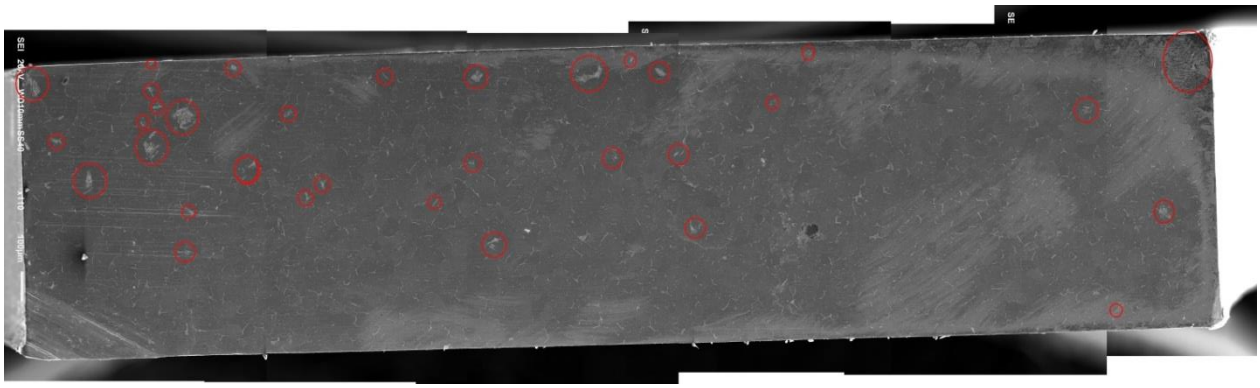

Figure 4.12 SEM photo on the whole cross section of C12 at 190 MPa to 2×10^9 cycles.

Figure 4.11 are micro-voids found on cross-section of C12 after 2×10^9 cycles at 190 MPa after cutting from the centre. The whole cross-section is displayed in Figure 4.12. Under 190 MPa, this kind of visible deformation can be found in some grains corresponding to about 2% of the total grains number on the whole section. Unfortunately, for this specimen, it can't be possible to observe the surface damage, since it is not polished electrolytically.

- At low stress amplitude

In the fractography of C12 at 175 MPa and 130 MPa, we observe neither micro-voids in matrix nor PSBs on surface.

We summrize the observed phenomena of C12 in Figure 4.13. Although the datapoints are not sufficient to analyse furtherly, maybe it's helpful to understand its mechanism. Point 1-5 offer no information about PSBs, on account that these five

specimens are tested after mechanical polishing, or electrical polishing are not good enough.

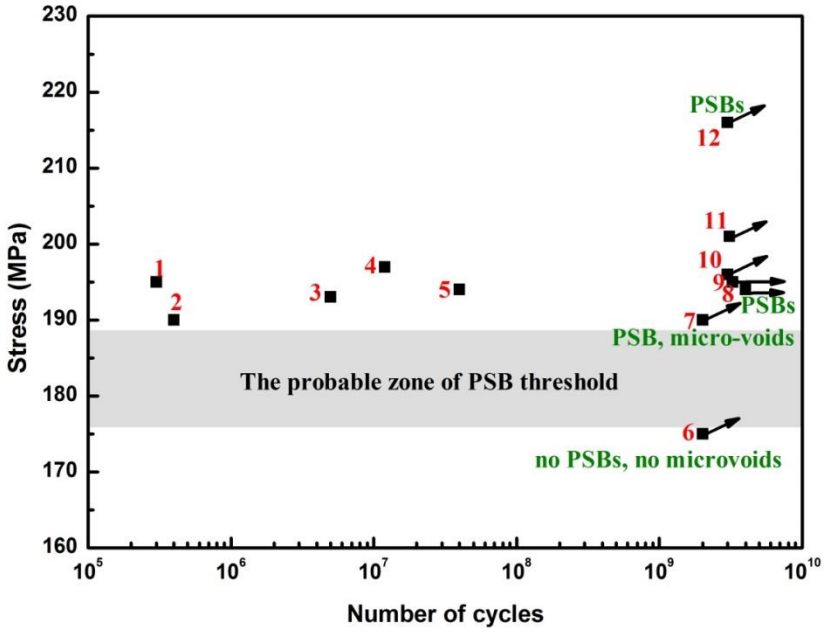

Figure 4.13 The observed structures of C12 steel summarized in S-N curve. Details can be found in annex.

4.3 Discussion

From Figure 4.4 (α-iron) and Figure 4.13 (C12), it seems possible to schematize the behaviors in VHCF domain (tested at high frequency) for the ferrite/pearlite steels (Figure 4.14).

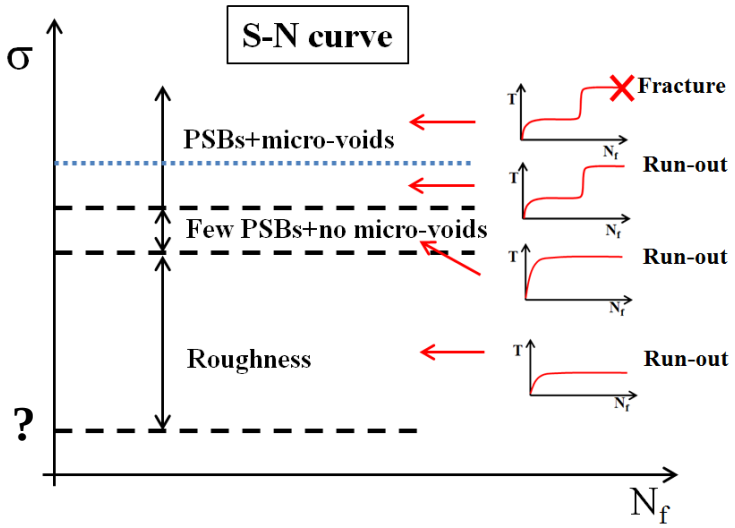

Figure 4.14 Summary of temperature evolution and microstructural changes.

These figures show the relation between thermal response and corresponding microstructures for the BCC ferrite/pearlite steels tested at high frequency until 10^9 cycles without cooling. The following points can be summarized:

Point 1: an abnormal sudden temperature increase occurs when the specimen temperature approaches ~100 °C for α-iron (with 0.008% of carbon) and C12 steel and 75 °C for C65;
Point 2: a PSB threshold of about 103~105 MPa for the studied polycrystalline α-iron, corresponding to a shear resolved stress of ~ 63 MPa;
Point 3: for a stress amplitude below 100 MPa (α-iron), we observe no occurrence of PSB are observed, but instead, a surface roughness in some grains.

- Point 1

The point 1 has been discussed previously. So, it can be assumed that for ferrite-pearlite steels, as for ferrite-martensitic steels, the sudden temperature increase in self-heating tests is due to:

-the ferrite phase in which the transition from the thermal regime to the athermal regime occurs. In pure martensitic steels, the sudden temperature increase doesn't occur.
-the diffusion rate of carbon and nitrogen atoms in solid solution which starts and increases at temperature above 100 ℃. For the C65 steel, the sudden temperature increase begins at a lower temperature. It will be interesting to know the temperature in ferrite grains. Probably, the temperature in the ferrite grains is also around 100 ℃, but with the numberous pearlite grains (in which the temperature is lower), the mean temperature globally is lower than 100 ℃.
-and the yield stress which decreases with the temperature.

- Point 2

A schematic multistage fatigue life diagram (Mughrabi, 2006; Mughrabi and Stanzl-Tschegg, 2007) is proposed for the copper reported in Figure 4.15 with a conventional fatigue HCF limit and a lower VHCF limit at much higher number of cycles N_f. Below the stress for the development of PSB, the damage will be due to the accumulation of slightly irreversible random slip.

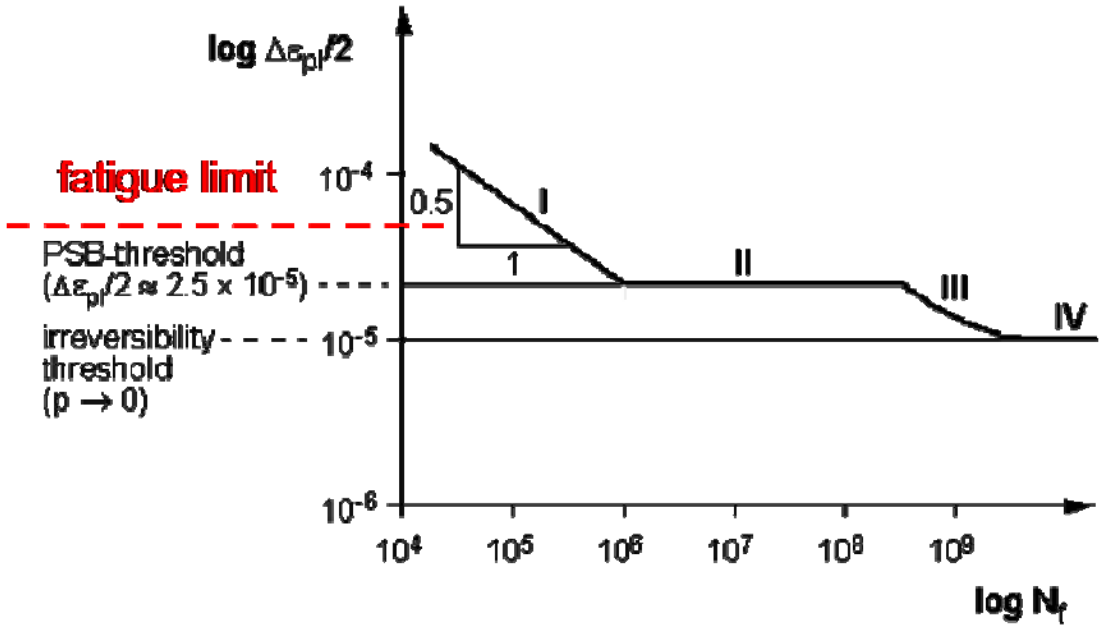

Figure 4.15 Schematic multistage fatigue life diagram for type I materials (copper). (Mughrabi and Stanzl-Tschegg, 2007)

For the polycrystal α-iron of this study with 0.008% carbon tested at high frequency, the shear resolved shear stress lies around 60 MPa (Point 2). H. Mughrabi for an α-iron single crystal with 30 ppm of carbon reported a shear stress threshold for PSB of 49 MPa (Mughrabi, 1979), not so far of our value for a polycrystal with a little more carbon and tested at high frequency. For the stress amplitudes just above the PSB threshold, the fatigue cracks initiate at the sites of emerging PSBs at the surface, where the damage is due to the rapid formation of extrusions and intrusions and the increase of surface roughness. For stress amplitudes below the PSB threshold, there would be no cyclic strain localization in PSBs but only a gradual surface roughening. From H. Mughrabi (2006), "*When a critical state of roughness is reached, some valleys in the surface roughness profile act as sufficiently strong raisers to the extent that the local stress at such site can exceed the PSB threshold value.*" This would then lead to the formation of an "embryonic" PSB as indicated in Figure 3.43 a-d.

- Point 3

As illustrated in Figure 1.26, PSBs formation requires experiencing three stages under stress amplitude: surface roughness, the first slip appearance and persistence slips marks. The existing deformation type has accommodated the present plastic

deformation at such stress amplitude level. It indicates that surface roughness could be reserved to show, on account that plastic strain is not sufficient to produce slip bands.

In the cyclic stress-strain curves under low frequency loading (Shih et al., 2009) in Figure 1.19, α-iron will form the dislocation structure termed "loop patches", on the condition of plastic strain amplitude not sufficient to generate dislocation walls/ladders structure, i.e. slip bands. Therefore, it's assumed that surface roughening is possible to be "loop patches", which consist of bundles of dislocation dipoles dominated by dislocations.

This surface roughness for stresses below the PSBs threshold has been evidenced in copper polycrystals (Weidner et al., 2010). The present study on α-iron and C12 show that this damage sequence can be proposed for BCC steels.

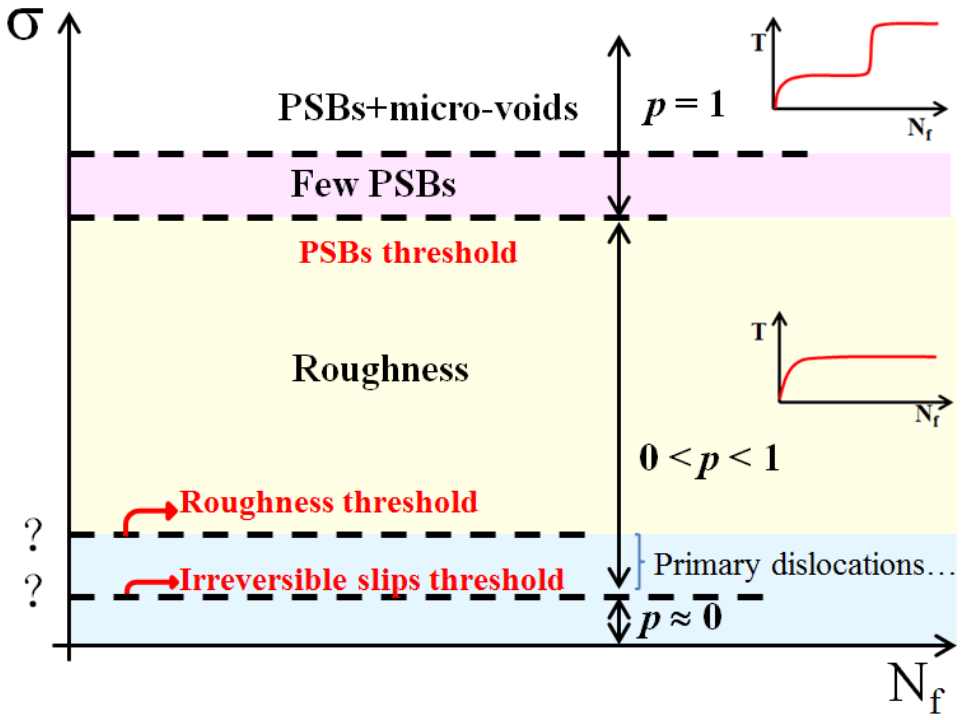

Figure 4.16 Schematic illstruction of relation between thermal behavior and microstructure.

From H. Mughrabi (Mughrabi, 2013a), "*fatigue damage of ductile crystalline materials is intimately related to some kind of slip irreversibility leading to unreversed slips steps at the surface. The slip irreversibility p is defined as the fraction of microstructurally irreversible cumulative plastic strain*". This

irreversibility can emanate from different sources (Mughrabi, 2013b). For the α-iron polycrystals, two sources are identified: surface roughening and asymmetry of slip planes in tension and compression of BCC metals leading to incompatible shape changes of neighbouring grains and intergranular cracking.

In order to have a better understanding of relation between thermal behavior and microstructures at different stress amplitudes, a schematic picture is summarized with in the irreversibility factor *p* in Figure 4.16. Below the strain amplitude to surface roughness, some irreversible slips: gliding primary screw dislocations, debris loops and a few secondary dislocations can be found in TEM photo. (Shih et al., 2009). Therefore, probably-existed irreversisible slips threshold is considered to stay below roughness threshold. Surface roughness is the aggregation structure of irreversible dislocations. With increasing the strain amplitude, the number of grains forming this kind of irreversible structure become more and more, the corresponding irreversibility increases between 0 and 1. Until local stress in some grains beyond the threshold of PSB, it begins to form PSBs on surface. This similar phenomenon is analogue to Figure 4.3, few PSBs would occur without the sudden temperature increase. Once the sudden temperature increase happens, PSBs saturation on surface and micro-voids in matrix would form consequently.

4.4 Conclusions

The α-iron and C12, are studied to investigate the effect of stress amplitude on fatigue initiation mechanism in fatigue tests.

1. At high stress amplitude, it will produce many PSBs on surface, and micro-voids in matrix.

At low stress amplitude, there are only few PSBs in rare few grains.

At very low stress amplitude, it will not produce any PSBs, and grain surfaces become rough.

2. The cycles of first recognizable PSBs appearance consume a lower fraction of fatigue life at higher loading amplitude. PSBs threshold lie below fatigue limit.

Chapter 5 Effect of interstitial atoms content on thermal response of C-Mn steels in self-heating tests

In last chapter, we find that for the C12 steel, two distinct temperature increases would appear before 1×10^7 cycles, over which the specimen temperature is stabilized (Figure 3.27). But the related mechanism still remains unknown.

In this chapter, thermal behaviors of two C-Mn steels (A42, A48) with different interstitial atoms content are compared. The A48 steel is the one with more interstitial atoms which is very sensitive to DSA. The DSA phenomenon makes its fatigue strength and thermal response different from A42 steel which is less sensitive to DSA. Furthermore, we adjust the interstitial atoms content in A48 steel by thermal treatment, since tempering treatment at 600 °C will gradually precipitate nitrides from the crystal lattice.

We mainly deal with three aspects: (1) effect of tempering on microstructure and properties of A48, (2) the reason why the secondary temperature increase appears in the A48 steel (3) How to explain the temperature changes in self-heating tests.

5.1 Materials and preparations

5.1.1 Composition and microstructure

The materials studied in this chapter are two carbon-manganese steels of AFNOR (French standard) NFA 36205 grade A42 and A48, which are received as 40 mm thick plates. Their chemical compositions are listed in Table 5.1. The A42 grade material is a fully-killed steel containing aluminium content (0.045%), while the A48 grade material is a silicon semi-killed steel containing a very low aluminium content (0.004%).

Table 5.1 Mass percentage (in wt%) of chemical elements.

	A42	**A48**
C	0.140	0.198
S	0.0057	0.012
P	0.016	0.0104
Si	0.225	0.207
Mn	0.989	0.769
Ni	0.024	0.135
Cr	0.021	0.095
Mo	0.002	0.025
Al	0.045	0.004
N	0.0082	0.0083
O	0.0006	0.0049

A42 and A48 plates are obtained after a prior normalization thermal treatment including austenitizing at 870 ℃ and then air cooling. Generally, during the normalization heat treatment, the majority of carbon atoms are used in formation of cementite (Fe_3C) in pearlite phase.

As to the difference of element contents in A42 and A48 in Table 5.1, aluminium content in A42 steel is almost 10 times more than A48 steel. Aluminium atoms in steel usually tend to combine with nitrogen atoms to form stable aluminium nitride (AlN) during cooling from the austenitic domain. In A48 steel, aluminium content is too low to trap all nitrogen atoms, such that a large amount of nitrogen atoms exist freely in the ferrite lattice. The significant difference between these two steels is the remaining free nitrogen atoms content in the lattice.

Optical microscopic structure of normalized A42 and A48 are shown in Figure 5.1, The white grains are ferrite and the dark are pearlite. Lamellar cementite structure can be easy to observe at high magnification.

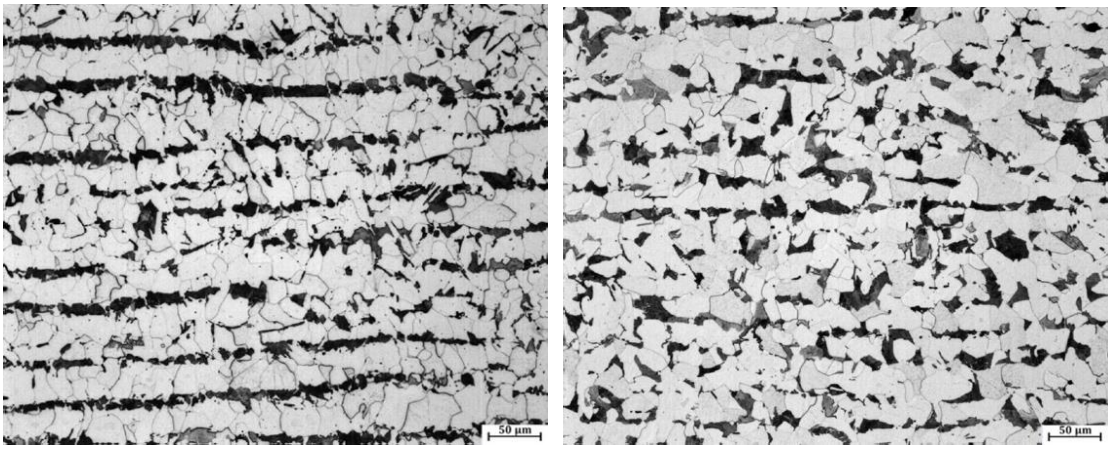

Figure 5.1 Microstructure of (left)A42, (right)A48. (Huang, 2010)

5.1.2 Characterization of the dynamic strain aging effect

The uniaxial tension curves of A48 at different temperatures are shown in Figure 5.2. In these curves, the jerky flow (serrations on the curves) begins to appear between 100 °C ~ 250 °C. To compare these two materials (A42 and A48), the strain rate coefficient $S = \frac{\partial \sigma}{\partial \ln \dot{\varepsilon}}$ is measured from 20 °C to 300 °C. Correspondingly, in Figure 5.3, the strain rate sensitivity coefficient of A48 becomes negative in the temperature range of 110 °C ~ 220 °C. Hence it proves that 110 °C ~ 220 °C is the thermal-activated temperature of dynamic strain aging in A48. Due to the higher interstitial nitrogen content for the A48 steel, its sensitivity to DSA is more remarkable than that in A42 steel.

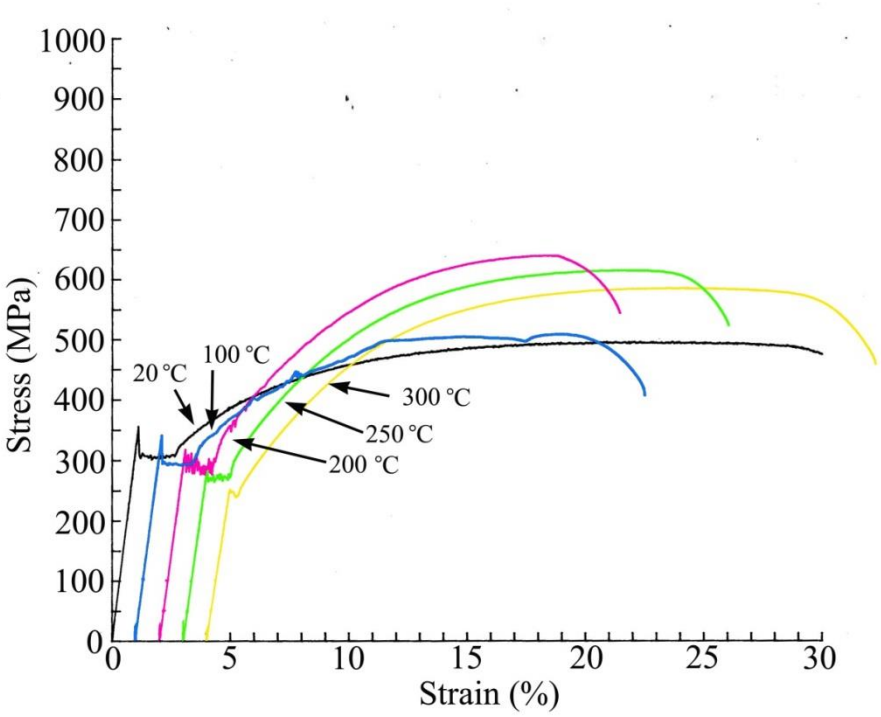

Figure 5.2 Uniaxial tension curve of A48 at different temperatures.

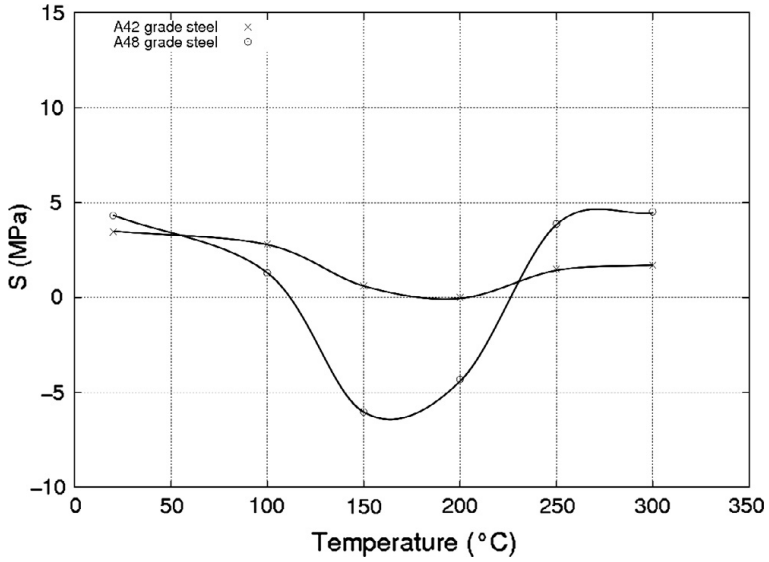

Figure 5.3 Strain rate sensitivity coefficient versus temperature for A48 steel and A42 steel. (Moreno, 1998)

Figure 5.4 is the internal friction spectra of A42 and A48. The internal friction technique allows to evaluate the balance between carbon/nitrogen free atoms in the lattice and carbon/nitrogen atoms interacting with mobile dislocations. According to the previous results (Wagner et al., 2006), the internal friction tests have shown a

good correlation between the internal friction spectra and the sensitivity to DSA for the A48 and A42 steels.

It is well-acknowledged that Snoek Peak (SP, the peak in mechanical loss observed in the temperature range 0 ~ 100 ℃) is associated with interstitial solute atoms diffusion in the ferritic lattice. If the crystal is cycled through tension and compression corresponding to the jumps of these atoms in solid solution from one position to the others, there is an absorption of energy in mechanical loss spectra (Snoek, 1941; François et al., 2012). Snoek-Kê-Köster Peak (SKKP, 100~250 ℃), also termed Snoek-Köster peak and Cold Work peak, is produced by the interaction between interstitial atoms and dislocations. Plastic deformations, which maintain a balance between C/N atoms distributions bound in stable precipitations, trapped at dislocations, and left in solid solution under thermal equilibrium, enabled us to observe highly stable SKKP in mechanical loss experiments. (Petarra and Beshers, 1967; Weller, 1983; Kinra and Wolfenden, 1992; Magalas, 2006)

In Figure 5.4, A48 steel (curve 1) shows two apparent remarkable peaks in the -20 to 300 ℃ temperature range. The first peak which presents a maximum at about 20 ℃ can be associated with SP resulting from carbon and/or nitrogen redistribution between octahedral sites in the ferritic lattice. Due to complex interactions between nitrogen and manganese, the Snoek peak height is not directly proportional to C and N interstitial content in the lattice, as observed in pure iron. (Gladman and Barker, 1971) The second peak, observed in the 150 to 250 ℃ temperature range, and is due to the interaction between dislocations and interstitials such as carbon and/or nitrogen. The SKKP height is related to both the density of mobile dislocations and the interstitial content in the vicinity of dislocations. This classical interpretation of the internal friction spectrum in steels is confirmed by curve 2 which represents the internal friction variation measured on this A48 grade steel after 8% cold working and one month room temperature aging. In that case, an increase of SKKP with dislocation density is observed, associated with a corresponding SP decrease, in agreement with the classical balance of interstitial atoms between lattice and dislocations.

The internal friction spectrum measured on A42 (curve 3) reveals no peaks (neither SP nor SKKP) in agreement with the nitrogen content in the ferritic lattice.

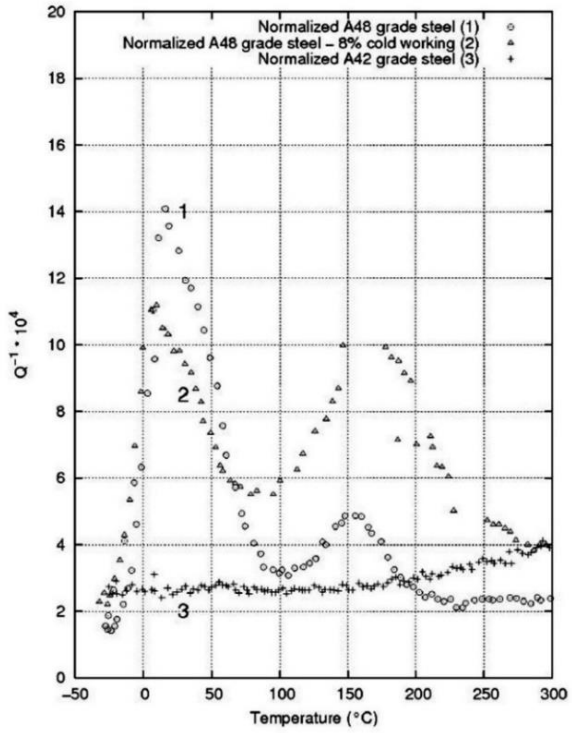

Figure 5.4 Internal friction spectra for normalized A42 and A48 steels. (Moreno, 1998)

5.1.3 Experimental procedure

The specimens of A42 and A48 used in fatigue tests are machined as Figure 5.3. Some A48 steel specimens are retreated at 600 ℃ during different times (1h30, 6h30, 26h30) in order to realize the atoms redistribution in the lattice. According to their retreatment duration, the heat-treated A48 steels are labelled as A48+1.5h, A48+6.5h, A48+26.5h, respectively. Before tests, mechanical polishing is necessary to remove the oxidation film on the surface.

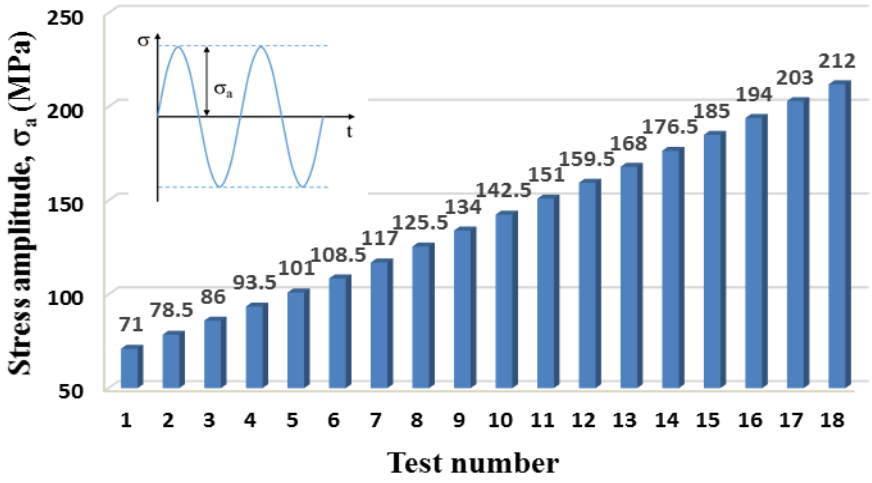

Figure 5.5 Successive fatigue loading step in self-heating tests (Each block consists of 2.5×10^7 cycles).

The experimental setups are shown in Figure 2.1. All the tests in this chapter are still carried out without cooling on the specimen. The temperature recordings are still obtained by IR camera from one side of the specimen which is covered with black paint. All the materials for self-heating tests are applied to the same loading history, as illustrated in Figure 5.5. These tests consist of a series of cyclic loadings for the same specimen with increasing the stress amplitude. At each stress amplitude, a fatigue test was carried out up to 2.5×10^7 cycles and then interrupted. After the specimen is cooled down to the room temperature, another loading step restarts.

5.2 Results

5.2.1 S-N curves

Figure 5.6 represents the conventional S-N curves of normalized A42 and A48 under 20 kHz loading. The results under cooling is refered from HUANG's thesis (2010). Under cooling, the fatigue limits at 2×10^9 cycles of A42 and A48 are 210 MPa and 245 MPa. Without cooling, the fatigue limit at 2×10^9 cycles of A42 are about 176 MPa. Specially, A48 doesn't produce one conventional S-N curve as before: Below ~230 MPa, specimen can survive up to 2×10^9 cycles. Above 230 MPa, specimens fracture very quickly, in a few seconds (just 10^5 cycles).

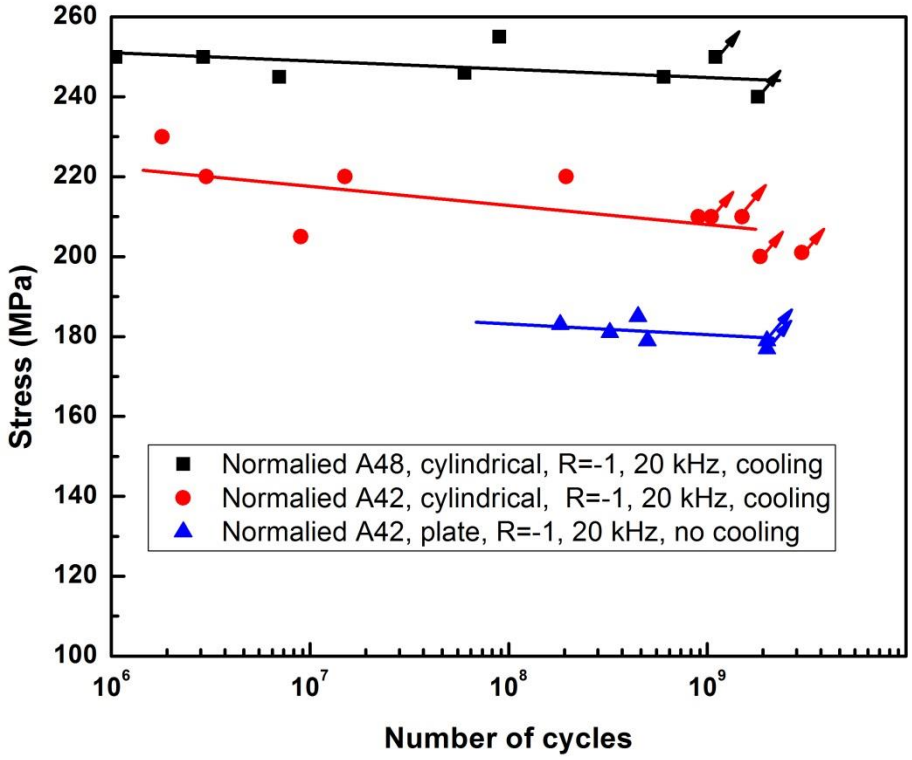

Figure 5.6 Traditional S-N curves of A42 and A48 steels under the condition of with cooling (Huang, 2010), and no cooling in our work.

5.2.2 Thermal response of A42 and A48

According to the sequence of self-heating tests in Figure 5.5, successive interrupted steps of the fatigue tests are conducted with increasing the stress amplitude and the temperature distribution is registered at each step. The evolutions of the maximum temperature for some of the loading steps with different stress amplitudes are shown in Figure 5.7. For A42 in Figure 5.7a, the temperature curves are similar with α-iron and other carbon steels reported in chapter 3.

For A48 in Figure 5.7b, from 159 MPa to 185 MPa, prior to attain the stabilized temperature, the temperature evolution experiences twice rapid increases before 1×10^7 cycles. After the secondary temperature-rise, the specimen temperature could reach 110~180 °C. The 48 steel behavior is similar to that of C12 when decreasing the stress amplitudes in the self-heating tests (Figure 3.27).

According to the rule whether the specimen temperature would reach the stabilization state after 1×10^7 cycles, or the sudden temperature increase up to hundreds of degrees, the temperature evolution can be classified into different stages:

For A42, Stage I: $\sigma_a < 176.5$ MPa; Stage II: $\sigma_a \geq 176.5$ MPa.

For A48, Stage I: $\sigma_a < 194$ MPa; Stage II: $\sigma_a \geq 194$ MPa. But for this steel, Stage I is also composed of

- Stage I_A: $\sigma_a < 151$ MPa
- Stage I_B: 151 MPa $< \sigma_a \leq 185$ MPa

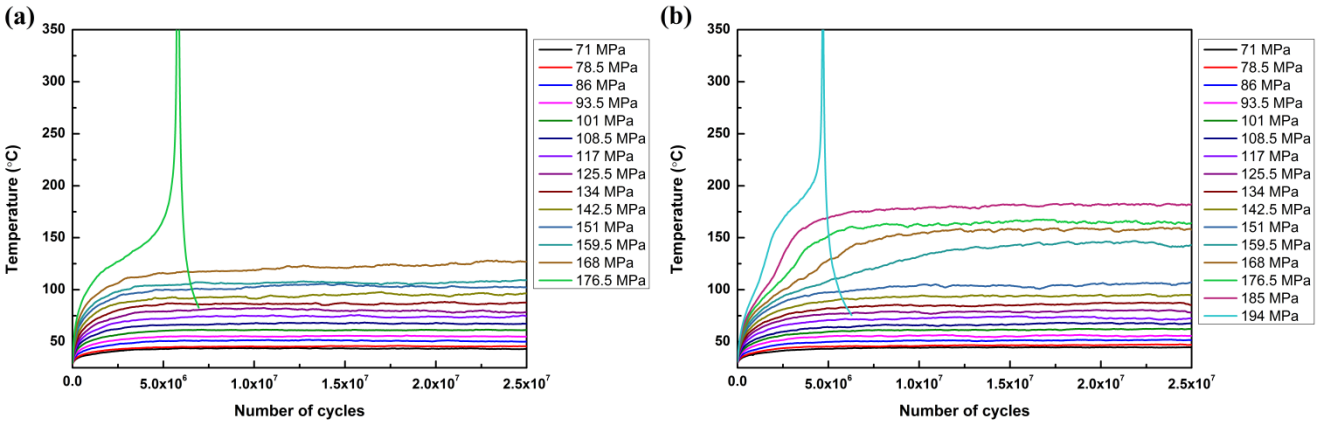

Figure 5.7 Temperature evolutions in self-heating tests for (a) A42, (b) A48.

Combining with results of S-N curve under no cooling, the fatigue behaviour of A42 can verify the conclusions obtained in chapter 3 that the sudden temperature increase is related to the transition of deformation mechanism from thermal regime and athermal regime.

For the A48 steel, in view of these results, the DSA effect is suspected to be responsible for the secondary temperature increase. Previously, a series of tempered A48 steels at 400 °C and 600 °C have been performed the internal friction tests (Figure 4.11), which have shown that only thermal treatment at 600 °C can reduce the SP and SKKP. So, self-heating tests would be conducted on the tempered A48 steels at 600 °C for 1.5h, 6.5h, 26.5h.

5.2.3 Thermal response of thermal-treated A48s

According to above-mentioned method of self-heating tests, we compare their thermal responses after various tempering durations in Figure 5.8a to Figure 5.8c. The behavior of the A48+26.5h steel is similar to that of A42 steel with two stages. For A48+26.5h, Stage I: $\sigma_a < 185$ MPa; Stage II: $\sigma_a \geq 185$ MPa.

It can be found that after tempering during 1.5 h and 6.5 h, the temperature evolutions present the similar profile as A48 (Figure 5.7b). For the Stage II corresponding to the sudden temperature increase, some differences can be noted depending on the stress amplitude.

For A48+1.5h, Stage I: $\sigma_a < 194$ MPa; Stage II: $\sigma_a \geq 194$ MPa.

For A48+6.5h, Stage I: $\sigma_a < 194$ MPa; Stage II: $\sigma_a \geq 194$ MPa.

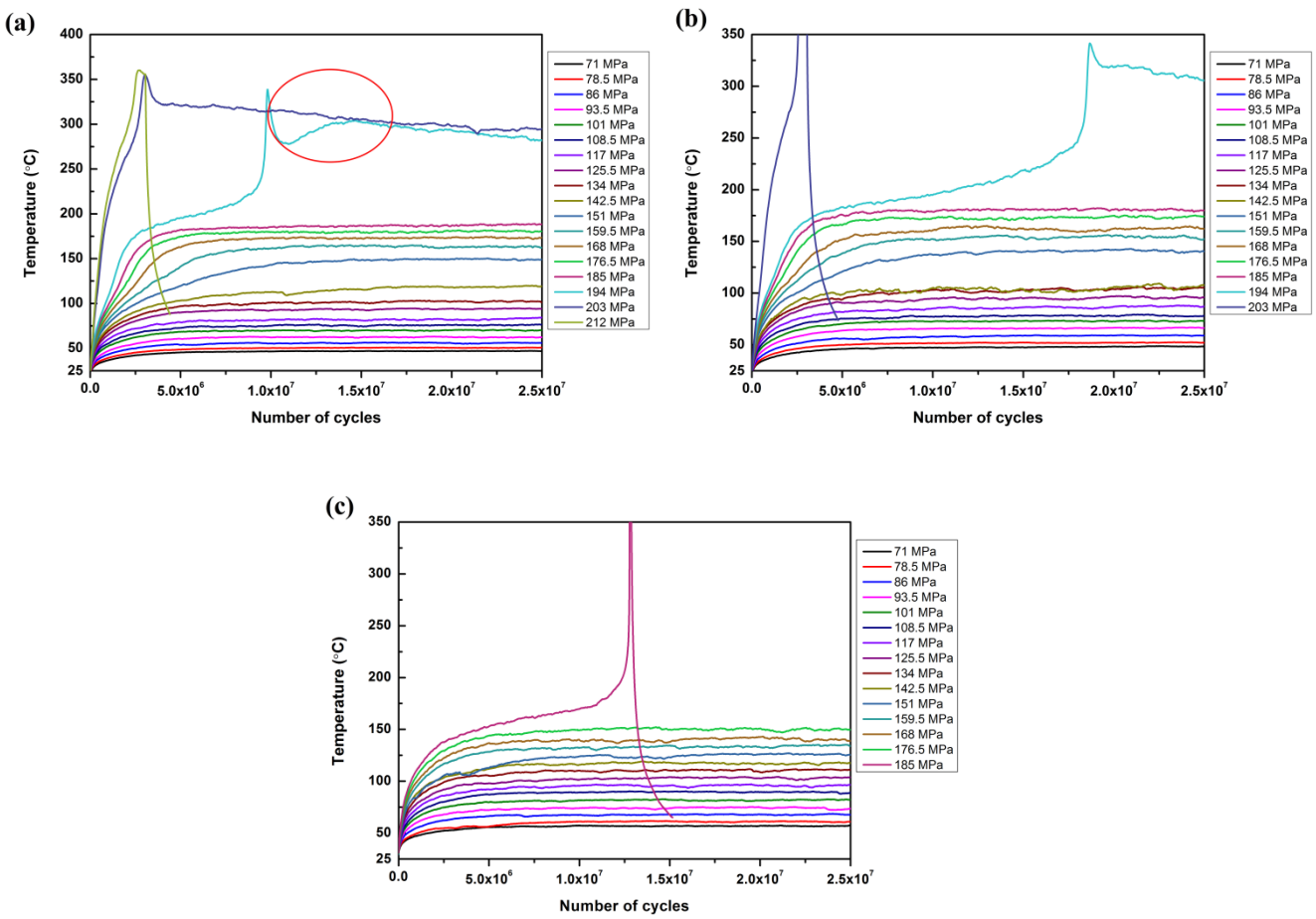

Figure 5.8 Temperature evolutions versus number of cycles under different stress amplitude for (a) A48+1.5h, (b) A48+6.5h, (c) A48+26.5h.

In Figure 5.8, at Stage II of A48+1.5h and A48+6.5h, the stabilized temperature can not be reached anymore. For A48+1.5h at 194 MPa, after twice temperature increases before 1×10^7 cycles, a sharp elevation to 336 ℃ of the specimen temperature happens at 1×10^7 cycles, followed by rapid specimen temperature drop, then a slight increase, finally the specimen temperature keeps decreasing slowly. This kind of temperature "decrease-increase-decrease" is highlighted by red circle in Figure 5.8a. At the next higher stress (203 MPa), the temperature directly decreases slowly along subsequent cycles after reaching 350 °C. In Figure 5.8b, for A48+6.5h at 194 MPa, the temperature also has the same "decrease-increase-decrease" profile, but in a much lesser extent than A48+1.5h. As to A48+2.6.5h, it doesn't appear.

5.2.4 Effect of heat-treatment on microstructure and properties

Microstructure evolution

Effect of tempering treatment on microstructure is strongly linked with the transformation of steels. Tempering at 400~650 ℃ can realize the recovery and recrystallization process of α-phase, which are both energy release process to eliminate high-energy caused by defects, dislocations (Zhao and Zhang, 1991) and so on. Up to 500 ℃, all residual stress in steels are basically eliminated.

The microstructures of tempered A48 steels could be observed by optical microscope after electrical polishing, shown in Figure 5.9. Cementite in normalized A48 is compact lamellar structure. After 1.5 h treatment, the pearlite colonies are decomposed into small granular shape (indicated by red arrows in Figure 5.9b), due to the thermal stress in cementite during thermal treatment. The percentage of cementite decomposition is affected by thermal treatment duration (Shin et al., 2001). When treated for 26.5 h, cementite in all grains have completely decomposed (globularization) and fine cementite Fe_3C precipitates are distributed throughout ferrite matrix and gathered in ferrite grain boundary. Tiny precipitations in ferrite grains become more obvious in Figure 5.9d.

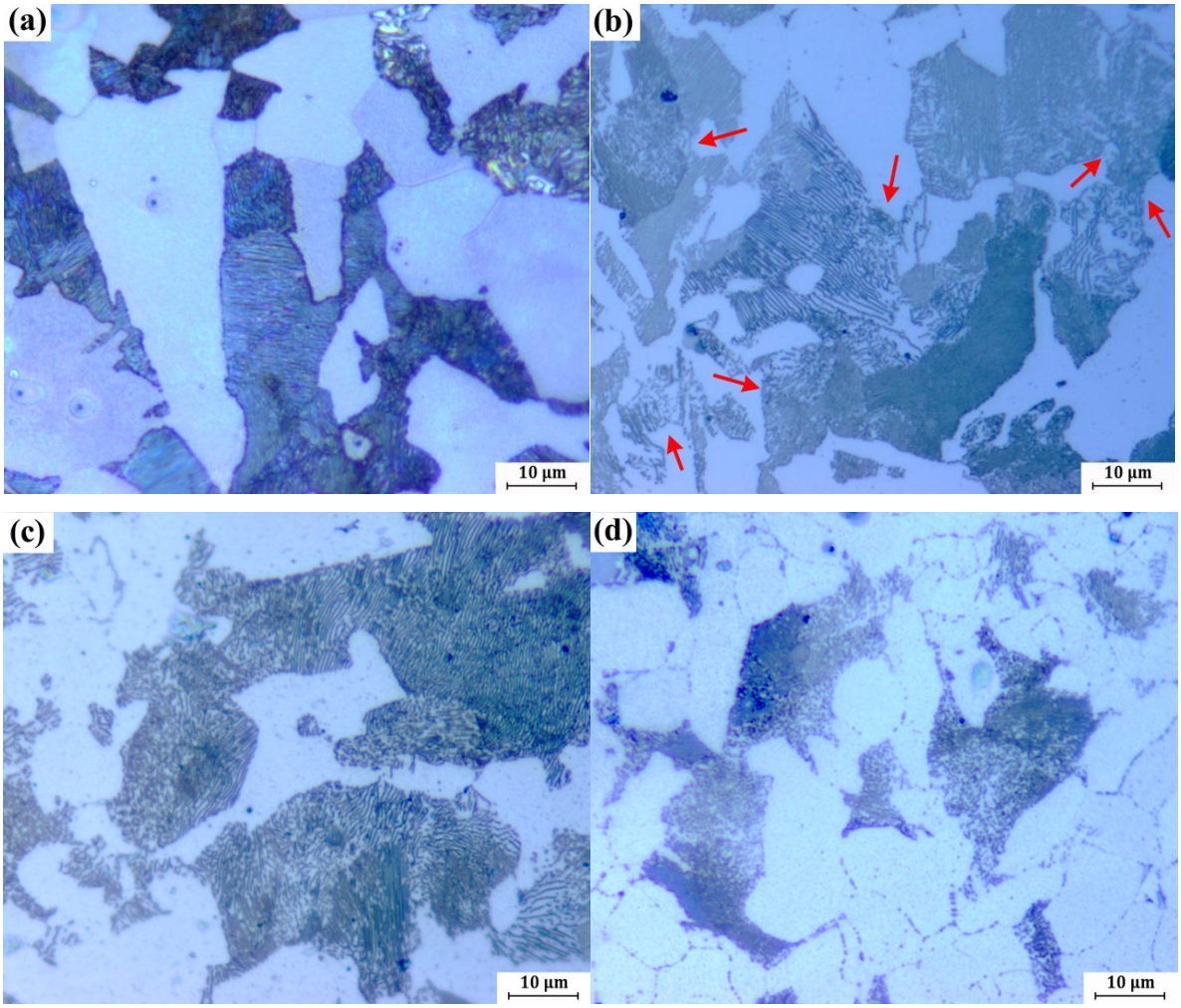

Figure 5.9 Cementite morphology observed by optical microscope after tempering at 600 °C for different durations (a) A48, (b) A48+1.5h steel, (c) A48+6.5h steel, (d) A48+26.5h steel.

Tensile tests

Effect of heat treatment on the mechanical curves and hardness are illustrated in Figure 5.10 and Table 5.2. Tempering doesn't change remarkably the material properties. Indeed, extension of tempering duration makes UTS and yield plateau stress decrease rather weakly. Tempering durations do not affect greatly on hardness, remaining approximately constant. From these analyses, tempering at 600 ℃ could increase A48 steel ductility and maintain its strength at room temperature to the maximum extent.

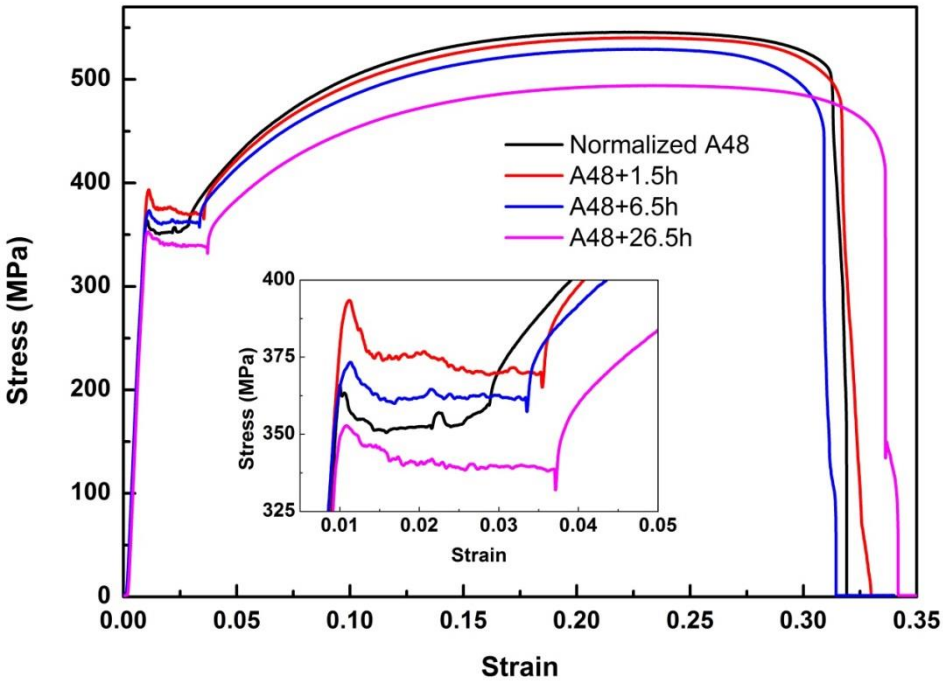

Figure 5.10 Uniaxial tension tests at room temperature with the tensile rate of 10 mm/min (strain rate about 10^{-4} s^{-1}).

Table 5.2 Hardness of A48 before and after heat treatement.

Tempering duration	Hardness (HRA)
0 h	43.4
1.5 h	45
6.5 h	44.6
26.5 h	43

Internal friction tests

Figure 5.11 shows the internal friction results on the A48 steel after various tempering durations at 400 ℃ and 600 ℃. The height of SP and SKKP after tempering at 400 ℃ does not change at all, regardless of tempering durations. Whereas, tempering at 600 ℃ makes both peaks drop apparently with increasing tempering time. For the tempering duration of 26.5 h, SP and SKKP nearly disappear.

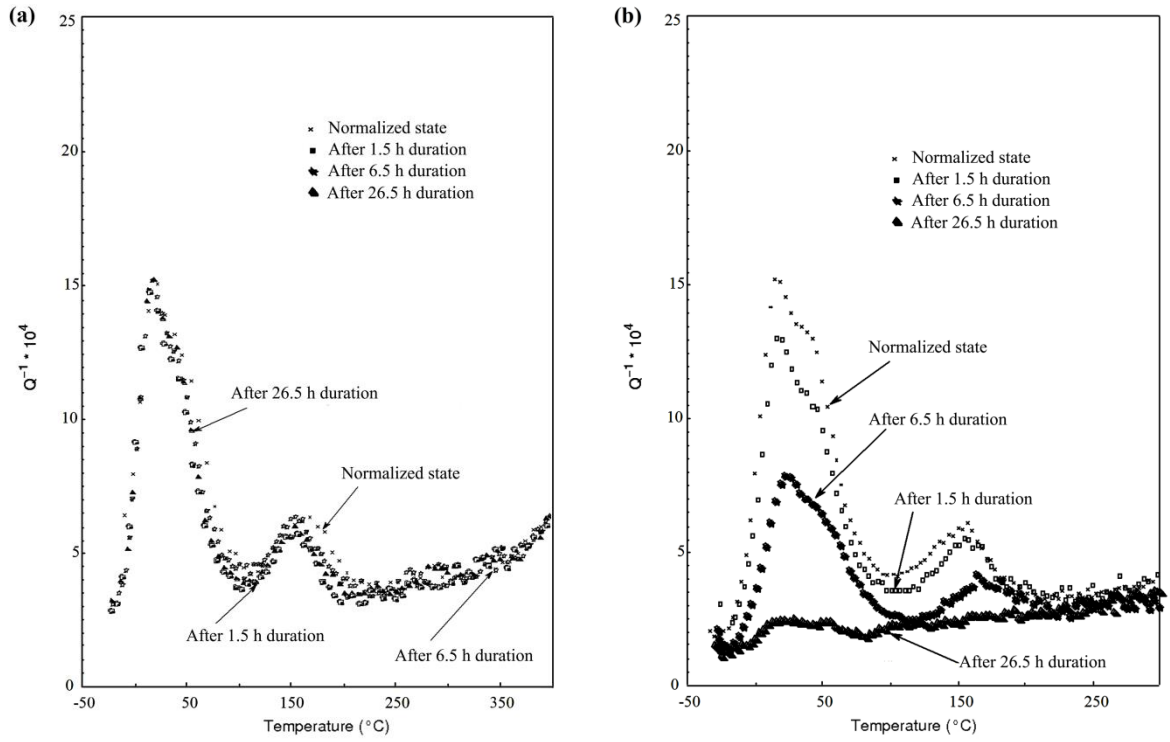

Figure 5.11: Evolution curve of internal Friction after different durations for A48 steel at (a) 400 ℃ and (b) 600 ℃. (Moreno, 1998)

In order to have a better understanding of these figures, we have to know the transformation caused by thermal treatment. Nucleation temperature of carbide always happens between 250 ℃ and 400 ℃. Above 400 ℃, metastable ε-carbides precipitates and *x*-carbides precipitates formed at lower temperature tend to transform into more stable θ-carbides Fe_3C. (Sharma, 2003) Another aspect, optimal nucleation temperature of aluminum nitrides locates at 700 ℃ (Sennour and Esnouf, 2003; Liu et al., 2009; Luo et al., 2016), and at a lower or higher temperature the nucleation rate would correspondingly decrease. Occurrence of nitrides precipitation usually takes place near or above 600 ℃ (Liu et al., 2009; Mucsi, 2014). That's to say, 400 ℃ is always used to precipitate carbides, 600 ℃ for nitrides.

From Figure 5.11, it is verified again that interstitial solute atoms in A48 are free nitrogen atoms, not carbon atoms. It is also declared that tempering at 600 ℃ would be an effective and easy way to decrease interstitial nitrogen atoms.

Although it may not exist a proportional relation between peak height and interstitial atoms owing to the interaction of nitrogen and manganese atoms, we can roughly

estimate that three tempered A48 in our work contain probably 81% (A48+1.5h), 48% (A48+6.5h), 7% (A48+26.5h) nitrogen atoms in lattice relative to A48, respectively.

5.3 Discussion

For stage I, the behaviors of A42 steel are different from those of A48, A48+1.5h and A48+6.5h, whereas the A48+26.5h response is identical to those of A42.

For the A48 steel, the temperature evolution (Figure 5.7b) shows an inflexion point about ~110 ℃. The inflexion point appears as an additional temperature increase. Figure 5.12a compares the temperature increase for A48 and A48+26.5h under the same stress amplitude 168 MPa, extracted from Figure 5.7b and Figure 5.8c. We consider that the additional temperature increase comes from the diffusion of N atoms at short distances (SKKP) towards the mobile dislocations during cyclic loading. As for DSA, the solute atoms diffusion leads to the pinning and unpinning of dislocations which induces the temperature increase.

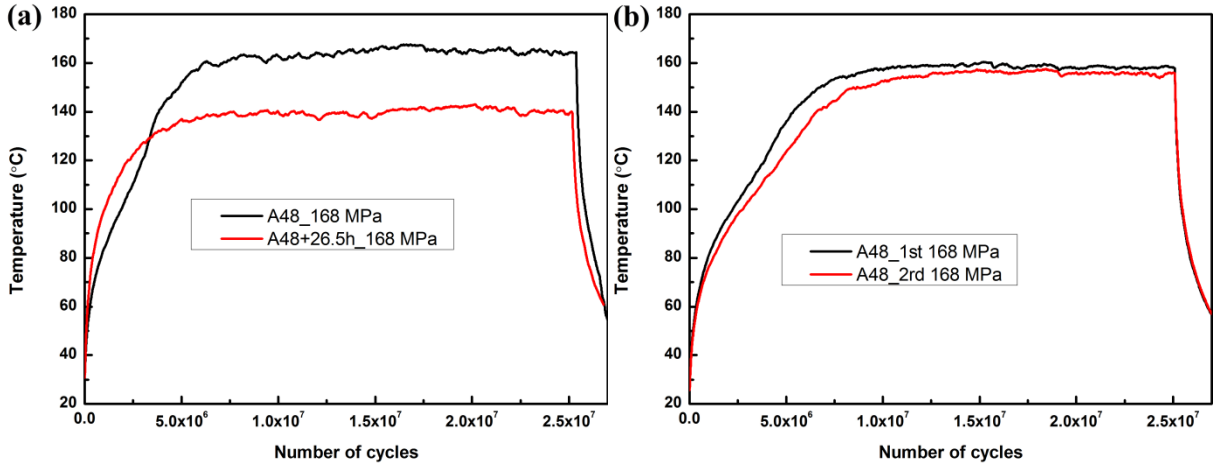

Figure 5.12 Temperature evolutions in self-heating tests (a) on A48 and A48+26.5h steel at 168 MPa, (b) two tests at 168 MPa on the same A48 specimen.

In Figure 5.12b, a new A48 sample is tested to stress amplitude of 168 MPa until 2.5×10^7 cycles, then cooled to ambient temperature and tested again under 168 MPa until 2.5×10^7 cycles. The behaviour of this sample is basically identical to the first sample (shown in Figure 5.12a), owning two temperature-increase before stabilization. For steels (A48) with free solute atoms in the lattice, DSA phenomenon plays an important role in the temperature increases.

The A42 and retreated A48+26.5h steels which show no SKKP or contain very few solute atoms in the lattice, don't show this behavior, which is due to the unchanged N and C atoms distribution.

As explained in the chapter 3, the temperature increase in stage I is correlated with the gliding of edge dislocations. For the steels with an inflexion point in the temperature increase, this secondary increase is associated with the interaction of edge dislocations and free interstitial atoms.

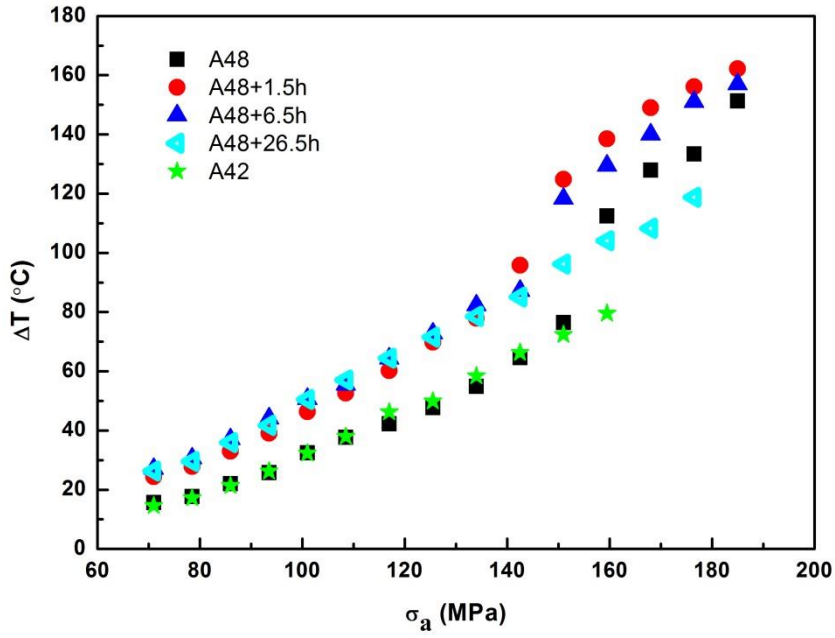

Figure 5.13 Maximum temperature increments at stabilization stage versus the applied stress amplitudes.

Figure 5.13 summarizes the maximum stabilization temperature evolution (Period II, explained in Figure 5.10) in Stage I versus the applied stress amplitude of A42, A48 and the three tempered A48. This figure proposes several interesting phenomena:

① all tempered A48 steels dissipate more heat than A42 and A48 at all stress amplitudes, at least 10 °C. A42 and A48 present almost the same temperature elevation at initial phase.

② A48, A48+1.5h and A48+6.5h have a big temperature jump (at least 30 °C) at 140~160 MPa, but A48+26.5h and A42 do not have this phenomenon.

③ A48+1.5h and A48+6.5h have occurrence of temperature jump at lower stress amplitudes than A48.

As to why normalized A42 and A48 have the same temperature in stage I is because they have the similar carbon content. Naturally, their similar ferrite phase fraction results in same temperature elevation, since dislocations movement mainly happens in soft ferrite grains. Tempering at 600 ℃ is enough high to eliminate lattice distortion, to obtain the well-ordered atoms arrangement in ferrite grains, which reduces the obstacles to dislocations movement and increase the mean free path of dislocations. This is why tempering duration enhances specimen temperature in stage I.

The phenomena ② and ③ in Figure 5.13 should be related to the free interstitial atoms in solid solution. According to Figure 5.4 and Figure 5.11, A42 and A48+26.5h have no peaks in internal friction spectra, which proves the low content of interstitial atoms in these two steels. So, dynamic strain aging cannot be activated under this condition.

With nitrides precipitation taking place during tempering, less interstitial nitrogen atoms are possible to interact with dislocations. Experimental phenomenon ③ indicates that decrease of interstitial atoms content could urge the occurrence of temperature jump in thermal responses at a lower stress amplitude and a higher temperature. It seems not consistent with the conclusion from Kim et al. (2003) that the addition of nitrogen retarded DSA to higher temperature in 316L steels, which is austeniste FCC steel. The phenomenon in our work should be attributed to nitrogen precipitation due to tempering at 600 °C and the reduce of residual stress after tempering. As to the effect of dislocation structure, it requires the further TEM analysis.

At Stage II of A48+1.5h (in Figure 5.8a), the third sudden temperature increase (194 MPa, at 1×10^7 cycles) can be regarded as the signal of screw dislocations having been massively multiplied, which has been approved in chapter 3. The subsequent temperature “decrease-increase-decrease” profile may mean that the specimen experiences “hardening-softening-hardening” process.

As well-accepted about micro-mechanism of dynamic strain aging, the microscopic movement of dislocations is a discontinuous process: mobile dislocations will be arrested temporarily by obstacles, and wait some time for the thermal-activated effect to conquer the obstacles; and then move to next obstacles. (Beukel, 1975) So this

process can be described by the equation: $t=t_a+t_w$. t_a is the time for solute atoms to pin the dislocations, and t_w is the time for dislocations to wait.

Therefore, in red circle of "decrease-increase-decrease" (marked in Figure 5.8a), the first "decrease" could be caused by the hardening effect that due to the multiplicited screw and edge dislocations which are pinned rapidly by interstitial atoms and the dislocations are hindered. Thus, the temperature decreases. The subsequent "increase" is possible to be related with the softening from reorganization of dislocation structures. The softening process is also observed in low cycles fatigue tests (Huang et al., 2014). It is reported by TEM photos (Cuddy and Nabil Bassim, 1989; Valiev et al., 1996; Shih et al., 2009) that dislocations structure would change from randomly scattered dislocations forest structure to low energy dislocations cell structure in BCC structure. The softening phenomenon results from this rearrangement of dislocations structure. Finally, the slow and continuous "decrease" is caused by the hardening of dynamic strain aging (Huang et al., 2014). After experiencing a series of hardening, dislocations movement requires a higher stress amplitude to overcome the obstacles, but the applied stress amplitude cannot afford dislocations to overcome new obstacles.

The irreversible "hardening-softening-hardening" microstructural evolution which is inferred from themperature curves at 194 MPa is inevitable to produce "hardening-hardening" process at 203 MPa. The higher stress amplitude meets the requirement for dislocations to conquer the obstacles. However, rearrangement of dislocations structure to cells is impossible to reoccur in the same tested specimen.

Comparing A48+1.5h and A48+6.5h steels, the A48+6.5h steel has a smaller and tardy peak at 194 MPa and "decrease-increase-decrease" process becomes weaker. It is likely to attribute to interstitial nitrogen atoms content. Dynamic strain aging is the interaction of dislocations and solute atoms, so it's reasonable to state that dynamic strain aging will weaken with decreasing nitrogen content. For the A48+26.5h which contains only ~7% nitrogen interstitial atoms relative to A48, it's possible that the impurity interstitial atoms are insufficient to activate Fatigue dynamic strain aging. Thus, A48+26.5h behaves more similarly with A42.

5.4 Conclusions

This chapter compares the thermal behavior of C-Mn steels (A42, A48, A48+1.5h, A48+6.5h, and A48+26.5h) in self-heating tests. A42 and A48 are dual-phase ferrite-pearlite steels with different content of interstitial nitrogen atoms. A48 has the potential dynamic strain aging between 110 ~ 220 °C, due to higher content of interstitial nitrogen atoms. A series of tempering durations (1.5 h, 6.5 h, 26.5 h) are applied to gradually decrease the interstitial nitrogen atoms content in the lattice, owing to nitrogen atoms precipitation as nitrides during high temperature tempering (600 °C).

(1) In stage I, before stabilized temperature, A42 and A48+26.5h have one temperature increase in self-heating tests, while A48, A48+1.5h, A48+6.5h have two successive temperature increases. And the secondary temperature increment appears above 110 °C, corresponding to the activation temperature of dynamic strain aging. The secondary temperature increase is possible to be caused by interaction of interstitial atoms and edge dislocations.

(2) In stage II, after specimen temperature suddenly increases to hundreds of degrees, A48, A48+1.5h and A48+6.5h show the temperature “decrease-increase-decrease” process, corresponding to be “hardening-softening-hardening” process caused by interaction of interstitial nitrogen atoms and screw dislocations.

(3) Reduction of interstitial nitrogen atoms weakens the DSA. The low amount of interstitial atoms caused by tempering lead to the complete disappearance of secondary temperature increase and DSA effect.

Conclusions and Perspectives

General conclusions

In this work, dual-phase ferrite-pearlite steels are investigated during fatigue tests under 20 kHz high-frequency tension-compression loading in the VHCF domain. Thermal response in self-heating tests are recorded to improve the fatigue damage knowledge. Two parameters are considered, i.e. pearlite phase fraction, interstitial nitrogen atoms in solid lattice. An α-iron, C12 and C65 steels are chosen to investigate the effect of phase constituents, while A42 and A48 steels are applied to study the influence of interstitial carbon and nitrogen atoms. Classically, during a fatigue test, the specimen surface temperature at the beginning increases rapidly and then stabilizes. After the crack initiation, before the fracture occurs, the temperature increases very quickly. For the BCC steels, under high stress amplitudes, a sudden increase of the temperature occurs without the crack initiation and fracture. The main conclusions can be summarized as following:

1. The enough high stress amplitudes accompanied by specimens temperature suddenly up to hundreds of degrees, corresponds to the limit for these BCC steels between thermal regime ($< T_0$) and athermal regime ($> T_0$) at high frequency cyclic loading.

- In athermal regime, a series of optical microscopic observations give the evidences that the temperature increase is caused by dislocations multiplication with the occurrence of many PSBs, and numerous micro-voids in matrix.

- In thermal regime, the tendency of ΔT-σ_a curves under high frequency fatigue loading are non-linear for all studied BCC steels. The dissipated energy per cycle always displays the power relation with the stress amplitude. Microscopic observations indicate that few PSBs can be found in rare few grains at some stress amplitude. However, at lower stress amplitude, it will not produce any PSBs. In this case, surface roughness can be observed on the grain surfaces.

2. The cumulative hardening effect in self-heating tests would cause the increase of the flow stress and the decrease of temperature variation at each step loading.

3. The number of cycles of first recognizable PSBs appearance consume a lower fraction of the fatigue life at higher loading amplitude. PSBs threshold lie below the conventional fatigue limit.

4. Results of self-heating tests indicate that more pearlite fraction in steels leads to higher fatigue strength. The corresponding temperature elevation and dissipated energy decline with increasing pearlite fraction.

5. The secondary temperature increment appearing at ~110 °C, corresponds to the activation temperature of dynamic strain aging in steels, even at the strain rate around 100 s^{-1} due to the high frequency loading. The secondary temperature increase is possible to be caused by interaction of interstitial atoms with edge dislocations in thermal regime ($< T_0$).

6. After the sudden specimen temperature increases to hundreds of degrees, A48, A48+1.5h and A48+6.5h show a temperature "decrease-increase-decrease" process, which is caused by interaction of interstitial atoms and screw dislocations in thermal regime ($> T_0$).

7. Reduction in free interstitial nitrogen atoms content caused by thermal treatment would weaken the dynamic strain aging. Very low content of interstitial atoms could lead to the complete disappearance of the secondary temperature increase and dynamic strain aging effect.

Perspectives

Some investigations can be conducted to confirm and extend our results in this thesis, as following:

- Self-heating tests under very low stress amplitude (< 50 MPa) to verify if it exists a maximum stress amplitude under which there is no specimen temperature variation.

- Transmission electron microscope (TEM) studies to verify the relation of the observed surface roughness on α-iron and the published "loop patches" in the literature.

- Effect of frequency on the cyclic stress-strain curve of BCC metals. To portray the

CSSC under 20 kHz fatigue loading and the corresponding dislocation structures at different stages by means of TEM. Correspondingly, estimation of the irreversibility factor *p*.

- Fatigue tests at low stress amplitude (< 103 MPa) far over 10^{10}-10^{11} cycles to investigate the evolution of roughness on α-iron surface: effect of number of cycles and stress amplitudes on roughness (Rz, Ra, et al.) by a professional roughness measuring instrument.

- Investigation of PSB evolution (height, width, initial site of PSBs) on number of cycles and stress amplitudes for α-iron carried out by 3D optical microscope, atomic force microscopic (AFM) or in situ micro computed tomography (micro-CT).

- Recording of the temperature changes after sudden temperature increase by IR camera with higher measurement range. And the localized temperature in ferrite grains by high definition IR thermal imager.

- Investigation of the effect of other parameters on thermal response in self-heating tests, for example, grain size.

We have done partial complementary investigations about effect of average grain size on thermal response under high frequency cyclic loading. Figure 5.1 shows the temperature elevation of two irons with different grain sizes. The α-iron with mean grain size 35 μm is the same one as in chapter 3. And the other with mean grain size 170 μm is obtained by cold molding and recrystallization at 1050 °C on the same α-iron.

Under the same stress amplitude, α-iron with bigger grains always present a higher temperature elevation than that with smaller grains. When we talk about the effect of grain size on fatigue properties, the law “smaller is stronger” is very useful. This agrees with the conclusion in chapter 3. Less temperature elevation, higher fatigue strength.

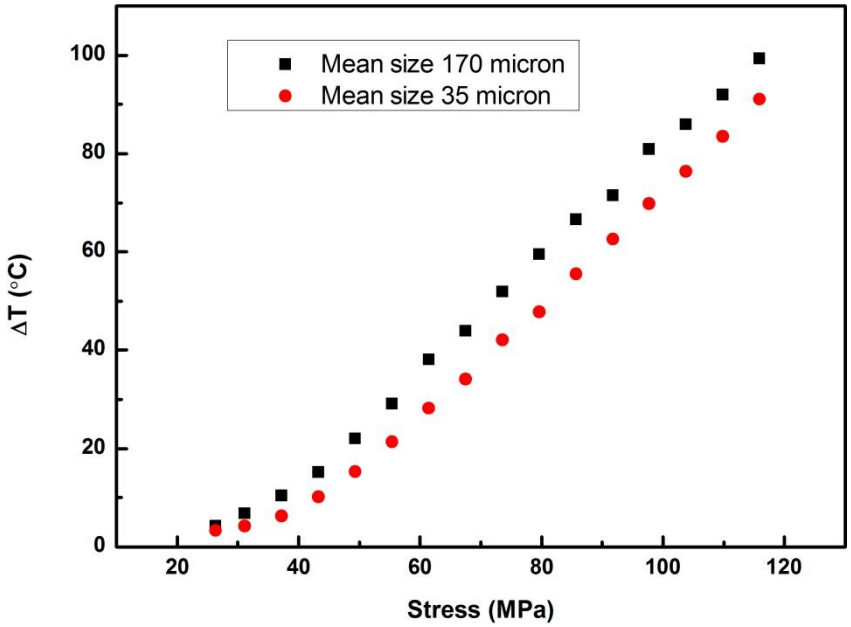

Figure 6.1 Temperature elevation of α-iron with different grain sizes.

References

Abdel-Salam M. Eleiche (1981). Strain-rate history and temperature effects on the torsional-shear behavior of a mild steel. Exp. Mech. *21*, 285–294.

Amiri, M., and Khonsari, M.M. (2010). Life prediction of metals undergoing fatigue load based on temperature evolution. Mater. Sci. Eng. A *527*, 1555–1559.

Arakere, N.K. (2016). Gigacycle rolling contact fatigue of bearing steels: A review. Int. J. Fatigue *93*, 238–249.

Bain, E.C. (1939). Functions of the Alloying Elements in Steel (American Society for Metals).

Baird, J.D. (1971). The effects of strain-ageing due to interstitial solutes on the mechanical properties of metals. Metall. Rev. *16*, 1–18.

Bao, W.P. (2010). Experimental research on the dynamic constitutive relation of pure iron at elevated temperatures and high strain rates. J. Mech. Eng. *46*, 74.

Bardes, B. (1978). Metals Handbook: Properties and Selection: Irons and Steels (American Society for Metals).

Bathias, C. (1999). There is no infinite fatigue life in metallic materials. Fatigue Fract. Eng. Mater. Struct. *22*, 559–565.

Bathias, C., and Paris, P.C. (2005). Gigacycle fatigue in mechanical practice (New York: CRC press).

Bathias, C., and Pineau, A. (2013). Fatigue of Materials and Structures (Wiley Online Library).

Beukel, A. van den (1975). Theory of the effect of dynamic strain aging on mechanical properties. Phys. Status Solidi A *30*, 197–206.

Bhat, S.P., and Laird, C. (1978). The cyclic stress-strain curves in monocrystalline and polycrystalline metals. Scr. Metall. *12*, 687–692.

Botny, R., and Kaleta, J. (1986). A method for determining the heat energy of the fatigue process in metals under uniaxial stress: Part 1. Determination of the amount of heat liberated from a fatigue-tested specimen. Int. J. Fatigue *8*, 29–33.

Boulanger, T., Chrysochoos, A., Mabru, C., and Galtier, A. (2004). Calorimetric analysis of dissipative and thermoelastic effects associated with the fatigue behavior of steels. Int. J. Fatigue *26*, 221–229.

Brown, M.W., and Miller, K.J. (1973). A Theory for Fatigue Failure under Multiaxial Stress-Strain Conditions. Proc. Inst. Mech. Eng. *187*, 745–755.

Brugger, C., Palin-Luc, T., Osmond, P., and Blanc, M. (2017). A new ultrasonic fatigue testing device for biaxial bending in the gigacycle regime. Int. J. Fatigue *100*,

619–626.

Callister, W.D. (2007). Materials science and engineering: an introduction (New York: John Wiley & Sons).

Callister, W.D. (2015). Fundamentals of Materials Science and Engineering: An Integrated Approach, 5th Edition.

Campbell, J.D., and Ferguson, W.G. (1970). The temperature and strain-rate dependence of the shear strength of mild steel. Philos. Mag. J. Theor. Exp. Appl. Phys. *21*, 63–82.

Cazaud, R., Pomey, G., Rabbe, P., and Janssen, C. (1968). La Fatigue des Métaux (Paris: Dunod).

Charles, J.A., Appl, F.J., and Francis, J.E. (1975). Using the scanning infrared camera in experimental fatigue studies. Exp. Mech. *15*, 133–138.

Chmelík, F., Klose, F.B., Dierke, H., Šachl, J., Neuhäuser, H., and Lukáč, P. (2007). Investigating the Portevin-Le Châtelier effect in strain rate and stress rate controlled tests by the acoustic emission and laser extensometry techniques. Mater. Sci. Eng. A *462*, 53–60.

Chrysochoos, A., and Louche, H. (2000). An infrared image processing to analyse the calorific effects accompanying strain localisation. Int. J. Eng. Sci. *38*, 1759–1788.

Chrysochoos, A., Maisonneuve, O., Martin, G., Caumon, H., and Chezeaux, J.. (1989). Plastic and dissipated work and stored energy. Nucl. Eng. Des. *114*, 323–333.

Cuddy, J., and Nabil Bassim, M. (1989). Study of dislocation cell structures from uniaxial deformation of AISI 4340 steel. Mater. Sci. Eng. A *113*, 421–429.

Cura, F., Curti, G., and Sesana, R. (2005). A new iteration method for the thermographic determination of fatigue limit in steels. Int. J. Fatigue *27*, 453–459.

Doudard, C., Poncelet, M., Calloch, S., Boue, C., Hild, F., and Galtier, A. (2007). Determination of an HCF criterion by thermal measurements under biaxial cyclic loading. Int. J. Fatigue *29*, 748–757.

Ewing, J.A., and Humfrey, J.C.W. (1903). VI. The fracture of metals under repeated alternations of stress. Phil Trans R Soc Lond A *200*, 241–250.

Favier, V., Blanche, A., Wang, C., Phung, N.L., Ranc, N., Wagner, D., Bathias, C., Chrysochoos, A., and Mughrabi, H. (2016). Very high cycle fatigue for single phase ductile materials: Comparison between α-iron, copper and α-brass polycrystals. Int. J. Fatigue *93*, 326–338.

Forsyth, P.J.E. (1951). Some metallographic observations on the fatigue of metals. J. Inst. Met. *80*, 181.

Forsyth, P.J.E. (1953). Exudation of material form slips bands at the surface of fatigued crystals of an aluminum copper alloy. Nature *171*, 172–173.

Forsyth, P.J.E. (1963). Fatigue damage and crack growth in aluminium alloys. Acta Metall. *11*, 703–715.

François, D., Pineau, A., and Zaoui, A. (2012). Mechanical Behaviour of Materials: Volume 1: Micro- and Macroscopic Constitutive Behaviour (Springer Netherlands).

Gladman, T., and Barker, R. (1971). Internal friction characteristics of interstitial carbon and nitrogen in alpha-iron. J. Phys. Colloq. *C2*, C2-57-C2-58.

Guo, Q., and Guo, X. (2016). Research on high-cycle fatigue behavior of FV520B stainless steel based on intrinsic dissipation. Mater. Des. *90*, 248–255.

Guy, A.G. (1976). Essentials of Materials Science (New York: McGraw-Hill Book Company).

Hempel, H. (1957). Metallographic observations on the fatigue of steels. In Proceedings of the International Conference on Fatigue of Metals, (London: Institution of Mechanical Engrs.), p.

Hong, Y.S., and Sun, C.Q. (2017). The nature and the mechanism of crack initiation and early growth for very-high-cycle fatigue of metallic materials – An overview. Theor. Appl. Fract. Mech. *92*, 331–350.

Hong, Y.S., Lei, Z.Q., Sun, C.Q., and Zhao, A.Q. (2014). Propensities of crack interior initiation and early growth for very-high-cycle fatigue of high strength steels. Int. J. Fatigue *58*, 144–151.

Huang, Z.Y. (2010). Endommagement des aciers au C-Mn en fatigue oligocyclique et gigacyclique. PhD dissertation. Université Paris Nanterre.

Huang, Z.Y., Wagner, D., Wang, Q.Y., and Bathias, C. (2013). Effect of carburizing treatment on the "fish eye" crack growth for a low alloyed chromium steel in very high cycle fatigue. Mater. Sci. Eng. A *559*, 790–797.

Huang, Z.Y., Chaboche, J.L., Wang, Q.Y., Wagner, D., and Bathias, C. (2014). Effect of dynamic strain aging on isotropic hardening in low cycle fatigue for carbon manganese steel. Mater. Sci. Eng. A *589*, 34–40.

Huang, Z.Y., Wagner, D., and Bathias, C. (2015). Some metallurgical aspects of Dynamic Strain Aging effect on the Low Cycle Fatigue behavior of C-Mn steels. Int. J. Fatigue *80*, 113–120.

Huang, Z.Y., Ranc, N., and Wagner, D. (2016). Dislocations gliding study by IR thermography in C-Mn steels with different solute atoms content in the gigacycle fatigue domain. Key Engineering Materials *664*, 177-187.

Hull, D., and Bacon, D.J. (2011). Introduction to Dislocations (UK: Elsevier).

Jiang, Z.Y. (2018). Développement d'une machine de fatigue gigacyclique en torsion pour les matériaux métalliques à haute résistance. PhD dissertation. Université Paris Nanterre.

Johnson, H.D. (2012). Lüders bands in RPV steel. PhD dissertation. Cranfield University.

Kim, D.W., Kim, W.G., and Ryu, W.S. (2003). Role of dynamic strain aging on low cycle fatigue and crack propagation of type 316L(N) stainless steel. Int. J. Fatigue *25*, 1203–1207.

Kinra, V., and Wolfenden, A. (1992). M3D III: Mechanics and Mechanisms of Material Damping.

Klesnil, M., and Lukáš, P. (1965). Dislocation arrangement in surface layer of alpha-iron grains during cyclic loading. J Iron Steel Inst *203*, 1043–1048.

Knysh, P., and Korkolis, Y.P. (2015). Determination of the fraction of plastic work converted into heat in metals. Mech. Mater. *86*, 71–80.

La Rosa, G., and Risitano, A. (2000). Thermographic methodology for rapid determination of the fatigue limit of materials and mechanical components. Int. J. Fatigue *22*, 65–73.

Laird, C., and Duquette, D.J. (1972). Corrosion Fatigue: Chemistry, Mechanics, and Microstructure. pp. 88–117.

Laird, C., Charsley, P., and Mughrabi, H. (1986). Low energy dislocation structures produced by cyclic deformation. Mater. Sci. Eng. *81*, 433–450.

Lee, B.H., and Kim, I.S. (1995). Dynamic strain aging in the high-temperature low-cycle fatigue of SA508 Cl. 3 forging steel. J. Nucl. Mater. *226*, 216–225.

Lei, Z.Q., Hong, Y.S., Xie, J.J., Sun, C.Q., and Zhao, A.Q. (2012). Effects of inclusion size and location on very-high-cycle fatigue behavior for high strength steels. Mater. Sci. Eng. A *558*, 234–241.

Li, P., Zhang, Z.F., Li, X.W., Li, S.X., and Wang, Z.G. (2009). Effect of orientation on the cyclic deformation behavior of silver single crystals: Comparison with the behavior of copper and nickel single crystals. Acta Mater. *57*, 4845–4854.

Liu, Y., FU, J., and WU, H. (2009). Precipitation of aluminum nitride in low carbon aluminum-killed steel. Chin. J. Iron Steel *21*, 20–0.

Lukáš, P., and Klesnil, M. (1973). Cyclic stress-strain response and fatigue life of metals in low amplitude region. Mater. Sci. Eng. *11*, 345–356.

Luo, B., Li, M., Wang, G., Tan, F., Zhao, J., and Sun, C. (2017). Strain rate and hydrostatic pressure effects on strength of iron. Mech. Mater. *114*, 142–146.

Luo, Z., Wang, L., Sun, Q., Li, S., Ma, Y., and Wang, X. (2016). AlN precipitation behavior and its effect on work hardening of low carbon steel in deep drawing process. Trans. Mater. Heat Treat. *37*.

Luong, M.P. (1995). Infrared thermographic scanning of fatigue in metals. Nucl. Eng. Des. *158*, 363–376.

Luong, M.P. (1998). Fatigue limit evaluation of metals using an infrared thermographic technique. Mech. Mater. *28*, 155–163.

Magalas, L.B. (2006). The Snoek-Köster (SK) relaxation and Dislocation-Enhanced Snoek Effect (DESE) in deformed iron. Solid State Phenom. *115*, 67–72.

Mareau, C. (2009). Influence of the free surface and the mean stress on the heat dissipation in steels under cyclic loading. Int. J. Fatigue *31*, 1407–1412.

Marschall, C.W., Landow, M.P., and Wilkowski, G.M. (1990). Effect of Dynamic Strain Aging on Fracture Resistance of Carbon Steels Operating at Light-Water Reactor Temperatures. Fract. Mech. Twenty-First Symp.

McCormigk, P.G. (1972). A model for the Portevin-Le Chatelier effect in substitutional alloys. Acta Metall. *20*, 351–354.

Mikell P. Groover (2007). Fundamentals of modern manufacturing; materials, processes, and systems (USA: John Wiley & Sons. Inc).

Miller, K.J. (1991). Metal fatigue-past, current and future. Proc. Inst. Mech. Eng. Part C Mech. Eng. Sci. *205*, 291–304.

Moreno, J.C. (1998). Vieillissement dynamique dans les joints soudés d'acier au carbonne manganèse : relation entre les paramètres métallurgiques et le comportement mécanique. PhD dissertation. Châtenay-Malabry, Ecole Centrale de Paris.

Mucsi, A. (2014). Effect of hot rolled grain size on the precipitation kinetics of nitrides in low carbon Al-killed steel. J. Mater. Process. Technol. *214*, 1536–1545.

Mughrabi, H. (1979). Microscopic Mechanisms of Metal Fatigue. In Strength of Metals and Alloys, P. Haasen, V. Gerold, and G. Kostorz, eds. (Pergamon), pp. 1615–1638.

Mughrabi, H. (1999). On the life-controlling microstructural fatigue mechanisms in ductile metals and alloys in the gigacycle regime. Fatigue Fract. Eng. Mater. Struct. *22*, 633–641.

Mughrabi, H. (2002). On "multi-stage" fatigue life diagrams and the relevant life-controlling mechanisms in ultrahigh-cycle fatigue. Fatigue Fract. Eng. Mater. Struct. *25*, 755–764.

Mughrabi, H. (2006). Specific features and mechanisms of fatigue in the ultrahigh-cycle regime. Int. J. Fatigue *28*, 1501–1508.

Mughrabi, H. (2009). Cyclic slip irreversibilities and the evolution of fatigue damage. Metall. Mater. Trans. B *40*, 431–453.

Mughrabi, H. (2013a). Microstructural fatigue mechanisms: Cyclic slip irreversibility, crack initiation, non-linear elastic damage analysis. Int. J. Fatigue *57*, 2–8.

Mughrabi, H. (2013b). Cyclic slip irreversibility and fatigue life: A microstructure-based analysis. Acta Mater. *61*, 1197–1203.

Mughrabi, H. (2015). Microstructural mechanisms of cyclic deformation, fatigue crack initiation and early crack growth. Philos. Transact. A Math. Phys. Eng. Sci. *373*.

Mughrabi, H., and Stanzl-Tschegg, S. (2007). Fatigue damage evolution in ductile single-phase face-centred cubic metals in the UHCF-regime. (Fourth International Conference on Very High Cycle Fatigue (VHCF-4)), pp. 75–82.

Mughrabi, H., Ackermann, F., and Herz, K. (1979). Persistent slip bands in fatigued face-centered and body-centered cubic metals. Fatigue Mech ASTM-STP *675*, 67–105.

Mughrabi, H., Herz, K., and Stark, X. (1981). Cyclic deformation and fatigue behaviour of α-iron mono- and polycrystals. Int. J. Fract. *17*, 193–220.

Mühlhaus, E.H., Wiley, J., Ch, N.Y., and Lakes, R. (1995). Continuum models for materials with microstructure (Wiley).

Munier, R., Doudard, C., Calloch, S., and Weber, B. (2014). Determination of high cycle fatigue properties of a wide range of steel sheet grades from self-heating measurements. Int. J. Fatigue *63*, 46–61.

Munier, R., Doudard, C., Calloch, S., and Weber, B. (2017). Identification of the micro-plasticity mechanisms at the origin of self-heating under cyclic loading with low stress amplitude. Int. J. Fatigue *103*, 122–135.

Norton, F.H. (1929). The creep of steel at high temperatures (New York: McGraw-Hill Book Company).

Ouarabi, M. (2018). Influence de la fréquence de chargement sur la résistance à l'amorçage et la croissance de fissure de fatigue dans des aciers utilisés pour des applications mécaniques exigeantes. PhD dissertation. Université Paris Nanterre.

Petarra, D.P., and Beshers, D.N. (1967). Cold-work internal friction peak in iron. Acta Metall. *15*, 791–800.

Pohl, K., Mayr, P., and Macherauch, E. (1980). Persistent slip bands in the interior of a fatigued low carbon steel. Scr. Metall. *14*, 1167–1169.

Polák, J., Mazánová, V., Heczko, M., Petráš, R., Kuběna, I., Casalena, L., and Man, J. (2017). The role of extrusions and intrusions in fatigue crack initiation. Eng. Fract. Mech. *185*, 46–60.

Pyttel, B., Schwerdt, D., and Berger, C. (2011). Very high cycle fatigue – Is there a fatigue limit? Int. J. Fatigue *33*, 49–58.

Ranc, N., and Wagner, D. (2007). Experimental study by pyrometry of Portevin-Le Châtelier plastic instabilities-Type A Type B transition. Mater. Sci. Eng. A *474*, 188–196.

Ranc, N., Favier, V., Munier, B., Vales, F., Thoquenne, G., and Lefebvre, F. (2015). Thermal Response of C45 Steel in High and Very High Cycle Fatigue. Procedia Eng. *133*, 265–271.

Ranc, N., Du, W., Ranc, I., and Wagner, D. (2016). Experimental studies of Portevin-Le Chatelier plastic instabilities in carbon-manganese steels by infrared pyrometry. Mater. Sci. Eng. A *663*, 166–173.

Reifsnider, K.L., and Williams, R.S. (1974). Determination of fatigue-related heat emission in composite materials. Exp. Mech. *14*, 479–485.

Rittel, D., Zhang, L.H., and Osovski, S. (2017). The dependence of the Taylor-Quinney coefficient on the dynamic loading mode. J. Mech. Phys. Solids *107*, 96–114.

Sakai, T., Sato, Y., and Oguma, N. (2002). Characteristic S-N properties of high-carbon-chromium-bearing steel under axial loading in long-life fatigue. Fatigue Fract. Eng. Mater. Struct. *25*, 765–773.

Sarkar, A., Nagesha, A., Sandhya, R., Laha, K., and Okazaki, M. (2018). Manifestations of dynamic strain aging under low and high cycle fatigue in a type 316LN stainless steel. Mater. High Temp. *35*, 523–528.

Sennour, M., and Esnouf, C. (2003). Contribution of advanced microscopy techniques to nano-precipitates characterization: case of AlN precipitation in low-carbon steel. Acta Mater. *51*, 943–957.

Sharma, R.C. (2003). Principles of heat treatment of steels (New Age International).

Shih, C.C., Ho, N.J., and Huang, H.L. (2009). The relationship between cyclic stress-strain curve and dislocation structures in cyclically deformed IF steel. Mater. Sci. Eng. A *517*, 235–238.

Shin, D.H., Kim, Y.S., and Lavernia, E.J. (2001). Formation of fine cementite precipitates by static annealing of equal-channel angular pressed low-carbon steels. Acta Mater. *49*, 2387–2393.

Snoek, J.L. (1941). Effect of small quantities of carbon and nitrogen on the elastic and plastic properties of iron. Physica *8*, 711–733.

Spriestersbach, D., Grad, P., and Kerscher, E. (2014). Influence of different non-metallic inclusion types on the crack initiation in high-strength steels in the VHCF regime. Int. J. Fatigue *64*, 114–120.

Stanzl-Tschegg, S., Mughrabi, H., and Schoenbauer, B. (2007). Life time and cyclic slip of copper in the VHCF regime. Int. J. Fatigue *29*, 2050–2059.

Suresh, S. (1998). Fatigue of Materials (Cambridge University Press).

Thomas, G.D., and Samuel, J.R. (1960). Heat treatment and properties of iron and steel.

Thompson, N., and Wadsworth, N.J. (1958). Metal fatigue. Adv. Phys. *7*, 72–169.

Torabian, N., Favier, V., Ziaei-Rad, S., Dirrenberger, J., Adamski, F., and Ranc, N. (2016). Thermal response of DP600 dual-phase steel under ultrasonic fatigue loading.

Mater. Sci. Eng. A *677*, 97–105.

Torabian, N., Favier, V., Dirrenberger, J., Adamski, F., Ziaei-Rad, S., and Ranc, N. (2017). Correlation of the high and very high cycle fatigue response of ferrite based steels with strain rate-temperature conditions. Acta Mater. *134*, 40–52.

Torabiandehkordi, N. (2017). High and very high cycle fatigue behavior of DP600 dual-phase steel : correlation between temperature, strain rate, and deformation mechanisms. PhD dissertation. Ecole nationale supérieure d'arts et métiers - ENSAM.

Valiev, R.Z., Ivanisenko, Y.V., Rauch, E.F., and Baudelet, B. (1996). Structure and deformaton behaviour of Armco iron subjected to severe plastic deformation. Acta Mater. *44*, 4705–4712.

Wagner, D., Moreno, J.C., Prioul, C., Frund, J.M., and Houssin, B. (2002). Influence of dynamic strain aging on the ductile tearing of C-Mn steels: modelling by a local approach method. J. Nucl. Mater. *300*, 178–191.

Wagner, D., Roubier, N., and Prioul, C. (2006). Measurement of sensitivity to dynamic strain aging in C-Mn steels by internal friction experiments. Mater. Sci. Technol. *22*, 301–307.

Wagner, D., Ranc, N., Bathias, C., and Paris, P.C. (2010). Fatigue crack initiation detection by an infrared thermography method. Fatigue Fract. Eng. Mater. Struct. *33*, 12–21.

Wagner, D., Wang, C., Huang, Z., and Bathias, C. (2016). Surface crack initiation mechanism for body centered cubic materials in the gigacycle fatigue domain. Int. J. Fatigue *93*, 292–300.

Wang, C. (2013). Microplasticité et dissipation en fatigue à très grand nombre de cycles du fer et de l'acier. PhD dissertation. Université Paris Nanterre.

Wang, C., Blanche, A., Wagner, D., Chrysochoos, A., and Bathias, C. (2014). Dissipative and microstructural effects associated with fatigue crack initiation on an Armco iron. Int. J. Fatigue *58*, 152–157.

Wang, C., Petit, J., Huang, Z., and Wagner, D. (2019). Investigation of crack initiation mechanisms responsible for the fish eye formation in the Very High Cycle Fatigue regime. Int. J. Fatigue *119*, 320–329.

Weidner, A., Amberger, D., Pyczak, F., Schönbauer, B., Stanzl-Tschegg, S., and Mughrabi, H. (2010). Fatigue damage in copper polycrystals subjected to ultrahigh-cycle fatigue below the PSB threshold. Int. J. Fatigue *32*, 872–878.

Weller, M. (1983). The Snoek-Köster relaxation in body-centered cubic metals. J. Phys. Colloq. *44*, C9-63-C9-82.

Winter, A.T. (1974). A model for the fatigue of copper at low plastic strain amplitudes. Philos. Mag. J. Theor. Exp. Appl. Phys. *30*, 719–738.

Wöhler, A. (1870). Über die Festigkeitsversuche mit Eisen und Stahl. Z. Für Bauwes.

20, 73–106.

Yang, S. (2002). Heat Transfer (High Education Press).

Zhang, Z.F., and Wang, Z.G. (2008). Grain boundary effects on cyclic deformation and fatigue damage. Prog. Mater. Sci. *53*, 1025–1099.

Zhang, J.M., Li, S.X., Yang, Z.G., Li, G.Y., Hui, W.J., and Weng, Y.Q. (2007). Influence of inclusion size on fatigue behavior of high strength steels in the gigacycle fatigue regime. Int. J. Fatigue *29*, 765–771.

Zhao, J.S., and Zhang, L.M. (1991). A study on the dislocation density in 300M steel. J. Beijing Univ. Aeronaut. Astronaut. *1*, 14–17.

Zuo, J.H., Wang, Z.G., and Han, E.H. (2008). Effect of microstructure on ultra-high cycle fatigue behavior of Ti-6Al-4V. Mater. Sci. Eng. A *473*, 147–152.

Annex

N ° (Fig 3.31)	N °	N_f (cycles)	Stress (MPa)	Fracture	PSB	Emerging Cycle of PSB
1	C0-7	4.48×10^{6}	129	Yes		
2	C0-14	5.50×10^{6}	125	Yes	Yes	PSB video 4.00E6
3	C0-18	6.0×10^{8}	120	Yes	Yes	PSB video 1.76E6
4	C0-15	1.04×10^{7}	120	Yes	Yes	PSB video 4.30E6
5	C0-13	1.30×10^{7}	115	Yes	Yes	PSB video 3.00E6
6	C0-17	1.40×10^{9}	113	Yes	Yes	PSB video 2.70E6
7	C0-9	1.83×10^{7}	110	Yes	Yes	7.74E6
8	C0-12	2.36×10^{7}	107	Yes	Yes	PSB video 1.13E7
9	C0-21	2×10^{9}	106	*No*	Yes	PSB video
10	C0-20	3.26×10^{9}	105	*No*	Yes	PSB video, ~1E7
11	C0-16	4.11×10^{9}	103	*No*	*No*	*Surface roughness, no PSB*
12	C0-11	3.38×10^{9}	99	*No*	*No*	*Surface roughness, no PSB*
13	C0-6	3.61×10^{9}	96	*No*	*No*	*Surface roughness, no PSB*

N ° (Fig 3.41)	N °	N_f (cycles)	Stress (MPa)	Fracture	Polishing state
1	C12-7	3×10^{5}	195	Yes	Mechanical polishing
2	C12-8	4.4×10^{6}	190	Yes	Mechanical polishing
3	unlabelled	5×10^{6}	193	Yes	Not so good electrical polishing
4	C12-10	1.2×10^{7}	197	Yes	Not so good electrical polishing
5	C12-*	4×10^{7}	194	Yes	Mechanical polishing
6	C12-9	2.36×10^{9}	175	*No*	Good electrical polishing
7	C12-cut	2×10^{9}	190	*No*	Good electrical polishing
8	C12-11	4×10^{9}	194	*No*	Good electrical polishing
9	C12-4	3×10^{9}	195	*No*	Good electrical polishing
10	C12-10	3×10^{9}	197	*No*	Not so good electrical polishing
11	C12-13	3×10^{9}	201	*No*	Good electrical polishing
12	C12-14	3×10^{9}	216	*No*	Good electrical polishing